Mechanical Engineering Department N.A. Sidky
Master's Thesis

Axi-Symmetric Turbulent Wall Jet over a Sphere

The incompressible wall jet over the surface of a sphere has been investigated both experimentally and theoretically.

The experimental part consists of setting up a universal flow independent of inlet conditions. The velocity profiles, for that universal flow, measured using both pitot tube and hot wire are found to be in good agreement with Glauert's prediction. The growth is nearly the same as the two-dimensional wall jet over a circular cylinder, implying that lateral stretching of the turbulent eddies increases the entrainment. The flow breaks away from the sphere close to the rear and hence an axi-symmetric jet forms downstream. Hot wire measurements indicate that the mean velocity profile becomes similar to a conventional axi-symmetric jet about three sphere diameters downstream of the nozzle exit. The longitudinal turbulence, however, does not attain similarity up to seven sphere diameters which was the range of investigation.

The aim of the theoretical part is to identify the contribution of the various terms in the momentum equations. This is achieved by applying Newman's first order analysis and a higher order one, both of which assume a 'top hat' profile for the mean velocity, and the measured rate of growth. Reasonable predictions are obtained by the first analysis for surface pressure and maximum velocity. Better predictions are obtained by the higher order analysis; the latter also predicts the existing two-dimensional measurements fairly accurately.

Axi-Symmetric Turbulent Wall Jet over a Sphere

by

N.A. Sidky

A thesis submitted to the Faculty of Graduate Studies and Research in partial fulfillment of the requirements for the degree of Master of Engineering.

Department of Mechanical Engineering
McGill University
Montreal, Quebec

March. 1970

Summary

The incompressible wall jet over the surface of a sphere has been investigated both experimentally and theoretically.

The experimental part consists of setting up a universal flow independent of inlet conditions. The velocity profiles, for that universal flow, measured using both pitot tube and hot wire are found to be in good agreement with Glauert's prediction. The growth is nearly the same as the two-dimensional wall jet over a circular cylinder, implying that lateral stretching of the turbulent eddies increases the entrainment. The flow breaks away from the sphere close to the rear and hence an axi-symmetric jet forms downstream. Hot wire measurements indicate that the mean velocity profile becomes similar to a conventional axi-symmetric jet about three sphere diameters downstream of the nozzle exit. The longitudinal turbulence, however, does not attain similarity up to seven sphere diameters which was the range of investigation.

The aim of the theoretical part is to identify the contribution of the various terms in the momentum equations. This is achieved by applying Newman's first order analysis and a higher order one, both of which assume a 'top hat' profile for the mean velocity, and the measured rate of growth. Reasonable predictions are obtained by the first analysis for surface pressure and maximum velocity. Better predictions are obtained by the higher order analysis; the latter also predicts the existing two-dimensional measurements fairly accurately.

SOMMAIRE

Cette thèse contient un ensemble de résultats expérimentaux et une analyse théorique concernant un jet pariétal incompressible évoluant sur une sphère.

La partie expérimentale consiste à établir un écoulement universel indépendant des conditions d'admission. Les profils de vitesse moyenne, mesurés grâce à un tube de pitot et à un anémomètre à fil chaud confirment les resultats prédits par Glauert. L'évolution linéaire de la largeur du jet est presque identique à celle d'un jet pariétal sur un cylindre, ceci implique une accélération de l'entrainement due à un étirage latéral des tourbillons turbulents. Le décollement s'effectue à un angle près de 155^{o}, et par suite, un jet de révolution se forme en aval. Quelques mesures à l'anémomètre ont permis de constater que l'écoulement moyen atteint un état d'équilibre après une distance à la buse de trois diamètres de sphère; par contre l'écoulement turbulent en requiert plus de sept diamètres, ce qui dépasse la zone étudiée.

Le but de la partie théorique est d'évaluer la contribution des différents termes de l'équation de quantités de mouvement. Ceci est obtenu par l'analyse au premier ordre de Newman, ainsi qu'une autre d'ordre supérieur. Toutes deux supposent des profils de vitesse moyenne de forme rectangulaire et l'évolution mesurée de la largeur du jet. L'analyse au premier ordre prédit, la pression sur la surface et la vitesse maximale, d'une manière satisfaisante. L'analyse d'ordre supérieur, outre des resultats plus précis, prédit les mesures bi-dimensionnelles, qui existaient, quasiment exactes.

Acknowledgements

The author is deeply indebted to Dr. B.G. Newman for his guidance, advice and help throughout the course of this work.

Numerous suggestions and valuable help given by Mr. A.A. Gustavsen, during the design and construction of the apparatus are very much appreciated.

The advice and criticism of co-workers in the Aerodynamics Group as well as the keen interest shown by Mr. D.B. Garland of The De Havilland Aircraft of Canada Ltd., is also appreciated.

Thanks are due to Mrs. T. Miller for typing the manuscript.

The work was supported by the Defence Research Board of Canada under D.R.B. Grant Number 9551-12.

Table of Contents

Notation

(i) Roman Alphabet

a	-	radius of sphere
a'	-	radius of Fekete's cylinder
b	-	gap width
b'	-	slot width in Fekete's cylinder
C	-	skin friction coefficient $= \dfrac{\tau_w}{\frac{1}{2}\rho U_m^2}$
C'	-	shear stress coefficient $= \dfrac{-\tau}{\rho U_m^2}$
d	-	nozzle diameter
D	-	nozzle diameter in Bradshaw's experiment
F	-	force exerted by the sphere
h	-	scaling factor of the orthogonal co-ordinates
J_i	-	jet momentum out of the nozzle
J_o	-	jet momentum far downstream of the sphere
K	-	constant in equations (2-16) and (2-17) $= \dfrac{\overline{u^2} - \overline{v^2}}{\overline{uv}}$
n	-	exponent for inner boundary-layer profile
p	-	static pressure
p_e	-	static pressure at the edge of the wall jet
p_o	-	stagnation pressure in plenum chamber
p_s	-	static pressure at surface of sphere or cylinder
p_∞	-	static pressure of surrounding fluid
r	-	radius from centre of flat surface in Bradshaw's experiment
Re	-	Reynolds number $= \left[\dfrac{(p_o - p_\infty)\, bd}{\rho\, \nu^2}\right]^{1/2}$

u	-	turbulent velocity component in the U direction
U	-	mean velocity component in the streamwise direction tangential to the sphere or in the wake
U_1	-	square profile velocity
U_m	-	maximum jet velocity
v	-	turbulent velocity component in the V direction
V	-	radial mean velocity component
V_e	-	radial mean velocity component at the edge of the wall jet
w	-	turbulent velocity component in the W direction
W	-	mean velocity component in the transverse direction tangential to the sphere
x	-	distance along the surface $= a\theta$
X	-	distance from the plane of the nozzle measured along the centre line of flow
X_o	-	position of hypothetical origin from the plane of the nozzle measured along the centre line of flow
y	-	distance measured from and perpendicular to sphere
y_1	-	width of square velocity profile
y_m	-	distance from surface where $U = U_m$
$y_{m/2}$	-	distance from surface or flow centre line where $U = \frac{1}{2} U_m$

(ii) Greek Alphabet

α	-	co-ordinate of a point
ϵ	-	perturbation parameter $= \frac{y_{m/2}}{a}$
θ	-	angular distance measured from the centre line of flow
θ_{sep}	-	angular position of separation
ν	-	kinematic viscosity of the fluid
ρ	-	density of the fluid

τ	-	shear stress $= -\rho\ \overline{uv}$
τ_m	-	shearing stress where $U = U_m$
τ_w	-	surface skin friction
ϕ	-	meridional angle measured from the horizontal plane

(iii) Subscripts

1, 2 and 3 in section 2.2 refer to the three axes in the curvilinear orthogonal system used.

1. Introduction

The numerous practical applications, hydraulic and aeronautic, which involve the flowing of a jet over a solid surface, to which Glauert ascribed the name 'Wall Jet', have led many researchers to investigate this type of flow.

A theory was developed by Glauert (1956) for both radial and two-dimensional, laminar and turbulent, plane wall jets using a similarity-type solution. In order to determine a suitable variation of eddy viscosity across the flow for the turbulent wall jet, he considered a hybrid structure in which the eddy viscosity distribution near the wall is taken from the empirical formula due to Blasius (1912) for flow in a pipe and the eddy viscosity in the outer layer is considered to be constant over the cross-section, following Prandtl's hypothesis. By 'matching' the two parts at the peak velocity, he obtained a solution for the velocity profile. This theory was followed by a number of others, most of which use integral techniques. These integral methods for calculating the growth of a plane wall jet in still surroundings have been developed by Myers et al. (1963), by Gartshore and Hawaleshka (1964) and others. Gartshore and Newman (1969) gave a good review of the existing integral techniques and developed a more sophisticated one for calculating the growth of a turbulent wall jet in streaming flow. This method incorporates four integral-momentum equations taken from the wall to various points in the flow. By including some empiricism, based on the large-eddy equilibrium hypothesis to calculate the shear stress at the limits of the integrals and by assuming a four-parameter velocity profile, they obtained satisfactory predictions.

Previous experimental investigations dealt exclusively with the turbulent case as it is the most frequently encountered in practice. These investigations considered three types of wall jets: the plane, the cylindrical and the radial one. The plane wall jet was originally explored experimentally, well before Glauert's analysis, by Förthmann (1936). More recently, experimental studies were performed by Sigalla (1958), Bradshaw and Gee (1960), Schwarz and Cosart (1961), Myers et al (1961), Eskinazi and Kruka (1962), Patel (1962), Gartshore and Haweleshka (1964) and Mathieu et al. (1967). The cylindrical wall jet was examined by Lawrence (1964) and Starr and Sparrow (1967). Experiments on the radial wall jet were carried out by Bakke (1957), Bradshaw and Love (1961) and Tsuei (1962). The latter experiments, being pertinent to the present work, will be discussed in more detail.

Bakke studied a radial wall jet of air emanating from a pipe, 28.4 mm. in diameter, placed at right angles to a smooth plate. The exit of the pipe was at one half of its diameter above the plate. He found the velocity profiles to confirm Glauert's prediction satisfactorily. The growth $\left(\frac{dY_{m/2}}{dx}\right)$ of the wall jet was 0.069. Bradshaw and Love looked at the same configuration but with a nozzle having a diameter, D = 1 in., placed at '18D' above the plate. The growth of the developed radial wall jet was 0.0885 which is surprisingly high when compared with Bakke's value. The discrepancy between the two values for the growth may be explained as follows:

1. The effective origin of the wall jet in Bradshaw's experiment is at '0.6D' from the stagnation point, which represents the fifth of the radius of the impinging jet. This may result in a growth different from that of a jet having its origin at the stagnation point, as was the case in Bakke's experiment. It is to be noted also that the dynamic pressure contours in the stagnation region, for Bradshaw's exhibited a certain deviation from axial symmetry.

2. Bradshaw stated that "slight changes in the shape of profiles are detectable out to the maximum radius, r = 20D, at which measurements were made, but for practical purposes the wall jet is fully developed at $\frac{r}{D} = 8$"; this conclusion is of doubtful validity even for the mean velocity. Rather interestingly, if the point for '$\frac{r}{D} = 8$' is neglected, it would be possible to draw a straight line with Bakke's slope through Bradshaw's three remaining points (see Fig. 7, page 8, Bradshaw et al. (1961)).

Tsuei carried out a complete experimental investigation including measurements of the turbulence intensities which were not considered by Bakke or Bradshaw. He obtained a growth for his jet close to Bakke's value.

In conjunction with the aforementioned wall jets, the tendency of a jet to adhere to and follow the curvature of a solid surface should be pointed out. This phenomenon, which is accompanied by a significant pressure difference across the jet, is often referred to in the literature as the 'Coanda effect'. A review of its various applications, configurations and investigators is well summarized by Wille and Fernholz (1965). Newman (1961), Nakaguchi (1961) and Fekete (1963) investigated the turbulent flow around a circular cylinder, while Sawyer (1962), Guitton (1965) and Giles et al. (1966) examined the turbulent flow around a logarithmic spiral as well.

Laminar solutions for such flows were subsequently obtained by Wygnanski and Champagne (1968), while the turbulent cases were first considered by Newman (1961), Nakaguchi (1961), Sawyer (1962) and Guitton (1964). The configuration which is most related to the present investigation is the flow over a circular cylinder. A theoretical approach for that flow was suggested by Newman (1961) which predicts the surface pressure distribution and the maximum velocity decay over the cylinder. He made the following assumptions:

1. The mean velocity profiles are similar over the cylinder, at least for a considerable distance, and

can be replaced by a uniform velocity profile having the same mass flow and the same momentum.

2. The effect of skin friction on the change of jet momentum is negligible.

3. The radial mean velocity "V" is small compared to the circumferential mean velocity "U", and the width of the jet "$Y_{m/2}$" is much less than the radius of the cylinder.

Using the above assumptions and the experimental growth of the wall jet, Newman predicted the maximum velocity decay and the surface pressure distribution. The former quantity agreed well with experiments while the latter was higher than the experimental one.

Nakaguchi (1961), independently, tried another approach which can be summarized as follows:

1. He assumed similarity of mean velocity profiles so that the non-dimensional velocity profile can be represented by a half free jet on the basis that the boundary layer is negligible.

2. The shear stress can be related to an eddy viscosity which is constant across the flow, as was done by Görtler (1942) for a free jet.

3. He assumed that the wall jet is self preserving and

thus has a turbulence eddy structure which is related non-dimensionally to local parameters which do not change significantly with "x", as stipulated by Townsend (1956) for self-preserving flows.

4. He formulated a relation for the growth of the jet assuming that it is proportional to the radial turbulent velocity component "v", which in turn is proportional to the centrifugal pressure change across the flow. The constants of proportionality were established experimentally.

Fekete (1963) compared both approaches and found that Newman's proved to be more useful in the light of its simplicity. Newman (1969) also made a comparison between the existing theories for the flow over a circular cylinder and showed that his approach is the most successful to predict that flow. It is to be remembered, however, that these theories are applicable if the slot width "b'" is small (but not too small for then the surface friction would become important) compared to the radius "a'" of the cylinder. The case where $\frac{b'}{a'}$ is not small has been discussed by Newman (1969).

The initial purpose of the present work was to investigate both theoretically and experimentally, the axi-symmetric flow of a turbulent wall jet around a sphere. Possible practical applications of such a flow are:

i) The stabilization of flames in burners

ii) The development of axi-symmetric or near-axi-symmetric fluidic devices

iii) The attenuation of jet velocities during the ground testing of aircraft and other machines.

The experimental investigation involved blowing a 2 in. round jet over an 8.5 in. plastic sphere. As the object was to set up a universal flow independent, as far as possible, of inlet conditions, the gap between the jet nozzle and the ball was adjusted so that the wall jet width was zero when extrapolated to $\theta = 0^\circ$, at the front of the ball, where the growth was expected to conform to the radial plane wall jet value at a sufficiently high Reynolds number (Townsend, 1956).

The surface pressure, when referenced to atmospheric, has a negative value near the nozzle due to the flow curvature and exhibits a gradual rise up to $\theta = 90^\circ$, followed by a sudden rise which leads to separation at $\theta = 155^\circ$ when the surface pressure becomes positive at the back of the sphere, due to the curvature of the flow there. This behaviour suggested the possibility of a resultant force on the ball <u>towards</u> the nozzle, which would result in thrust augmentation of the jet. This suggestion was also supported by a simple demonstration in which a sphere was supported underneath a circular jet (Fig. 1).

The tests were therefore extended for different values of the gap width to investigate the momentum balance and the possibility of thrust augmentation. Results are presented for four gap widths ranging from 0.048 in. to 0.5 in. and for Reynolds numbers based on jet momentum varying between 1.26×10^4 and 6.4×10^4.

The theoretical investigation consisted of three different approaches:

1. Modification of Newman's first order, two-dimensional theory for the axi-symmetrical case.

2. Use of an improved version of Newman's theory in which his assumptions of a 'top-hat' velocity profile and an experimental growth are retained, but in which the two-integral momentum equations are not simplified to first order and are solved numerically. The shear stress and turbulence intensities are assumed to have self-similar profiles.

3. Application of a three-parameter velocity profile together with three integral-momentum equations.

It will be seen that the theoretical approach (2) gives reasonably accurate predictions. But its usefulness is not to be judged solely on its ability to predict the flow. Of more importance for future developments is the identification of the contribution of the various terms in the x-momentum and y-momentum equations; the important terms indicate where more detailed work is required.

The theoretical results are presented for both the two-dimensional and axi-symmetric cases and are compared with the experimental results.

2. Theoretical Analysis

2.1 Dimensional Analysis and the Choice of Parameters

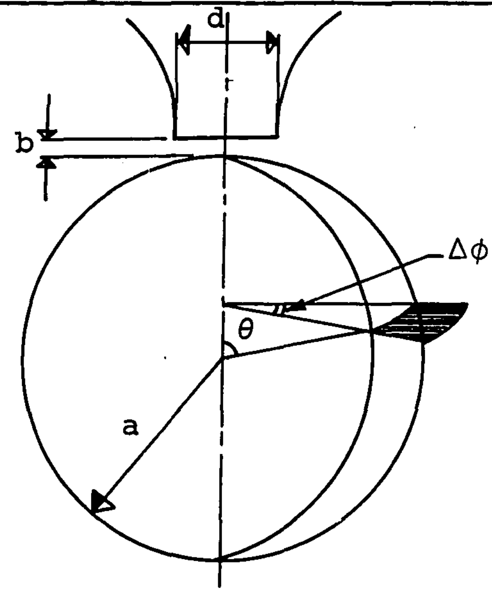

Fig. (2.a)

Following Newman (1961) for $(p_o - p_\infty) \ll p_\infty$ the flow can be treated as being effectively incompressible, therefore the following parameters are sufficient to define it:

$p_o - p_\infty$	the plenum chamber static pressure relative to that of the surroundings
a	the radius of the sphere
d	the internal diameter of the nozzle
θ	the angular distance measured from the front of the sphere
b	the distance between the sphere and the plane of the nozzle
ρ	the density of the fluid
ν	the kinematic viscosity of the fluid

Hence, the flow may be described by four non-dimensional parameters namely:

$$\theta\ ,\quad \frac{b}{a}\ ,\quad \frac{d}{a}\ ,\quad \left[\frac{(p_o-p_\infty)(\text{length})^2}{\rho\ \nu^2}\right]^{1/2}$$

The dominant parameter for turbulent jets and wall jets is the jet momentum (Newman, 1961 and 1969), which in most cases tends to remain constant. However, the streamwise co-ordinate has to be measured from a certain hypothetical origin, so that the same flow would come from an infinitesimally thin slot situated there, and consequently the flow will not depend on the slot width and the jet velocity as individual parameters, but would depend on the jet momentum as in the two-dimensional case. In the present configuration, due to the symmetry of the flow, the streamwise coordinate is measured from the axis of the flow. However, in order to obtain the source effect of a hypothetical origin, the gap width must be adjusted so that the flow appears to originate from a source at the front of the sphere.

Consider a slice of the sphere subtending an angle $\Delta\phi$, as shown in Fig. (2.a). The angular momentum flux from the nozzle for this slice may be expressed as (p_o-p_∞) $bda\Delta\phi$, while the momentum flux would be (p_o-p_∞) $bd\Delta\phi$*. This angular momentum flux, at any angular position "θ", will have approximately the value $(p_\infty-p_s)$ $a^3\sin\theta\Delta\phi$ or $\rho U^2{}_m a^3\theta\sin\theta\Delta\phi$. It is interesting to note that the last two groups include a 'sinθ', which in

---

* It is to be noted that this is an idealized value which agrees also with the actual momentum as measured experimentally at the station $\theta = 15^\circ$ (for details see section 4.2).

fact takes into account the geometry of the sphere and renders the comparison with the case of a cylinder possible.

Therefore, the surface pressure "p_s" at an angular position "θ" may be expressed as follows:

$$\frac{(p_\infty - p_s)\ a^2 \sin\theta \Delta\phi}{(p_o - p_\infty)\ bd\ \Delta\phi} = \text{fn}\left\{\theta\ ,\ \left[\frac{(p_o - p_\infty)\ bd}{\rho\ \nu^2}\right]^{1/2}\right\} \quad (1)$$

For large values of the Reynolds number,

$$Re = \left[\frac{(p_o - p_\infty)\ bd}{\rho\ \nu^2}\right]^{1/2} ,$$

the viscosity may probably be excluded (Newman, 1961) and Eq. (1) reduces to:

$$\frac{(p_\infty - p_s)\ a^2}{(p_o - p_\infty)\ bd} = \text{fn}\ (\theta) \quad (2)$$

However, on physical grounds and in order to compare the results with those of a circular cylinder, Eq. (2) will be written as:

$$\frac{(p_\infty - p_s)\ a^2 \sin\theta}{(p_o - p_\infty)\ bd} = \text{fn}\ (\theta) \quad (3)$$

Similarly the maximum jet velocity coefficient is given by:

$$\frac{\rho\ U^2_m\ a^2\theta\ \sin\theta}{(p_o - p_\infty)\ bd} = \text{fn}\ (\theta) \quad (4)$$

and the position of separation may be expressed by

$$\theta_{sep} = \text{constant} \tag{5}$$

again as in the two-dimensional case.

2.2 Equations of Motion

The equations of motion and continuity for steady, incompressible, turbulent mean flow in a system of orthogonal coordinates in which the coordinates of a point are α_1, α_2, α_3 and the corresponding scaling factors are h_1, h_2, h_3 in the directions 1, 2, 3 respectively, are:*

$$\frac{U_1}{h_1^2}\frac{\partial h_1U_1}{\partial\alpha_1} + \frac{U_2}{h_1h_2}\frac{\partial h_1U_1}{\partial\alpha_2} + \frac{U_3}{h_1h_3}\frac{\partial h_1U_1}{\partial\alpha_3} - \frac{U_1^2+\overline{u_1^2}}{h_1^2}\frac{\partial h_1}{\partial\alpha_1} - \frac{U_2^2+\overline{u_2^2}}{h_1h_2}\frac{\partial h_2}{\partial\alpha_1} - \frac{U_3^2+\overline{u^2_3}}{h_1h_3}\frac{\partial h_3}{\partial\alpha_1} + \frac{1}{h_1^2h_2h_3}\left[\frac{\partial}{\partial\alpha_1}(h_1h_2h_3\overline{u_1^2}) + \frac{\partial}{\partial\alpha_3}(h_1^2h_2\overline{u_1u_3}) + \frac{\partial}{\partial\alpha_2}(h_1^2h_3\overline{u_1u_2})\right] = -\frac{1}{\rho h_1}\frac{\partial p}{\partial\alpha_1} \qquad (2\text{-}1)$$

$$\frac{1}{h_1h_2h_3}\left[\frac{\partial}{\partial\alpha_1}(h_2h_3U_1) + \frac{\partial}{\partial\alpha_2}(h_3h_1U_2) + \frac{\partial}{\partial\alpha_3}(h_1h_2U_3)\right] = 0 \qquad (2\text{-}2)$$

Where in Eq. (2-1), the viscous terms have been neglected in comparison to the inertia terms (Goldstein, 1938) and this equation is in the direction "1", the two others are obtained by cyclic change of the suffices.

---

* The only source of literature for the above equations is Townsend (1956). Townsend's equations contain a printing error, however, as was revealed when these were checked by converting the laminar equations given in Goldstein (1938) and Rouse (1959).

Choosing the coordinates as shown in the opposite figure we have:

$$\alpha_1 = x \quad \alpha_2 = y \quad \alpha_3 = \phi$$
$$h_1 = \frac{a+y}{a} \quad h_2 = 1 \quad h_3 = \frac{a+y}{a}\sin\frac{x}{a} = \frac{a+y}{a}\sin\theta$$
$$U_1 = U \quad U_2 = V \quad U_3 = W$$
$$u_1 = u \quad u_2 = v \quad u_3 = w$$

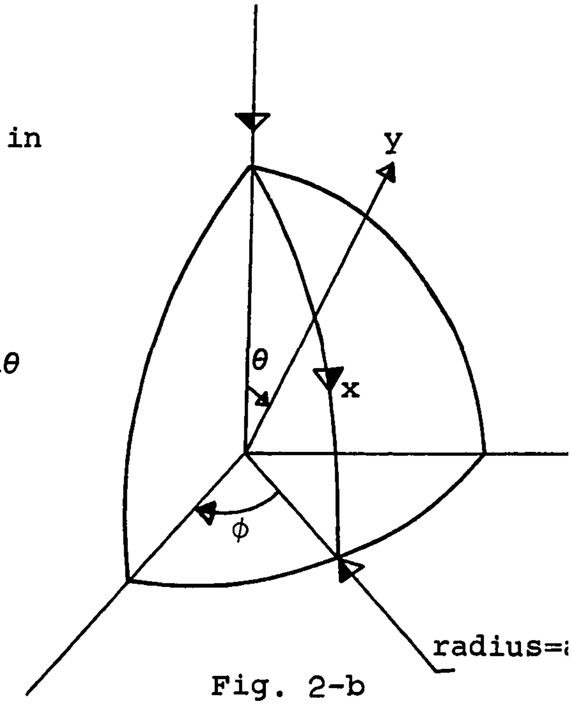

Fig. 2-b

Substituting in Eqs. (2-1) and (2-2) we get

$$U\frac{\partial U}{\partial x} + \frac{a+y}{a}V\frac{\partial U}{\partial y} + \frac{UV}{a} + \frac{\overline{u^2}-\overline{w^2}}{a}\cot\theta + 3\,\frac{\overline{uv}}{a} = -\frac{\partial}{\partial x}\left(\frac{p}{\rho} + \overline{v^2}\right) - \frac{\partial}{\partial x}\left(\overline{u^2}-\overline{v^2}\right) - \frac{a+y}{a}\frac{\partial\overline{uv}}{\partial y} \qquad (2\text{-}3)$$

$$U\frac{\partial V}{\partial x} + \frac{a+y}{a}V\frac{\partial V}{\partial y} - \frac{U^2}{a} + \frac{\partial\overline{uv}}{\partial x} + \frac{2\overline{v^2}-\overline{u^2}-\overline{w^2}}{a} + \frac{\overline{uv}}{a}\cot\theta = -\frac{a+y}{a}\frac{\partial}{\partial y}\left(\frac{p}{\rho} + \overline{v^2}\right) \qquad (2\text{-}4)$$

$$\frac{\partial}{\partial x}\left[(a+y)U\sin\theta\right] + \frac{\partial}{\partial y}\left[\frac{(a+y)^2}{a}V\sin\theta\right] = 0 \qquad (2\text{-}5)$$

The usual assumption for free shear flows of neglecting the term $\frac{\partial}{\partial x}(\overline{u^2} - \overline{v^2})$ will be used here.

Making use of the continuity equation (2-5), Eq. (2-3) may be rewritten in a form suitable for integration as follows:

$$\frac{\partial}{\partial x}\left[(a+y)^2 U^2\right] + \frac{\partial}{\partial y}\left[\frac{(a+y)^3}{a}UV\right] + \frac{(a+y)^2}{a}U^2\cot\theta = -\frac{\partial}{\partial x}\left[(a+y)^2\left(\frac{p}{\rho} + \overline{v^2}\right)\right] + \frac{\partial}{\partial y}\left[\frac{(a+y)^3}{a}\frac{\tau}{\rho}\right] \qquad (2\text{-}6)$$

It should be noted that in flows over curved surfaces $\frac{y_{m/2}}{x}$ is of the same order of magnitude as $\frac{y_{m/2}}{a}$ and will be denoted by "ϵ", (except, of course, close to the origin).

2.3 Newman's or First Order Analysis

Using the same assumptions as Newman (1961), Eqs. (2-6) and (2-4) are reduced to:

$$\frac{\partial}{\partial x}\left[(a+y)^2 U^2\right] + \frac{\partial}{\partial y}\left[\frac{(a+y)^3}{a} UV\right] + \frac{(a+y)^2}{a} U^2 \cot\theta = -\frac{\partial}{\partial x}\left[(a+y)^2 \left(\frac{p}{\rho} + \overline{v^2}\right)\right] \qquad (2\text{-}7)$$

and

$$\frac{U^2}{a+y} = \frac{\partial}{\partial y}\left(\frac{p}{\rho} + \overline{v^2}\right) \qquad (2\text{-}8)$$

Denoting the velocity and the width of the 'top hat' velocity profile by $U_1 = \frac{3}{4} U_m$ and $y_1 = \frac{4}{3} y_{m/2}$ respectively, and integrating (2-8) from 0 to y we get

$$\frac{p_\infty}{\rho} - \left(\frac{p}{\rho} + \overline{v^2}\right) = U_1^2 \ln \frac{a + y_1}{a+y} \qquad (2\text{-}9)$$

Substitution of (2-9) in (2-7) and then integration from 0 to ∞ yields

$$U_1^2 \, y_1 \, a \sin\theta = \text{constant} \qquad (2\text{-}10)$$

The last equation has been written to $O(\epsilon)$ i.e. all terms, as well as the logarithmic series in (2-9), involving $\left(\frac{y_1}{a}\right)^2$ or higher order have been neglected.

Interestingly enough, Eq. (2-10) expresses but the constancy of the angular momentum at any angular position "θ", which would be derived directly by considering a slice of the sphere.

Using the experimental growth relation given by (see section 4.2.1)

$$\frac{y_{m/2}}{a\theta} = 0.068 + 0.32\,\frac{y_{m/2}}{a} \qquad (2\text{-}11)$$

equation (2-10) reduces to

$$\frac{\rho U_m^{\,2}\; a^2\theta\; \sin\theta}{(p_o - p_\infty)\; bd} = \text{constant}\;\left(\frac{1}{a\theta} - \frac{0.32}{a}\right)\theta \qquad (2\text{-}12)$$

The surface pressure distribution is then given by Eqs. (2-9), (2-10) and (2-11)

$$\frac{(p_\infty - p_s)a^2\sin\theta}{(p_o - p_\infty)\; bd} = \frac{9}{16}\;\text{constant}\;\left(\frac{1}{a\theta} - \frac{0.32}{a}\right).\ln\left\{1 + \frac{4}{3}\,\frac{0.068}{a}\left[\frac{1}{a\theta} - \frac{0.32}{a}\right]^{-1}\right\} \qquad (2\text{-}13)$$

The 'constant' in the above equations will be evaluated in section 4.5.

2.4 Improved Newman's or Higher Order Analysis

Newman (1961) suggested that the inertia terms in the y-momentum equation should be retained, in order to get a better prediction of the surface pressure, on the ground that they are the only two terms responsible for the discrepancy in surface pressure. Therefore, it has been decided to keep the analytically convenient assumption of a 'top hat' velocity profile and deal with the complete momentum equations. Assumptions have to be made, however, for the skin friction and normal stresses. As the main aim for this analysis was to identify the contribution of the various terms in the y-momentum equation, a simple assumption was adopted, namely that the shear stress and turbulence intensities have universal profiles and scale with $y_{m/2}$ and U_m.

As the first order analysis proved to be reasonably accurate in predicting the maximum velocity decay and as the incorporation of the full y-momentum equation for the pressure term in the x-momentum equation proved to be analytically tedious, Eq. (2-9) was used to estimate the pressure terms. The pressure on the surface was, however, subsequently worked out using the full y-momentum equations (unknown turbulence terms disappear).

Therefore Eq. (2-10) now reads

$$C_1 \frac{dU_1^2}{dx} + C_2 U_1^2 = 0 \qquad (2\text{-}14)$$

where

$$C_1 = 2\frac{y_1}{a} + 2\left(\frac{y_1}{a}\right)^2 + \frac{2}{3}\left(\frac{y_1}{a}\right)^3 + \ln\left(1+\frac{y_1}{a}\right)$$

$$C_2 = \frac{1}{a}\left\{\left[2+4\frac{y_1}{a} + 2\left(\frac{y_1}{a}\right)^2 + \frac{a}{a+y_1}\right]\frac{dy_1}{dx} + \left[3\frac{y_1}{a} + 3\left(\frac{y_1}{a}\right)^2 + \left(\frac{y_1}{a}\right)^3\right]\cot\theta + \frac{8}{3}C\right\}$$

and C in the last equation is the skin friction coefficient $\left(\frac{\tau_w}{\frac{1}{2}\rho U^2{}_m}\right)$, taken to be 0.005 (Guitton, 1969).

Equation (2-14) was solved numerically using a 4th order Runge-Kutta technique.

Now, the surface pressure over the sphere is obtained by integrating the y-momentum equation (2-4). Measurement in a radial plane wall jet (Tsuei, 1963) indicates that the term $(\overline{v^2} - \overline{w^2})$ is negligible compared to U^2. Using this result Eq. (2-4) becomes

$$\frac{a}{a+y}\frac{U\partial V}{\partial x} + \frac{V\partial V}{\partial y} - \frac{U^2}{a+y} = -\frac{\partial}{\partial y}\left(\frac{p}{\rho} + \overline{v^2}\right) + \frac{a}{a+y}\frac{\partial}{\partial x}\left(\frac{\tau}{\rho}\right) + \frac{\overline{u^2}-\overline{v^2}}{a+y} + \frac{\tau/\rho}{a+y}\cot\theta \qquad (2\text{-}15)$$

Integration of Eq. (2-15) from 0 to ∞ yields

$$\int_0^\infty \frac{a}{a+y}\frac{U\partial V}{\partial x}dy + \frac{V_e^2}{2} - \int_0^\infty \frac{U^2}{a+y}dy = -\frac{p_e}{\rho} + \frac{p_s}{\rho} + \int_0^\infty \frac{a}{a+y}\frac{\partial}{\partial x}\left(\frac{\tau}{\rho}\right)dy + \int_0^\infty \frac{\tau/\rho}{a+y}(\cot\theta - K)\,dy \qquad (2\text{-}16)$$

where

V_e and p_e are the radial outflow velocity (physically negative) and static pressure at the edge of the wall jet, related through Bernoulli's equation by

$$p_\infty = p_e + \frac{1}{2}\rho V_e^2$$

and

$$K = \frac{\overline{u^2} - \overline{v^2}}{\overline{uv}} \simeq 1 \qquad \text{(Guitton, 1970)}$$

In order to evaluate the first integral in Eq. (2-16) the continuity equation (2-5) is integrated from 0 to y, yielding

$$V = \left[\frac{a^3}{2(a+y)^2} - \frac{a}{2}\right]\left[\frac{dU_1}{dx} + \frac{U_1}{a}\cot\theta\right]$$

Therefore

$$\frac{\partial V}{\partial x} = \left[\frac{a^3}{2(a+y)^2} - \frac{a}{2}\right]\left[\frac{d^2U_1}{dx^2} + \frac{1}{a}\frac{dU_1}{dx}\cot\theta - \frac{U_1}{a^2}\operatorname{cosec}^2\theta\right]$$

Hence Eq. (2-16) gives

$$\frac{p_\infty - p_s}{\rho} = \ln\frac{a+y_1}{a}\left\{U_1^2 - \frac{U_1^2}{2}\operatorname{cosec}^2\theta + \frac{a^2}{2}U_1\frac{dU_1^2}{dx^2} + \frac{a}{4}\frac{dU_1^2}{dx}\cot\theta - a\,C'\frac{dU_1^2}{dx} - (\cot\theta - K)\,C'\,U_1^2\right\}$$
$$- \frac{a^2}{4}\left[U_1\frac{d^2U_1}{dx^2} + \frac{1}{2a}\cot\theta\frac{dU_1^2}{dx} - \frac{U_1^2}{a^2}\operatorname{cosec}^2\theta\right]\left[1-\left(1+\frac{y_1}{a}\right)^{-2}\right]$$

where

$$C' = \frac{\overline{uv}}{U_1^2} = 0.0268 \qquad \text{(Tsuei, 1963)}$$

and $\frac{d^2U_1{}^2}{dx^2}$ is found by differentiating Eq. (2-14) w.r.t. "x" as follows

$$C_1 \frac{d^2U_1{}^2}{dx^2} + \frac{C_2}{a}\frac{dU_1{}^2}{dx} + \frac{C_3}{a^2} U_1{}^2 = 0 \qquad (2\text{-}18)$$

where

$$C_1 = 2\frac{y_1}{a} + 2\left(\frac{y_1}{a}\right)^2 + \frac{2}{3}\left(\frac{y_1}{a}\right)^3 + \ln\left(1+\frac{y_1}{a}\right)$$

$$C_2 = 2\left[2+4\frac{y_1}{a} + 2\left(\frac{y_1}{a}\right)^2 + \frac{a}{a+y_1}\right]\frac{dy_1}{dx} + \left[3\frac{y_1}{a}+3\left(\frac{y_1}{a}\right)^2+\left(\frac{y_1}{a}\right)^3\right]\cot\theta + 0.0025 \times \frac{16}{3}$$

$$C_3 = \left[4+4\frac{y_1}{a} - \left(\frac{a}{a+y_1}\right)^2\right]\left(\frac{dy_1}{dx}\right)^2 + \left[2+4\frac{y_1}{a} + 2\left(\frac{y_1}{a}\right)^2 + \frac{a}{a+y_1}\right] a \frac{d^2y_1}{dx^2} + \left[3+6\frac{y_1}{a} + 3\left(\frac{y_1}{a}\right)^2\right]\cot\theta \frac{dy_1}{dx} - \left[3\frac{y_1}{a} + 3\left(\frac{y_1}{a}\right)^2+\left(\frac{y_1}{a}\right)^3\right]\operatorname{cosec}^2\theta$$

It is worth noting that if we wanted to evaluate $\frac{dp}{dx}$ in Eq. (2-7) from (2-15) we would get terms in $\frac{d^3U_1}{dx^3}$. This complication tends to justify the use of Eq. (2-9) to estimate that term. Its size is, however, the main consideration as will be shown later (section 4.5).

This analysis has been applied for the case of a cylinder in order to give another comparison. The integrals of the momentum equations are given below:

$$\frac{dU_1{}^2}{dx}\left[\frac{y_1}{a} + \frac{1}{2}\left(\frac{y_1}{a}\right)^2 + \ln\left(1+\frac{y_1}{a}\right)\right] + \frac{U_1{}^2}{a}\left[\left(1+\frac{y_1}{a} + \frac{a}{a+y_1}\right)\frac{dy_1}{dx} + \frac{16}{9}x.005\right] = 0 \qquad (2\text{-}19)$$

$$\frac{p_\infty - p_s}{\rho} = \ln\frac{a+y_1}{a}\left[U_1{}^2 + a^2 U_1\frac{d^2U_1}{dx} - a\,C'\frac{dU_1{}^2}{dx} + KC'\,U_1{}^2\right] \qquad (2\text{-}20)$$

2.5 Full Integral Technique

It is obvious that the improvement which can be brought to the 'Higher Order' analysis, is to consider the momentum equations but with a more realistic velocity profile to enable the prediction of separation. Hence a four-parameter velocity profile was used:

$$\frac{U}{U_m} = \left(\frac{y}{y_m}\right)^{\frac{1}{n}} \qquad \text{from } 0 \text{ to } y_m$$

$$\frac{U}{U_m} = \operatorname{sech}^2\left[0.88 \; \frac{y-y_m}{y_{m/2}-y_m}\right] \quad \text{from } y_m \text{ to } \infty$$

In this case we have U_m, $y_{m/2}$, y_m, p_s and n as unknowns, implying the need for five equations. As a first step, it was decided to freeze the exponent "n" and assign to it the value 11, and to use the experimental growth relation given by Eq. (2-11). Therefore, we are left with 3 unknowns for which three equations were formed as follows:

1. The integral of the y-momentum equation (2-4) from 0 to ∞
2. The integral of the x-momentum equation (2-3) from 0 to y_m
3. The integral of the x-momentum equation from y_m to ∞

Empirical formulae were used for the shear stress variation across the flow as well as the skin friction. The three equations are given in Appendix II.

This method, however, did not seem to be promising as the equations were very complicated and the numerical solution proved to be unstable. The reason for this instability was that the value of $\frac{dp_s}{dx}$ was calculated through an iteration procedure which does not match with the sensitivity of the surface pressure.

A modification of this procedure, would be the evaluation of $\frac{dp_s}{dx}$ by differentiating the full radial y-momentum equation. This would result in six ordinary differential equations to be solved simultaneously. This work was abandoned as it was analytically very tedious.

3. Details of the Experimental Investigation

The experimental apparatus is shown both schematically and photographically in Figures 2, 3 and 4, and is described in Appendix I.

3.1 Calibrating and Proving the Apparatus

3.1.1 Checks with Sphere removed : Steadiness, Metering of the Flow and Axial Symmetry

In order to meter the flow emanating from the nozzle, the pressure drop across one of the perforated plates (1) or (2) was used. When the sphere was removed, the supporting pipe was replaced by an identical one plugged at the end. Before metering the flow, it was necessary to check for steadiness and axial symmetry. The steadiness of the flow was checked by viewing the signal from a hot wire placed at the exit of the nozzle. With the perforated plate (3) at the mid span of the expansion, the honeycomb (2) and a constant bleed at the outlet of the centrifugal blower, a reasonably steady flow was achieved (indicated by the disappearance of previously observed bursts of turbulence). The axial symmetry of the cylindrical wall jet was checked by measuring velocity profiles at four meridional planes around the pipe and the results are shown in Fig. 5.

The mass flow was obtained from the measured pressure drop across the perforated plate (1) by relating this to the integrated velocity profile at the outlet of the nozzle as shown in Fig. 6. The downstream perforated plate (1) was chosen because the upstream (2), once the sphere is installed, was in the wake of slight disturbances caused by the pressure leads.

3.1.2 <u>Checks with Sphere installed</u> : <u>Axial Symmetry</u>

The sphere was installed, and geometrical axial symmetry was achieved by the fine adjustment of the screws on the supporting perforated plates (1) and (2) (see Appendix I).

Aerodynamic axial symmetry was then checked by three different sets of measurements:

a) Surface pressure distributions, taken at four meridional planes. These were found to vary by no more than 1% of the mean value as shown in Fig. 7.

b) Total pressure profiles, measured at four meridional planes. There was no detectable asymmetry as shown in Fig. 8.

c) Skin friction on the sphere, measured by a 0.020 in. Preston tube at every 10° interval along the diameter $\theta = 90^\circ$. This was found to vary by less than 3% of the mean value (Fig. 9).

It is to be mentioned that the first check was quite reliable as the surface pressures proved to be extremely sensitive to any asymmetry and they were easily displayed on a multitube monometer, of 1:2 inclination, fitted with a freezing device. The third check was the decisive one as it constitutes the most severe test for the symmetry of a flow (Patel, 1964).

3.1.3 Setting the Universal Flow

After axial symmetry was verified, the growth of the wall jet was measured using a 0.022 in. diameter pitot tube. The static pressure was assumed to vary linearly from the value at the surface to that of the atmosphere at the point where the total pressure falls to zero with reference to atmospheric (Fekete, 1963).

This was repeated for different gap widths until the wall jet width extrapolated backwards to zero at the front of the sphere $\theta = 0^\circ$, as shown in Fig. 10-1. Further the setting was strongly confirmed by the fact that the growth at $\theta = 0^\circ$ conformed with Bakke's measurements on a plane radial wall jet (Fig. 10-2) at a sufficiently high Reynolds number $\left(\frac{U_m(y_{m/2}-y_m)}{\nu} > 5000\right)$.

This case, $\frac{b}{a} = 0.046$, was then intensively studied. This work is described in the following section.

3.2 Experiments

The surface pressure was measured using a pressure transducer together with a "Scanivalve", the results of which were displayed on a strip chart recorder. The estimated overall accuracy, by which the surface gauge pressure was measured, is better than ± 0.5% of the reading. The results were plotted for different Reynolds numbers, $Re = \left[\frac{(p_0 - p_\infty) bd}{\rho \ \nu^2} \right]^{1/2}$, ranging from 1.26×10^4 to 6.4×10^4. The limiting value, beyond which the flow appeared to be independent of Re, was chosen to be 4×10^4, at which all subsequent measurements were performed. Presumably, Reynolds number independence is not attained if $\frac{b}{a}$ is too small for then the surface friction would become important (Newman, 1969).

Mean velocity profiles on the sphere were measured with both a normal hot wire using a DISA linearized, constant-temperature anemometer, and a 0.010 in. flat pitot tube assuming a linear variation of static pressure across the flow, at $\theta = 50°$, $70°$, $100°$, $120°$ and $140°$. The displacement for the flat pitot tube was found to be 0.0015 in. by comparing its readings with those of a normal hot wire taken in a plane wall jet and, as its lip was sharpened, the estimated sensitivity for pitch was less then 0.15% per degree at one inch from the wall, where the angle of attack was estimated to be three degrees.

Special care was taken to determine when the hot wire was at the surface of the sphere. A 0.001 in. feeler gauge was held against the sphere and attached to one terminal of an oscilloscope, the second terminal being connected to the probe (the sphere, being made of plastic, is electrically insulating). Therefore, when the electrical pick-up on the screen disappeared, the probe was known to be at 0.001 in. from the surface. This adjustment had to be done very carefully to avoid breaking the wire.

The position of separation was determined by using a very light tuft mounted at the end of a fine wire. For high Re, the accuracy was $\pm 3^\circ$ while for low Re ($Re < 3 \times 10^4$), the velocities were so small that the point of separation could not be determined with reasonable accuracy. Another technique (Begg, 1967) was tried, using a fine needle with a transverse hole through which a short cotton thread was inserted, but similar difficulties were experienced. It was therefore decided to abandon any measurements for separation at low Re.

Mean velocity profiles were taken behind the sphere using pitot tube and normal hot wire at nine stations ranging from 1.3 to 7.3 sphere diameters from the nozzle exit.

Longitudinal turbulence intensities were measured by integrating a linearized signal for 50 sec. at the aforementioned stations. The results were analysed to first order in $\frac{\sqrt{\overline{u^2}}}{U}$ and no corrections for high intensity turbulence, usually of the order of 5% at $\frac{y}{y_{m/2}} = 1.5$ (Guitton, 1968), were applied.

In order to check for the momentum balance three quantities had to be estimated. The force on the sphere was obtained by integrating the surface pressure, the momentum out of the nozzle was based on the stagnation pressure in the plenum chamber, and the momentum in the wake was calculated by integrating the mean velocity profile there.

The momentum balance was also checked for two other gap widths, $\frac{b}{a}$ = 0.0116 and 0.1175.

The growth of the free jet was obtained and the variation of its hypothetical origin with the gap width was also determined for these cases.

4. Discussion of Results

4.1 Qualitative Description of the Flow

Figure (11) indicates the behaviour of the flow around the sphere. The jet emanating from the nozzle is thin and forms a vena contracta* close to the edge of the nozzle. As it proceeds around the sphere, the width decreases, up to $\theta = 90°$, due to lateral spreading, but it also increases as a result of air being entrained from the surroundings. Thus, the mean velocity on the sphere, having a profile typical of a wall jet, decreases and the surface pressure, which was negative at the beginning due to the curvature of the flow, starts to rise as the velocities fall causing separation at an angular position $\theta_{sep} = 155°$.

Due to the geometry of the sphere, namely the reduction in surface area beyond the diameter $\theta = 90°$, the separated flow tends to meet again at the back of the sphere after forming a cavity of recirculating flow which we will call a bubble. The average length of that bubble is about one fifth of the sphere diameter.

The flow expands again in a round jet with a mean velocity profile containing initially a wake due to the flow over the sphere - a wake which subsequently disappears far downstream leaving only turbulence as an indicator that the flow has been

---

* Where flow is developed such that it is plausible to assume that the pressure varies linearly across the flow, but a significant core still exists.

disturbed. The round jet is also a great deal wider with lower velocities than it would be if the flow from the nozzle were not disturbed by the sphere.

4.2 Choice of Parameters used in forming the Non-Dimensional Pressure and Velocity Coefficients

In section (2.1) it was shown that the non-dimensional pressure and velocity coefficients can be conveniently stated as $\frac{(p_\infty - p_s)\ a^2 \sin\theta}{(p_o - p_\infty)\ bd}$ and $\frac{\rho U^2{}_m\ a^2\theta \sin\theta}{(p_o - p_\infty)\ bd}$ respectively. The factor '$\sin\theta$' was included to account for the geometry of the sphere and makes a comparison with the case of a circular cylinder possible. It was also mentioned that $(p_o - p_\infty)\ bd\ \Delta\phi$ represents the momentum flux from the nozzle for a slice of the sphere subtending an angle '$\Delta\phi$'. This quantity is estimated by the following interpretation of the experiment; $(p_o - p_\infty)$ is taken to be the gauge stagnation pressure in the plenum chamber, "b" is the distance between the plane of the nozzle and the plane of intersection of the sphere with the supporting pipe, and "d" is the diameter of the nozzle. This $(p_o - p_\infty)\ bd\ \Delta\phi$ is an idealized value for the actual momentum at the vena contracta. Both quantities, however, were found to be equal within 1%. This is not too surprising when it is realized that $(p_o - p_\infty)$ is an over-estimation for $\frac{1}{2}\rho U^2$ due to the curvature of the flow at the exit of the nozzle, while the value of "d" is an under-estimation for the average diameter of the vena contracta at which the vena contracta forms, and "b" is not too far from the actual thickness of the vena contracta.

4.3 Description of Experimental Results

4.3.1 Sphere Measurements

Mean Velocity and Longitudinal Turbulence Profiles

Figures (12) show mean velocity profiles, for $\frac{b}{a} = 0.046$ and $Re = 4 \times 10^4$, measured by pitot tube and interpreted as velocity using a linear variation of static pressure across the flow, and normal hot wire at $\theta = 50°, 70°, 100°, 120°$ and $140°$.

These figures also show the r.m.s. longitudinal turbulence component as a percentage of the local mean velocity, i.e. $\frac{\sqrt{\overline{u^2}}}{U}$.

The outer part of the velocity profile measured by the pitot tube exhibits the error commonly found in curved flow measurements due to the probe misalignment. This is again shown in Fig. 13 where the non-dimensional velocity $\frac{U}{U_m}$ is plotted versus $\frac{y}{y_{m/2}}$ and compared with the theoretical curve of Glauert for $\frac{y}{y_{m/2}} = 0.12$. In the inner part of the profile, there is a slight difference between the experimental results and the theoretical curve which is due in part to the neglect of turbulence intensities in estimating the mean velocity from the measured total pressure.

The normal hot wire results are more accurate in the inner part, while in the outer part there is a slight discrepancy due to the high intensity turbulence which was not taken into account; the error is not large for Guitton (1968) found that the correction does not exceed 5% for a plane wall jet at $\frac{y}{y_{m/2}} = 1.6$. Figures 14 show the non-dimensional velocity $\frac{U}{U_m}$ for the whole profile and the outer part alone and compare these with Glauert's. The agreement is quite satisfactory.

Comparison of turbulence intensities $\frac{\sqrt{\overline{u^2}}}{U}$ is made in Fig. 15 between the present results and those of Fekete (1963) on a circular cylinder (two-dimensional case) and those of Tsuei (1962) on a plane radial wall jet for the same range of $\frac{U_m y_m}{\nu}$, and at approximately the same downstream station.

It is seen from the figure that the three curves are in qualitative agreement and the turbulence intensities, $\frac{\sqrt{\overline{u^2}}}{U}$, in the axi-symmetric wall jet are higher than those in the plane radial wall jet, the latter being higher than those in the two-dimensional wall jet over a circular cylinder. The explanation for this probably lies in the more rapid decay of the velocity "U" in the axi-symmetric case and perhaps in the likely increase of "u" due to the lateral stretching of the eddies.

Growth of Wall Jet

The growth law for the universal flow was obtained by numerically fitting a straight line to the experimental results. This relation and the growth law obtained by Fekete are shown in Fig. 16; they read:

$$\frac{y_{m/2}}{a\theta} = 0.068 + 0.32\, y_{m/2} \qquad \text{Axi-Symmetric}$$

$$\frac{y_{m/2}}{a\theta} = 0.067 + 0.3\, y_{m/2} \qquad \text{Two-Dimensional}$$

It is interesting to note that the two relations are nearly the same, implying that the stretching of the eddies increases the entrainment sufficiently to compensate for the lateral expansion at least up to $\theta = 90°$. This is consistent with the analogy in the behaviour of a plane wall jet and plane radial one for which the growth is 0.067 and 0.068 respectively.

Maximum Velocity and Momentum Decay

The maximum velocity coefficient $\frac{\rho U_m^2 a^2 \theta \sin\theta}{(p_o - p_\infty)\, bd}$ as estimated from the pitot tube and hot wire measurements, is shown in Fig. 17, and is compared with the two-dimensional case. The lateral spreading in the axi-symmetric case up to $\theta = 90°$ is obviously the direct cause of the more rapid decay in velocity; beyond that point the slope of the curve starts to be qualitatively comparable to the two-dimensional case.

Fig. 18 shows the decay for a measure of the momentum, namely $\rho U_m^2\, y_{m/2}\, a \sin\theta$. It is seen that this quantity decays only slowly in the range $0° < \theta < 90°$ and more rapidly beyond this range.

Surface Pressure Distribution

Figures 19 and 20 show the surface pressure distribution plotted non-dimensionally in two different ways, one as

$\frac{(p_\infty - p_s) a^2 \sin\theta}{(p_o - p_\infty)\, bd}$ and the other as $\frac{(p_\infty - p_s)\, a^2}{(p_o - p_\infty)\, bd}$ for six Reynolds numbers and $\frac{b}{a} = 0.046$.

It is obvious that the first non-dimensional group which includes the factor '$\sin\theta$' accounts for the lateral spreading geometrically, thus making a comparison with the two-dimensional case possible. The distribution has a plateau region where the momentum is conserved approximately as shown earlier in Fig. 18. At about 90° the pressure rises and the adverse pressure gradient is maximum at 120°. This causes the flow to separate at about 155° where the pressure is higher than atmospheric due to the enclosed recirculating region at the back of the sphere. In this way the flow differs from the two-dimensional case, where the pressure at separation is sensibly that of the surroundings.

In these two figures it can be seen that the surface pressure is a function of Reynolds number in addition to being a function of "θ" as was predicted by dimensional analysis. However, beyond a certain limiting value of Re, the data collapse on a single line, thus exhibiting the independence of that number. This limiting value is about 4×10^4 * and thus similar to the two-dimensional case (Newman, 1961). Other measurements (e.g. velocity) were performed at this Re. No doubt this value depends slightly on boundary layer development within the slot, but because of the large contraction ratio this thickness was very small at the exit (see Fig. 5).

---

* This value may slightly change for other nozzle configurations.

Position of Separation

The angular position of separation, θ_{sep}, is shown as a function of Reynolds number in Fig. 21. As mentioned earlier, for low Re the velocity at the back of the sphere is very small, so that all the techniques which were used to detect separation, failed to respond within an acceptable accuracy. Therefore the results are shown only for high Re ($> 3 \times 10^4$). It is seen that the separation point is at about $155° \pm 3°$, the accuracy and the independence with Re being in qualitative agreement with the corresponding observation for the two-dimensional case.

4.3.2 Wake Measurements

Mean Velocity and Longitudinal Turbulence Profiles

Fig. 22 shows the non-dimensional mean velocity $\frac{U}{U_m}$ for various $\frac{Y}{Y_{m/2}}$, where U_m is the mean velocity at the centre-line of the jet. It is obvious that the mean velocity attains similarity beyond three sphere diameters as if the jet emanating from the orifice has not been disturbed by the presence of the sphere. Also shown in this figure is the non-dimensional velocity profile obtained by Johannesen (1962) for a free round jet; the agreement is fairly good.

The longitudinal turbulence intensities $\frac{\sqrt{\overline{u^2}}}{U_m}$ are shown in Fig. 23 and are compared with the results obtained by Corrsin (1949) for a free round jet. Two interesting aspects may be noted in this figure; the first is that the turbulence is an indicator of the upstream history associated with the presence of the sphere; this did not disappear even after seven sphere diameters which was the range of investigation. The second feature is that the percentage turbulence in the present case is less than that in a free round jet. The explanation for this probably lies in the suppression of the turbulence within the wall jet of the sphere.

Growth of the Free Jet

The growth of the free jet was found to be 0.0825 compared to the value 0.082 - 0.092 for that of a free round jet obtained by Hinze et al. (1949) and Wygnanski (1968). This is shown in Fig. 24, where the growth is plotted for different gap widths. It is interesting to note in that figure the location of the hypothetical origin and its change with the gap width for which a cross-plot is shown in Fig. 25.

This implies that the jet is much wider than a free round jet indicating that flows of this sort can be used in practice to reduce both the mean and the fluctuating energy in jets.

4.4 Comparison with Theory for the Two-dimensional Case

Figures 26 and 27 show the results obtained from the 'Higher Order' analysis (Eqs. 2-19 and 2-20), as compared with the experimental results of Fekete (1963) and the other theories. The constants in Eqs. 2-19 and 2-20 were evaluated from the experimental results of Fekete at $\theta = 40°$ and $\frac{b'}{a'} = 0.0229$. It is seen that the prediction of the velocity decay is fairly good except for the downstream part. Note that there is considerable scatter in the experimental results, although this is mainly for moderate values of "θ".

The surface pressure distribution is in a very good agreement except again for the downstream part, being consistent with the velocity decay.

This shows that despite the assumption of a top hat profile, the inclusion of the inertia terms has been mainly responsible for the improved prediction (Newman, 1961).

4.5 Comparison with theory for the Axi-Symmetric Case

The experimental results for the maximum velocity decay and the surface pressure are now compared with the prediction obtained by applying 'Newman's First-Order' analysis (Eqs. 2-10 and 2-13) and the 'Higher Order' analysis (Eqs. 2-14 and 2-17). The necessary initial conditions for the Runge-Kutta technique and the constants in both analyses were evaluated at the station $\theta = 40°$. The latter was chosen on the basis that the flow was not developed before this position, as judged from the scatter in the surface pressure distribution and the growth of the jet. The comparison is made only for the case of the universal flow, $\frac{b}{a} = 0.046$.

Maximum Velocity Decay

Fig. 28 shows the decay of the maximum velocity coefficient as predicted by the two analyses. It should be remembered that the difference between the two equations (2-10) and (2-14) is that the former is written to the first order in $\frac{y_{m/2}}{a}$, while the latter has no approximation in it, except that inherent in the linear assumption for the pressure change across the flow.

Obviously, Eq. (2-14) is an improvement over Eq. (2-10) and it predicts the experimental results fairly well with an accuracy better than 10%.

Surface Pressure Distribution

As the main aim of the present theoretical work was to identify the contribution of the various terms in the y-momentum equation, the integral of this equation, Eq. (2-17), was computed for each term separately.

In Fig. 29, curve (1) represents the first order analysis, Eq. (2-13), which does not include any inertia or stress terms. Curve (2) is obtained when the inertia terms are included in the equation. This exhibits a more realistic trend than the previous one, although the predicted pressure is still larger than the actual surface pressure. The contribution of the shear stress and normal stresses is small, as can be seen from curves (3) and (4) which are slightly higher than curve (2). In order to demonstrate that the 'top-hat' profile is not the cause of the discrepancy between the aforementioned curves and the actual one, values of $\int_0^\infty \frac{\rho U^2}{a+y} dy$, for various angular positions, have been computed numerically for the measured profiles and the results, curve (5), are found to lie close to the 'First Order' theory. This was also found by Newman (1961) for the two-dimensional case.

It may first appear that the prediction of the surface pressure by the 'Higher Order' analysis in the axi-symmetric case is inconsistent with that in the two-dimensional case (see Fig. 27) where the theoretical curve is closer to the experimental one; however, this is not the case.

Let us reconsider the integrated momentum equations. In both the two-dimensional and axi-symmetric cases the surface pressure is predicted by means of the integrated y-momentum equation which involves terms in $\frac{dU_1}{dx}$ and $\frac{d^2U_1}{dx^2}$. These inertia terms are quite dominant as has been shown. Therefore, in order to evaluate them accurately, the velocity must be predicted with a very high degree of accuracy, for the accuracy of its derivatives to be acceptable, although accuracy in $\frac{d^2U_1}{dx^2}$ is less important. This cannot be achieved unless the x-momentum equation is computed using a more accurate assumption for the pressure variation across the flow than has been used. It was seen in Fig. (26), however, that in the two-dimensional case the actual slope of the velocity curve is nearly constant (theory also gives that slope accurately); hence the second derivative of the velocity is negligible and the approximation for the pressure variation across the flow is quite valid. Consequently, the predicted surface pressure is expected to be in good agreement (Fig. 27).

For the axi-symmetric case, however, it is obvious from Fig. 28 that, although the velocity is predicted more or less accurately, the slope at the starting point is in tremendous error. In order to be sure that this is in fact the reason for the failure of Eq. (2-17) to predict the surface pressure, the value of $\frac{dU_1}{dx}$ at the starting point, estimated from the measured velocities, was inserted in the equation and, surprisingly enough, the resulting surface pressure was higher than the experimental one by only 3%, i.e. the value of Eq. (2-17) with the correct value of $\frac{dU_1}{dx}$ is 0.59 at $\theta = 40°$.

To summarize the problem, if an accurate prediction of the surface pressure is sought, the term $\frac{dp}{dx}$ in the streamwise momentum equation should probably be evaluated by means of the complete radial momentum equation, so that the velocity and its derivatives are estimated accurately and consequently the surface pressure is well predicted.

4.6 Momentum Balance

In order to check the momentum balance, two control volumes were chosen as shown in the opposite figure.

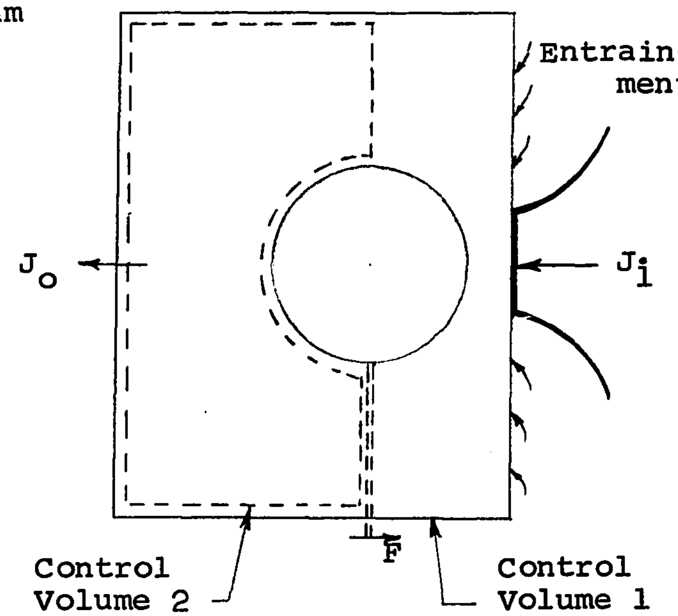

For the control volume 1 , neglecting the skin friction over the sphere and the entrainment, we have

$$- F = J_o - J_i \qquad \text{(i)}$$

where

F is the force exerted by the sphere, calculated by integrating the surface pressure (neglecting skin friction)

J_o is the momentum in the fully developed wake, estimated by integrating the mean velocity profile there at different stations. It was found to be nearly conserved downstream within the accuracy of the measurements for $\frac{X}{2a} > 3$

J_i is the momentum out of the nozzle and equals the following surface integral.

$$J_i = \int_A (p+\rho U^2)\, dA = \int_A p_o+\tfrac{1}{2}\rho(U^2-V^2) \quad dA = p_oA + \int_A \tfrac{1}{2}\rho(U^2-V^2)\, dA$$

where

p_o is the stagnation pressure in the plenum chamber (neglecting slot boundary layers which were thin, Fig. 5)

A is the area of the nozzle exit

p is the local static pressure at the nozzle exit

U is the component of the mean velocity at the nozzle exit and is parallel to the axis of the nozzle

V is the component of the mean velocity at the nozzle exit and is perpendicular to the axis of the nozzle

The integral, $\int_A \frac{1}{2}\rho(U^2-V^2)\,dA$, was assumed to be small and was neglected. It was impossible to check this, however, with the experimental techniques used.

Equation (i) was checked for three different gap widths and the unbalance, $\left[(J_o+F) - J_i\right]$, was found not to exceed 10% of J_o as shown in the following table. This unbalance is due in part to the neglect of the aforementioned integral which would increase the value of J_i ($U>V$ over most of the nozzle exit). Neglecting the skin friction over the sphere would increase the value of the force "F", but this increase would be very small (see section 4.5).

$\frac{b}{a}$	Re	M/J_i	J_o/J_i	F/J_i	$\left[J_o-(J_i-F)\right]J_o$
0.0116	5.6×10^4	0.331	0.322	0.707	9.75%
0.046	5.8×10^4	0.763	0.55	0.50	9.02%
0.117	5.9×10^4	1.178	0.916	0.165	8.64%

In order to check the momentum 'J_o' in the wake, another control volume (2) was chosen. The momentum through its upstream face was computed from the measured velocity profile there, and the surface pressure at the back of the sphere. This momentum was found to be 1.42 at $\frac{b}{a} = 0.046$, that is, the unbalance does not exceed 6.8% of J_o (if skin friction is neglected).

The existence of any thrust augmentation was checked by comparing "J_o" with the momentum "M" coming out of the nozzle with the sphere removed, for the same energy input to blower. This momentum "M" is included in the above table. It is seen that no thrust augmentation can be obtained with the present configuration, even though the pressure over much of the sphere is below atmospheric. With another nozzle configuration the force on the sphere may be <u>towards</u> the nozzle as shown by the simple demonstration in Fig. 1.

5. Conclusions

A universal flow, independent of inlet conditions, was set up. The ratio of the gap width to the sphere radius for this flow was found to be 0.046 and the associated growth of jet thickness at the front of the sphere agreed with that of the plane radial wall jet.

It was confirmed that the velocity profiles are similar over a large portion of the sphere as is usual for such flows. They show good agreement with Glauert's theoretical prediction, with $\frac{y_m}{y_{m/2}}$ chosen to be 0.12, for plane wall jets. The growth is found to be nearly the same as that of the two-dimensional wall jet over a circular cylinder implying that the stretching of the eddies increases the entrainment sufficiently to compensate for the lateral expansion at least up to $\theta = 90°$. The longitudinal turbulence intensities are in qualitative agreement with those for the two-dimensional and for plane radial wall jets. The flow separates at $\theta = 155°$ forming a bubble at the back of the sphere and an axi-symmetric jet forms downstream. Hot wire measurements in the wake showed that the mean velocity profile becomes similar after three sphere diameters downstream of the nozzle exit, whereas the longitudinal turbulence does not attain similarity up to seven sphere diameters, which was the range of investigation. The theoretical analyses, namely the 'First Order' and the 'Higher Order' have brought out the following points which relate to both the two-dimensional and axi-symmetric cases:

1. The 'top-hat' profile, suggested by Newman (1961), is very adequate for an integral technique and is not responsible for any gross discrepancy in predicting the velocity and surface pressure.

2. The most important second order terms in the radial momentum equation are the inertia terms as was presumed by Newman; while the turbulence terms account for very little.

3. In order to obtain a reasonable prediction for the surface pressure distribution, the inertia terms must be estimated fairly accurately. This cannot be achieved unless the pressure term in the x-momentum equation is calculated using the full y-momentum equation which is analytically rather tedious. However, if the slope of the velocity decay is nearly constant, as in the two-dimensional case, a simple approximation may be made for this term and reasonable prediction is obtained.

The investigation could be usefully extended by:

1. Performing comprehensive measurements of turbulence intensities over the sphere, to get more insight in the stretching of the eddies. This would be also valuable for estimating more accurately the contribution of the stress terms in the momentum equations.

2. Reapplying the higher order analysis with the correct value of $\frac{dp}{dx}$ in the streamwise momentum equation.

3. Replacing the term $\frac{dp}{dx}$ by its exact value in the full integral technique, thus eliminating the instability (section 2.5) of the numerical solution.

4. In the other direction, by studying axi-symmetric flows over other shapes of practical as well as theoretical interest.

5. Making a more detailed investigation of the flow associated with the demonstration in Fig. 1, to determine if this could produce any thrust augmentation.

References

Bakke, P.	An Experimental Investigation of a Wall Jet, J. Fluid Mech., Vol. 2, p. 467, 1957.
Begg, R.D.	A Note on the Reattachment of Two-Dimensional Compressible Jets to Planes, J. Royal Aero. Soc., Vol. 71, p. 656, 1967.
Blasius, H.	Forshungsarbeiten des Ver. deutsch Ing., No. 131, 1913.
Bradshaw, P. and Gee, M.T.	Turbulent Wall Jets with and without an External Stream, ARC 22, 008, FM 2971, 1960.
Bradshaw, P. and Love, E.M.	The Normal Impingement of a Circular Air Jet on a Flat Plate, ARC R. and M. 3205, 1961.
Corrsin, S. and Uberoi, M.S.	NACA TN 1865, 1949.
Eskinazi, S. and Kruka, V.	Mixing of a Turbulent Wall-Jet into a Free Stream, Proc. of ASCE 88, No. FM2, 125, 1962.
Fekete, G.I.	Coanda Flow of a Two-Dimensional Wall Jet on the Outside of a Circular Cylinder, McGill University, Dept. of Mech. Eng., Report 63-11, 1963.
Förthmann	Uber turbulente Strahlausbreitung, Ing.-Arch., 5, 42. N.A.C.A., TM 789, 1936.
Gartshore, I.S. and Hawaleshka, O.	The Design of a Two-Dimensional Blowing Slot and its Application to a Turbulent Wall Jet in Still Air, McGill University, Dept. of Mech. Eng., TN 64-5, 1964.
Gartshore, I.S. and Newman, B.G.	The Turbulent Wall Jet in an Arbitrary Pressure Gradient, Aero. Quarterly, Vol. 20, p. 25, 1969.

Giles, J.A., Hays, A.P. and Sawyer, R.A. — Turbulent Wall Jets on Logarithmic Spiral Surfaces, Aero. Quart., Vol. 17, p. 201, 1966.

Glauert, M.B. — The Wall Jet, J. Fluid Mech., Vol. 1, p. 625, 1956.

Goldstein, S. — Modern Developments in Fluid Dynamics, Vol. II, Oxford, 1938.

Görtler, H. — Berechnung von Aufgaben der freien Turbulenz auf Grund eines neuen Haherungsanstzes, ZAMM 22, 244, 1942.

Guitton, D. — Two-Dimensional Turbulent Wall Jet over Curved Surfaces, McGill University Dept. of Mech. Eng., Report 64-7, 1964 (and Addendum, TN 67-1)

Guitton, D. — The Two-Dimensional Turbulent Wall Jet over a Convex Logarithmic Spiral (R=x), Von Karman Institute, Rhode Ste. Genese, Project Report 65-128, June 1965.

Guitton, D. — Correction of Hot Wire Data for High Intensity Turbulence, Longitudinal Cooling and Probe Interference, McGill University, Dept. of Mech. Eng., Report 68-6, 1968.

Guitton, D. — A Transient Technique for Measuring Skin Friction Using a Flush-Mounted Heated Film and its Application to a Wall Jet in Still Air, McGill University Dept. of Mech. Eng., Report 69-9, 1969.

Guitton, D. — Unpublished Results (1970).

Hinze, J.O. and Van der Hegge Zijnen — Applied Science Res., 1A, 435, 1949

Johannessen, N.H. — Further Results on the Mixing of Free Axially-Symmetrical Jets of Mach Number 1.4, ARC R. and M. 3292, 1962.

Jordinson, R. — A Method based on the Use of the Schwarz-Christoffel Transformation for Incompressible Inviscid Flow, A.C. Eng., Vol. 33, No. 392, p. 294, 1961.

Lawrence, R.L. — Velocity Profiles from Compressible Wall Jets, AIAA J. 2, 574, 1964.

Mathieu, J. and Tailland, A. — Jet Pariétal, Journal de Mécanique, Vol. 6, No. 1, p. 103, 1967.

Myers, G.E., Schauer, J.J., and Eustis, P.H. — The Plane Turbulent Wall Jet, Part 1 Jet Development and Friction Factor, Stanford University, Dept. of Mech. Eng., Stanford, California, NSF 69705 Tech. Rep. 1, 1961.

Myers, G.E., Schauer, J.J. and Eustis, R.N. — The Plane Turbulent Wall Jet, Jet Development and Friction Factor, Trans. ASME, J. of Basic Eng., Vol. 85(2), p. 47, 1963.

Nakaguchi, H. — Jet along a Curved Wall, University of Tokyo, Dept. of Aeronautics, Research Memo 4, 1961.

Newman, B.G. — The Deflexion of Plane Jets by Adjacent Boundaries - Coanda Effect, Boundary Layer and Flow Control, Vol. 1, p. 232, Pergamon Press, 1961.

Newman, B.G. — Turbulent Jets and Wakes in a Pressure Gradient, Elsevier, Fluid Mechanics of Internal Flow, Ed. G. Sovran, p. 170, 1967.

Newman, B.G. — The Prediction of Turbulent Jets and Wall Jets, W. Rupert Turnbull Lecture, Canadian Aeronautics and Space Journal, Vol. 15, No. 8, 1969.

Patel, R.P. — Self-Preserving, Two-Dimensional Turbulent Jets and Wall Jets in a Moving Stream, M.Eng. Thesis, Mech. Eng. Dept., McGill University, 1962.

Patel, R.P. — The Effects of Wind Tunnel Screens and Honeycombs on the Spanwise Variation of Skin Friction in "Two-Dimensional Turbulent Boundary Layers." Proc. of the 2nd Australasian Conference on Hydraulics and Fluid Mechanics, p. B65, 1965.

Rouse, H. — Advanced Mechanics of Fluids, John Wiley and Sons, 1959.

Sawyer, R.A. — Two-Dimensional Turbulent Jets with Adjacent Boundaries, Cambridge University, Ph.D. Thesis, 1962.

Schwarz, W.H. and Cosart, W.P. — The Two-Dimensional Turbulent Wall Jet, J. Fluid Mech., Vol. 10, Part 4, 1961.

Sigalla, A. — Experimental Data on Turbulent Wall-Jets, Aircraft Engineering, May 1958.

Starr, J.B. and Sparrow, E.M. — Experiments on a Turbulent Cylindrical Wall-Jet, J. Fluid Mech., Vol. 29, p. 495, 1967.

Townsend, A.A. — The Structure of Turbulent Shear Flow, Cambridge University Press, 1956.

Tsuei, Y.G. — Axi-Symmetric Boundary-Layer of a Jet Impinging on a Smooth Plate, Colorado State University, Ph.D. Thesis, 1963.

Wille, R. and Fernholz, H. — Report on the First European Colloquium on the Coanda Effect, J. Fluid Mech., Vol. 23, p. 801, 1965.

Wygnanski, I. and Fiedler, H.E. — Some Measurements in the Self-Preserving Jet, Boeing Scientific Research Labs., Document D1-82-0712, 1968.

Wygnanski, I. and Champagne, F.H. — The Laminar Wall-Jet over a Curved Surface, J. Fluid Mech., Vol. 31, Part 3, p. 459, 1968.

Appendix I

Description of Apparatus

The experimental arrangement, shown schematically in Fig. 2-1, consists of an 8.5 in. diameter bowling ball supported on the end of a $\frac{1}{2}$ in. diameter steel pipe, which was held in bearings on perforated plates in the air settling chamber.

The air was supplied from a centrifugal blower powered by a 10 H.P., constant speed, 3 phase induction motor. The flow rate was varied by a throttle valve installed at the outlet of the blower. Four streamlined wooden spacers were later inserted between the valve and the blower outlet for bleeding off excess air, thus eliminating any surge problem. This arrangement permitted variable jet speed control from 0 to 320 fps.

The perforated plate (3) was placed at the central section of the expansion in order to reduce the adverse pressure gradient and prevent separation of the flow. The 16:1 contraction chamber was made from a 10 in. length of 8 in. diameter plexiglas round bar and it was based on the theoretical analysis developed by Jordinson (1961) for large contraction ratios. The outside of this contraction chamber was shaped so as not to inhibit entrainment and it was terminated by a

2 in. diameter nozzle.

The positions of the perforated plate (1) and (2), of $\frac{1}{16}$ in. thickness and 33% open area, could be adjusted to compensate for slight bending of the pipe due to the weight of the sphere (see Fig. 2-2). The pipe could thereby be located accurately in the centre of the nozzle and when this was done axial symmetry of the flow was obtained (see section 3.1.2). A locking nut was provided at the upstream perforated plate to prevent longitudinal motion of the pipe.

Two deep-cell honeycombs, of 0.5 in. thickness and $\frac{1}{8}$ in. cell size, were installed one at the outlet of the expansion to remove swirl in the air flow originating from the blower, and the second at the inlet of the contraction chamber to minimize divergence of the flow after passing through the perforated plates.

The forty surface pressure tappings, of 0.015 in. diameter, on the sphere whose angular positions are shown in Fig. 2-3, were connected to four rows of pressure tappings on the surface of the plexiglas tube, through tygon tubings threaded carefully inside the central pipe. The whole apparatus was fixed to a rigid table.

The traversing gear was mounted on a 2.5 in. diameter steel pipe welded to a square steel plate 24 x 24 x 0.5 in. In order to eliminate any vibrations in the pipe, its top was tied to the plate with four guy-wires adjusted with turn buckles. The steel plate had three wooden pads, resting on smooth sheets of plywood screwed to the floor of the laboratory, to ensure the stability of the traversing gear. The latter, incorporating a slider and double ended dial gauge, permitted accurate radial location of the measuring probe to 0.001 in. (see Fig. 4).

The static pressure in the plenum chamber was measured downstream of the perforated plate(1).This pressure was close to the total pressure of the core flow emerging from the nozzle (within 0.4% of the dynamic pressure). The stagnation temperature was measured by means of the sensing element of a telethermometer inserted through the nozzle. Pitot pressure, referenced to the surrounding atmosphere, was measured to an estimated accuracy of 1% by vertical and inclined manometers.

The hot wire measurements were made using a DISA (55A01) constant temperature anemometer, a DISA (55D10) linearizer, two RMS-Meter (DISA 55D35 and Hewlett-Packard 3400A), a Hewlett-Packard (2212A) voltage to frequency converter, a Hewlett-Packard (5216A) digital counter, a Hewlett-Packard Oscillator for long time integration and a Hewlett-Packard (562A) printer. This electonic circuit is shown in Fig. 3.

Appendix II

Formulation of the Equations used in the Full Integral Technique

a) Velocity Profiles Assumed

Outer Layer: $$\frac{U}{U_m} = \mathrm{Sech}^2\eta$$

where $$\eta = 0.88 \; \frac{y - y_m}{L}$$

$$L = y_{\frac{m}{2}} - y_m$$

Inner Layer: $$\frac{U}{U_m} = \left(\frac{y}{y_m}\right)^{\frac{1}{n}}$$

where $n = 11$

b) Equations

The first equation is obtained by integrating the x-momentum equation (2-6) from 0 to y_m as follows:

$$\int_0^{y_m} (a+y)^2 \frac{\partial}{\partial x}\left(U^2 \sin\theta\right) dy + \left[\frac{(a+y)^3}{a} \, UV \sin\theta\right]_0^{y_m} = -\int_0^{y_m} (a+y)^2 \sin\theta \frac{\partial}{\partial x}\left(\frac{p}{\rho} + \overline{v^2}\right) dy$$

$$+ \left[\frac{(a+y)^3}{a} \frac{\tau}{\rho} \sin\theta\right]_0^{y_m} \qquad \text{(II-1)}$$

Assuming a linear variation for the static pressure plus normal turbulence intensity across the flow, i.e.

$$\frac{p}{\rho} + \overline{v^2} = \frac{p_s}{\rho}\left(1 - \frac{y}{E}\right)$$

where "E" is considered to be proportional to "$y_{m/2}$" with a constant of proportionality of 2, representing approximately the average point of the boundary of vortical flow (Guitton, 1964). The total pressure at this distance "E" from the surface is close to that of the surroundings.

After substitution of the velocity profile (inner layer), Eq. (II-1) becomes

$$C_1 \frac{dU_m}{dx} + C_2 \frac{dy_m}{dx} = C_3 \tag{II-2}$$

where

$$C_1 = \frac{121}{13\times 12} U_m y_m$$

$$C_2 = \frac{13}{12} U_m^2 + \frac{y_m^2}{2E(L+y_m)} \frac{p_s}{\rho}$$

$$C_3 = \frac{11}{12\times 13} U_m^2 \frac{y_m}{a} \cot\theta + \left(\frac{y_m^2}{2E} - y_m\right) \frac{d(p_s/\rho)}{dx} - \frac{y_m^2}{2E(L+y_m)} p_s \frac{dL}{dx} + \frac{\tau_m - \tau_w}{\rho}$$

Following Gartshore and Newman (1969), the surface skin friction is represented by

$$\frac{\tau_w}{\frac{1}{2}\rho U_m^2} = 0.0257 \left(\frac{U_m y_m}{\nu}\right)^{-\frac{1}{6}}$$

The value of τ_m is obtained from the measurements of shear stress by Guitton (1970) in wall jets over logarithmic spirals. He found that τ_m varies from " $-\tau_w$" to " $-4\tau_w$" in the region where the pressure coefficient is constant (plateau region). As a preliminary attempt a constant value of " $-2\tau_w$" was chosen. (τ_m is the shear stress at the maximum velocity point.)

Similarly, the second equation is obtained by performing the integration in Eq. (II-1) from y_m to ∞, and substituting the velocity profile (outer layer). This equation reads

$$C4 \frac{dU_m}{dx} + C5 \frac{dy_m}{dx} = C6 \tag{II-3}$$

where

$$C4 = 2 U_m a^2 \int_{y_m}^{\infty} \left(1 + \frac{y}{a}\right)^2 \operatorname{Sech}^2 \eta \, dy + \frac{11}{12} (a + y_m)^3 U_m \frac{y_m}{a}$$

$$C5 = \frac{3.52}{L} U_m^2 a^2 \int_{y_m}^{\infty} \left(1 + \frac{y}{a}\right)^2 \operatorname{Sech}^2 \eta \tanh \eta \, dy - \frac{U_m^2}{12a} (a + y_m)^3$$
$$+ \frac{p_s}{\rho} \frac{1}{E(L + y_m)} \left[\frac{(a+E)^3 E}{3} - \frac{(a+y_m)^3}{3} y_m - \frac{(a+E)^4}{12} + \frac{(a+y_m)^4}{12} \right]$$

$$C6 = - U_m^2 \, a \cot\theta \int_{y_m}^{\infty} \left(1 + \frac{y}{a}\right)^2 \operatorname{sech}^4 \eta \, dy - \frac{4}{0.88} U_m^2 a^2 \frac{dL}{dx}$$
$$- \frac{11}{12} \frac{(a+y_m)^3}{a^2} y_m U_m^2 \cot\theta - \frac{(a+y_m)^3}{a} \frac{T_m}{\rho} - \frac{1}{3} \frac{d(p_s/\rho)}{dx} \left[(a+E)^3 - (a+y_m \right.$$
$$+ \left[\frac{1}{E} \frac{d(p_s/\rho)}{dx} - \frac{p_s}{\rho} \frac{1}{E(L+y_m)} \frac{dL}{dx} \right] \left[\frac{(a+E)^3 E}{3} - \frac{(a+y_m)^3}{3} y_m - \frac{(a+E)^4}{12} + \frac{(a+y_m)}{12} \right.$$

The above integrals and those following are computed numerically using Simpson's Rule.

Now, the two equations (II-2) and (II-3) have two unknowns namely "U_m" and "y_m" and are solved simultaneously using a 4th order Runge-Kutta technique. "L" and $\frac{dL}{dx}$ in those equations are evaluated from a polynomial which expresses the rate of growth as found experimentally, p_s is obtained from the third equation which will be formulated later and $\frac{dp_s}{dx}$ is found by an iteration procedure, at each step of the numerical technique, once p_s is known.

The third equation, form which p_s is evaluated is obtained by integrating the y-momentum equation (2-4) from 0 to ∞ in two steps: from 0 to y_m then from y_m to ∞, as follows

$$\int_0^{y_m} \frac{a}{a+y} U \frac{\partial V}{\partial x}\, dy + \int_{y_m}^{\infty} \frac{a}{a+y} U \frac{\partial V}{\partial x}\, dy - \int_0^{y_m} \frac{U^2}{a+y}\, dy - \int_{y_m}^{\infty} \frac{U^2}{a+y}\, dy$$

$$= -\frac{(p_\infty - p_s)}{\rho} + \int_0^{y_m} \frac{a}{a+y} \frac{\partial}{\partial x}\left(\frac{\tau}{\rho}\right) dy + \int_{y_m}^{\infty} \frac{a}{a+y} \frac{\partial}{\partial x}\left(\frac{\tau}{\rho}\right) dy + (\cot\theta - 1)\int_0^{y_m} \frac{\tau/\rho}{a+y}\, dy$$

$$+ (\cot\theta - 1)\int_{y_m}^{\infty} \frac{\tau/\rho}{a+y}\, dy \qquad \text{(II-4)}$$

where the term $(\overline{u^2}-\overline{v^2})$ to be equal to $\overline{uv}$ (Guitton, 1970).

The value of each integral in Eq. (II-4) is calculated separately as follows

$$\text{i} - \int_0^{y_m} \frac{a}{a+y} U \frac{\partial V}{\partial x}\, dy = \frac{-121}{288} U_m \frac{y_m^2}{a} \cot\theta \frac{dU_m}{dx} + \frac{121}{288} U_m^2 \frac{y_m^2}{a} \operatorname{Cosec}^2\theta + \frac{11}{288} U_m^2 \frac{y_m}{a} \cot\theta \frac{dy_m}{dx}$$

noting that the velocity "V" is obtained by integrating the continuity equation (2-5).

$$\text{ii} - \int_0^{y_m} \frac{u^2}{a+y}\, dy = \frac{11}{13a} U_m^2 y_m$$

$$\text{iii} - \int_{y_m}^{\infty} \frac{u^2}{a+y}\, dy = \frac{U_m^2}{a} \frac{L}{0.88} \int_0^{\infty} \frac{\operatorname{sech}^4\eta}{1+\frac{y}{a}}\, d\eta$$

$$\text{iv} - \int_0^{y_m} \frac{a}{a+y} \frac{\partial}{\partial x}\left(\frac{\tau}{\rho}\right) dy = U_m \frac{d\nu_T}{dx} + \nu_T \frac{dU_m}{dx} - \frac{\nu_T}{11} \frac{U_m}{y_m} \frac{dy_m}{dx}$$

where $\frac{\tau}{\rho}$ is assumed to be equal to $\nu_T \frac{\partial U}{\partial y}$

and ν_T is the eddy viscosity which is a function of "x" only and equals $\frac{U_m L}{33}$(Newman, 1967). One could change ν_T to allow for curvature, but this has not been adopted in the present analysis.

$$\text{v} - \int_{y_m}^{\infty} \frac{a}{a+y} \frac{\partial}{\partial x}\left(\frac{\tau}{\rho}\right) dy = -1.76\left(\frac{\nu_T}{L}\frac{dU_m}{dx} + \frac{U_m}{L}\frac{d\nu_T}{dx} - \frac{U_m}{L^2}\nu_T\frac{dL}{dx}\right)\int_{y_m}^{\infty} \frac{a}{a+y} \operatorname{Sech}^2\eta \tanh\eta$$

$$+ 1.76\,\frac{U_m \nu_T}{L}\,\frac{0.88}{L^2}\,\frac{dL}{dx}\int_{y_m}^{\infty} \frac{a}{a+y}\, y\left(\operatorname{Sech}^2\eta - 3\tanh^2\eta \operatorname{Sech}^2\eta\right)$$

$$+ 1.76\,\frac{U_m \nu_T}{L}\,\frac{0.88}{L}\left(\frac{dy_m}{dx} - \frac{y_m}{L}\frac{dL}{dx}\right)\int_{y_m}^{\infty}\left(\operatorname{Sech}^2\eta - 3\tanh^2\eta \operatorname{Sech}^2\eta\right)\frac{a}{a+y}$$

$$\text{vi} - (\cot\theta - 1)\int_0^{y_m} \frac{\tau/\rho}{a+y}\, dy = (\cot\theta - 1)\,\frac{\nu_T U_m}{a}$$

$$\text{vii} - (\cot\theta - 1)\int_{y_m}^{\infty} \frac{\tau/\rho}{a+y}\, dy = -1.76\,(\cot\theta - 1)\,\frac{U_m}{L}\nu_T \int_{y_m} \frac{\operatorname{Sech}^2\eta \tanh\eta}{a+y}\, dy$$

$$\text{viii}\quad -\int_{y_m}^{\infty}\frac{a}{a+y}\,U\frac{\partial V}{\partial x}\,dy = F1\int_{y_m}^{\infty}\frac{a^2}{(a+y)^3}\,\operatorname{sech}\eta\,dy + F2\int_{y_m}^{\infty}\frac{a^2}{(a+y)^3}\,\operatorname{Sech}^2\eta\,\tanh\eta\,dy$$

$$+ F3\int_{y_m}^{\infty}\frac{a^2}{(a+y)^2}\,\operatorname{Sech}^2\eta\,\tanh\eta\,dy + F4\int_{y_m}^{\infty}\frac{a^2}{(a+y)^3}\,y\,\operatorname{Sech}^2\eta\,\tanh\eta\,c$$

$$+ F5\int_{y_m}^{\infty}\frac{a^2}{(a+y)^3}\,\operatorname{Sech}^2\eta\,\log\operatorname{Cosh}\eta\,dy + F6\int_{y_m}^{\infty}\frac{a^2}{(a+y)^3}\,\operatorname{Sech}^4\eta\,dy$$

$$+ F7\int_{y_m}^{\infty}\frac{a^2}{(a+y)^2}\,y\,\operatorname{Sech}^4\eta\,dy + F8\int_{y_m}^{\infty}\frac{a^2}{(a+y)^2}\,\operatorname{Sech}^4\eta\,dy$$

$$+ F9\int_{y_m}^{\infty}\frac{a^2}{(a+y)^3}\,y\,\operatorname{Sech}^4\eta\,dy + F10\int_{y_m}^{\infty}\frac{a^2}{(a+y)^3}\,y^2\operatorname{Sech}^4\eta\,dy$$

$$+ F11\int_{y_m}^{\infty}\frac{a^2}{(a+y)^2}\,\operatorname{Sech}^4\eta\,\tanh\eta\,dy + F12\int_{y_m}^{\infty}\frac{a^2}{(a+y)^2}\,y\,\operatorname{Sech}^4\eta\,\tanh\eta$$

$$+ F13\int_{y_m}^{\infty}\frac{a^2}{(a+y)^2}\,y^2\,\operatorname{Sech}^4\eta\,\tanh\eta\,dy$$

where

$$F1 = -\frac{11}{12}U_m y_m\frac{dU_m}{dx}\cot\theta - \frac{11}{12}U_m^2\frac{dy_m}{dx}\cot\theta + \frac{11}{12a}U_m^2 y_m\operatorname{Cosec}^2\theta - \frac{11}{12}a\,U_m y_m\frac{d}{c}$$

$$-U_m\frac{dU_m}{dx}\frac{dy_m}{dx}\left(\frac{22}{12}a + y_m\right) - U_m^2\frac{d^2y_m}{dx^2}\left(\frac{11}{12}a + y_m\right) - U_m^2\left(\frac{dy_m}{dx}\right)^2$$

$$F2 = -\frac{U_m}{0.88a}\cot\theta\left(L U_m\frac{dy_m}{dx} - y_m U_m\frac{dL}{dx}\right) + \frac{2}{0.88}U_m y_m\frac{dU_m}{dx}\frac{dL}{dx} + \frac{U_m^2}{0.88}\frac{d^2L}{dx^2}y_m$$

$$-2U_m\frac{L}{0.88}\frac{dU_m}{dx}\frac{dy_m}{dx} - 2\frac{U_m^2}{0.88}\frac{dL}{dx}\frac{dy_m}{dx} + 2\frac{U_m^2}{0.88L}\left(\frac{dL}{dx}\right)^2 y_m$$

$$-U_m^2\frac{L}{0.88}\frac{d^2y_m}{dx^2}$$

$$F3 = -\frac{U_m}{0.88a}\operatorname{Cot}\theta\left(L\frac{dU_m}{dx} + U_m\frac{dL}{dx}\right) + \frac{L}{0.88a^2}U_m^2\operatorname{Cosec}^2\theta - 2\frac{U_m}{0.88}\frac{dU_m}{dx}\frac{dL}{dx}$$

$$-\frac{U_m L}{0.88}\frac{d^2U_m}{dx^2} - \frac{U_m^2}{0.88}\frac{d^2L}{dx^2}$$

$$F_4 = -\frac{U_m^2}{0.88a}\cot\theta\frac{dL}{dx} - \frac{2U_m}{0.88}U_m\frac{dU_m}{dx}\frac{dL}{dx} - \frac{U_m^2}{0.88}\frac{d^2L}{dx^2} - \frac{2U_m^2}{0.88L}\left(\frac{dL}{dx}\right)^2$$

$$F_5 = \frac{1}{(0.88)^2}\left[-\left(\frac{L}{a}\right)^2 U_m^2 \operatorname{Cosec}^2\theta + \frac{U_m L}{a}\cot\theta\left(L\frac{dU_m}{dx} + 2U_m\frac{dL}{dx}\right) + 4LU_m\frac{dU_m}{dx}\right.$$

$$\left. + L^2 U_m\frac{d^2U_m}{dx^2} + 2U_m^2\left(\frac{dL}{dx}\right)^2 + 2U_m^2 L\frac{d^2L}{dx^2}\right]$$

$$F_6 = -2U_m^2\frac{dL}{dx}\frac{dy_m}{dx}\frac{y_m}{L} + \frac{U_m^2}{L^2}\left(\frac{dL}{dx}\right)^2 y_m^2 + U_m^2\left(\frac{dy_m}{dx}\right)^2$$

$$F_7 = \frac{U_m^2}{aL}\cot\theta\frac{dL}{dx} + 2\frac{U_m}{L}\frac{dU_m}{dx}\frac{dL}{dx} + \frac{U_m^2}{L}\frac{d^2L}{dx^2}$$

$$F_8 = \frac{U_m^2}{a}\cot\theta\left(\frac{dy_m}{dx} - \frac{y_m}{L}\frac{dL}{dx}\right) - 2\frac{y_m}{L}U_m\frac{dU_m}{dx}\frac{dL}{dx} + 2U_m\frac{dU_m}{dx}\frac{dy_m}{dx}$$

$$- U_m^2\frac{d^2L}{dx^2}\frac{y_m}{L} + U_m^2\frac{d^2y_m}{dx^2}$$

$$F_9 = 2\frac{U_m^2}{L}\frac{dL}{dx}\frac{dy_m}{dx} - 2\frac{U_m^2}{L^2}y_m\left(\frac{dL}{dx}\right)^2$$

$$F_{10} = \frac{U_m^2}{L^2}\left(\frac{dL}{dx}\right)^2$$

$$F_{11} = 1.76\frac{U_m^2}{L}\left[\left(\frac{dy_m}{dx}\right)^2 + \frac{y_m^2}{L^2}\left(\frac{dL}{dx}\right)^2 - 2\frac{y_m}{L}\frac{dL}{dx}\frac{dy_m}{dx}\right]$$

$$F_{12} = 3.52\frac{U_m^2}{L}\left[\frac{1}{L}\frac{dL}{dx}\frac{dy_m}{dx} - \frac{y_m}{L^2}\left(\frac{dL}{dx}\right)^2\right]$$

$$F_{13} = 1.76\frac{U_m^2}{L^3}\left(\frac{dL}{dx}\right)^2$$

SPHERE SUPPORTED BY A CIRCULAR JET

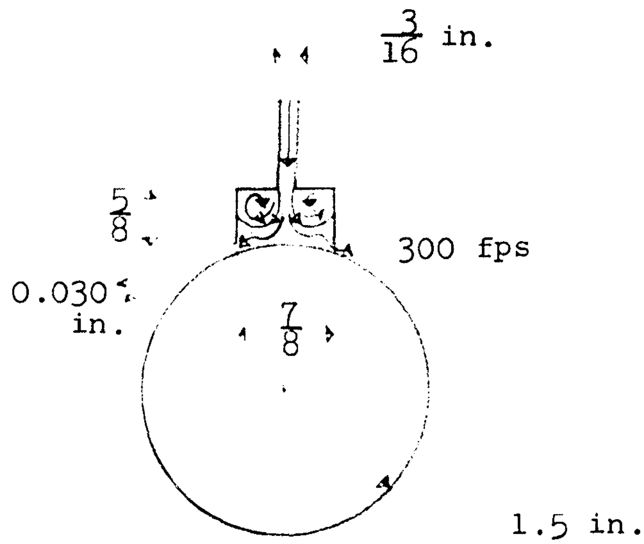

Scale: 1:2

SPHERE SUPPORTED BY A CIRCULAR JET

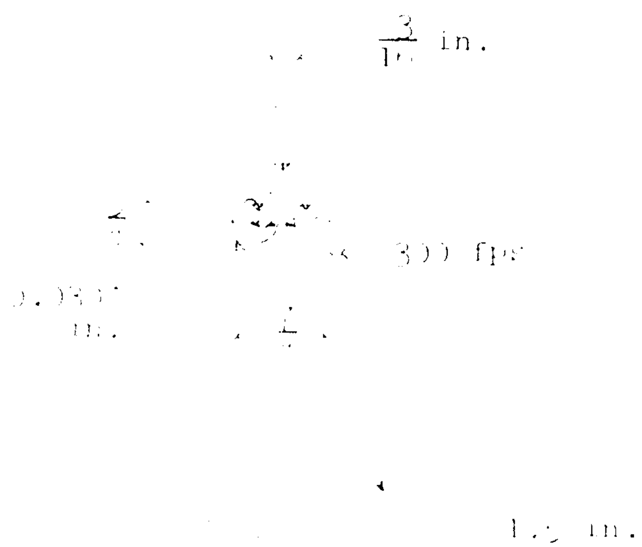

Scale: 1:[illegible]

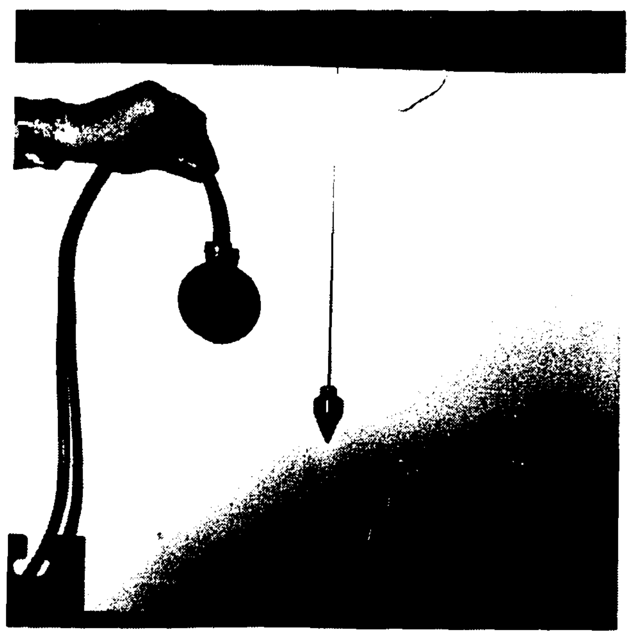

MAIN APPARATUS

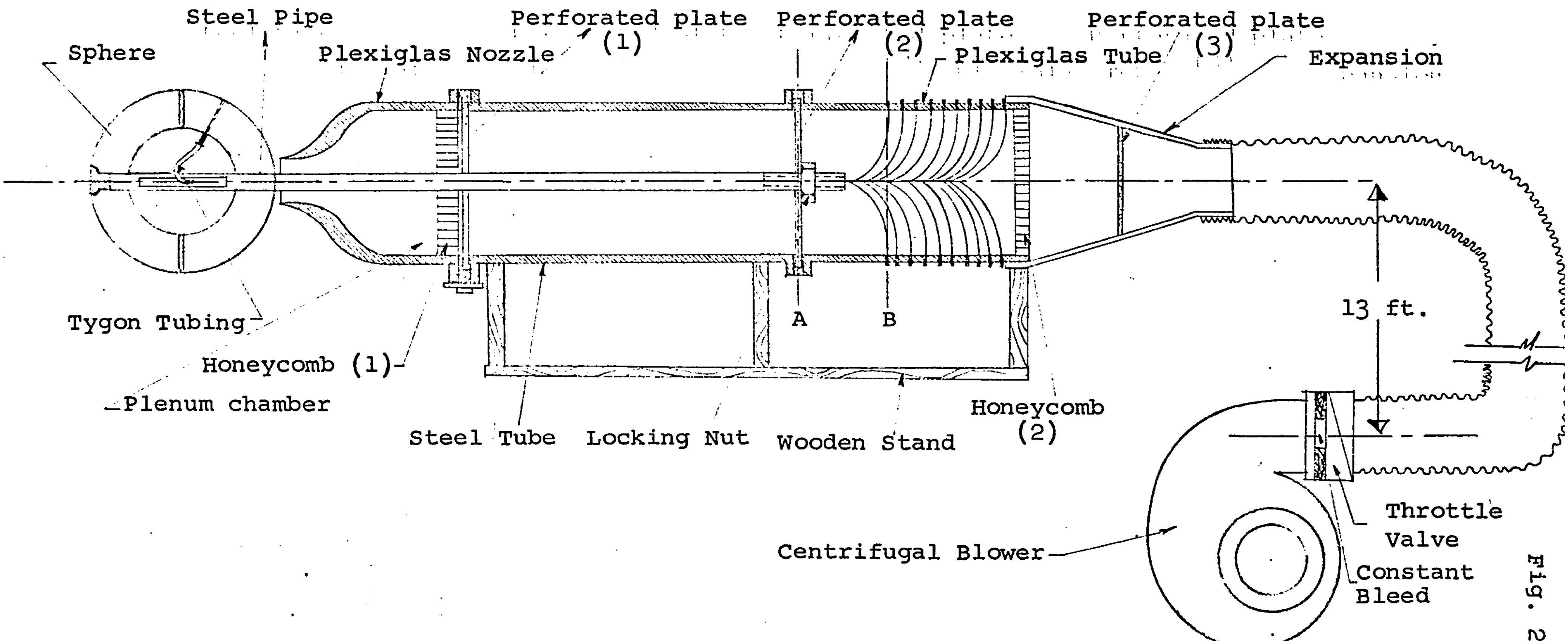

Fig. 2.1

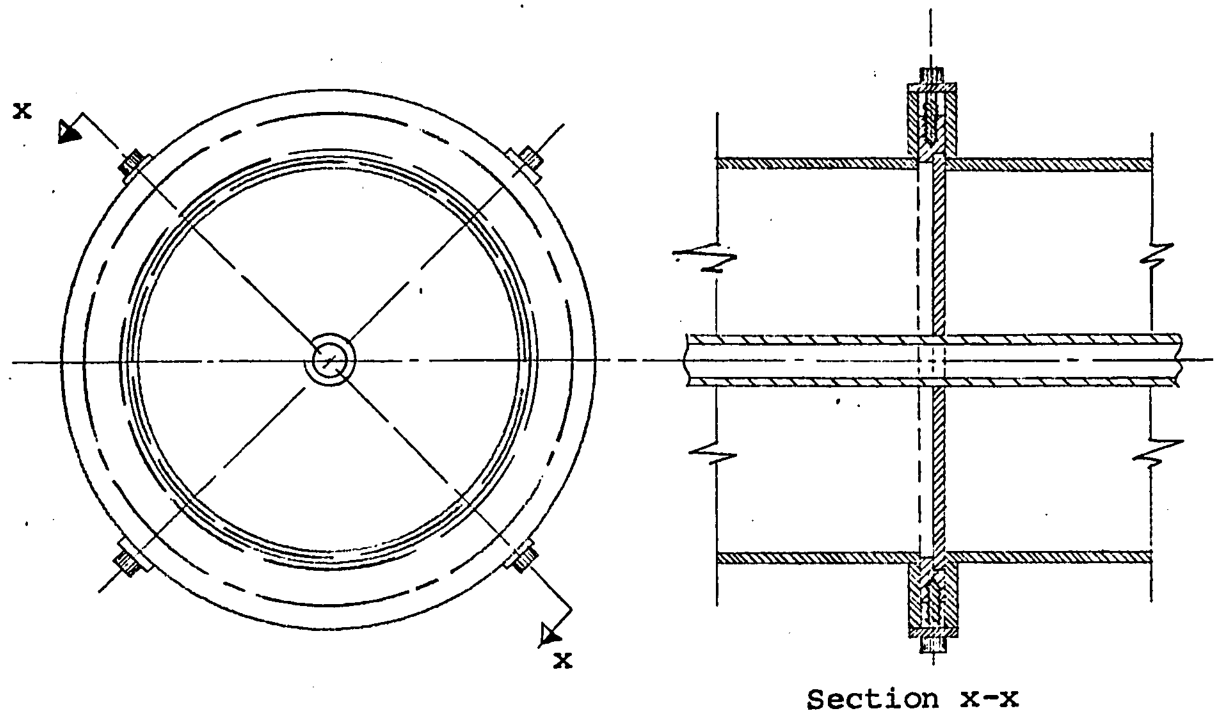

Details "A"

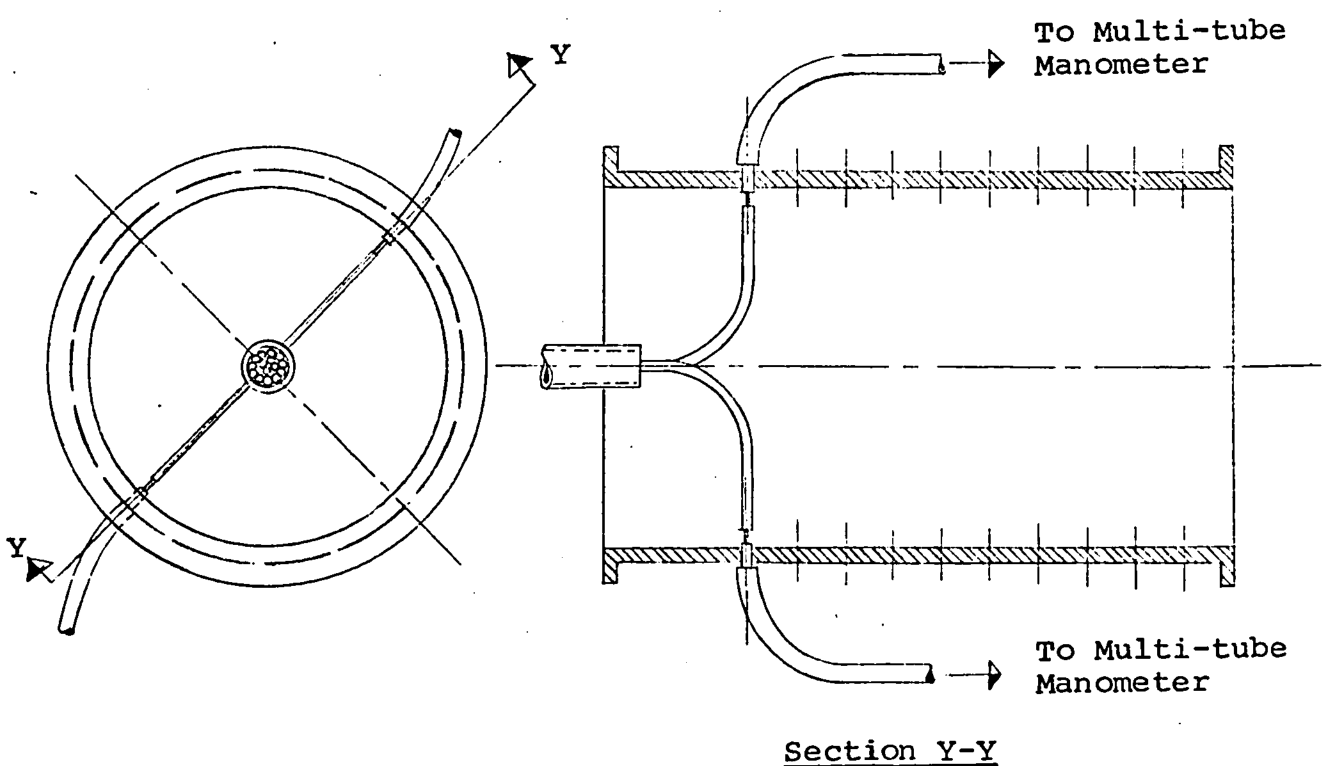

Details "B"

Fig. 2-3

Details of Pressure Taps on the Sphere

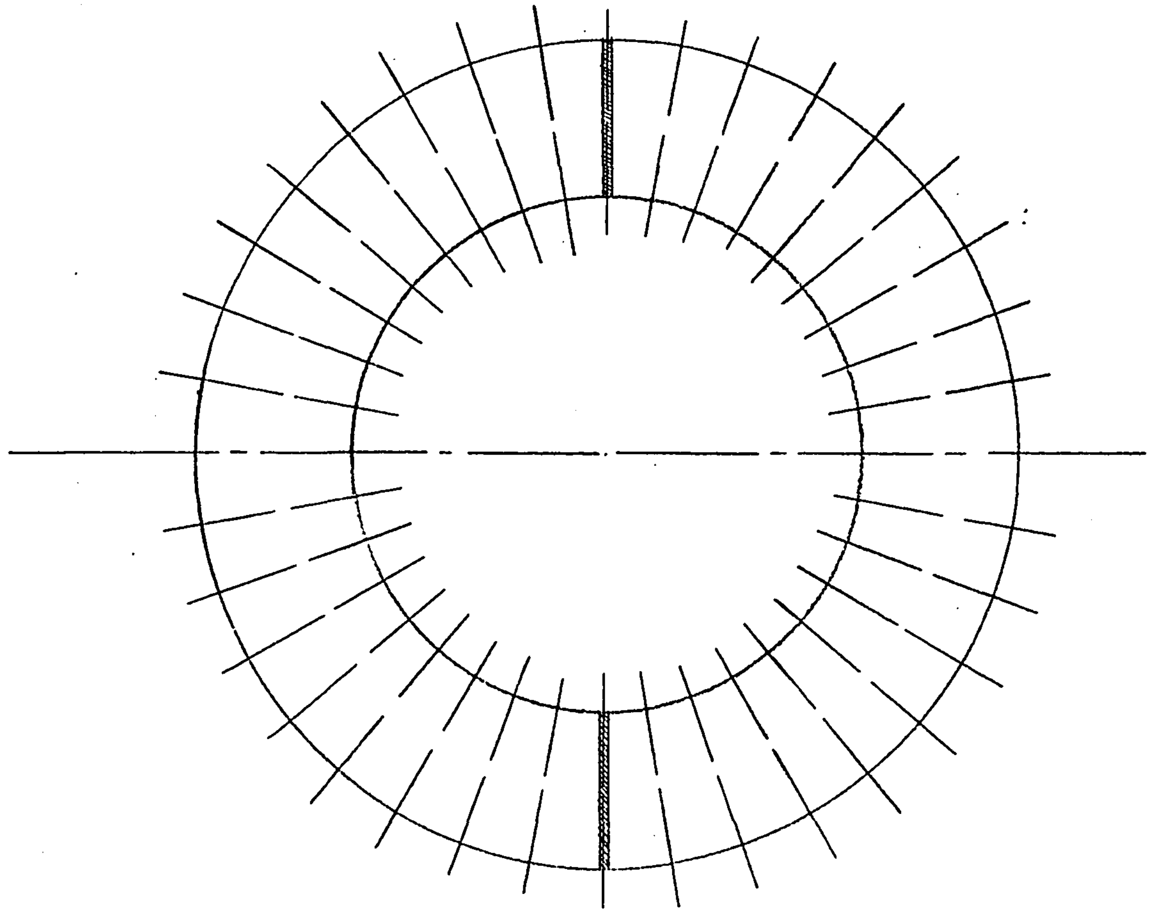

Front View

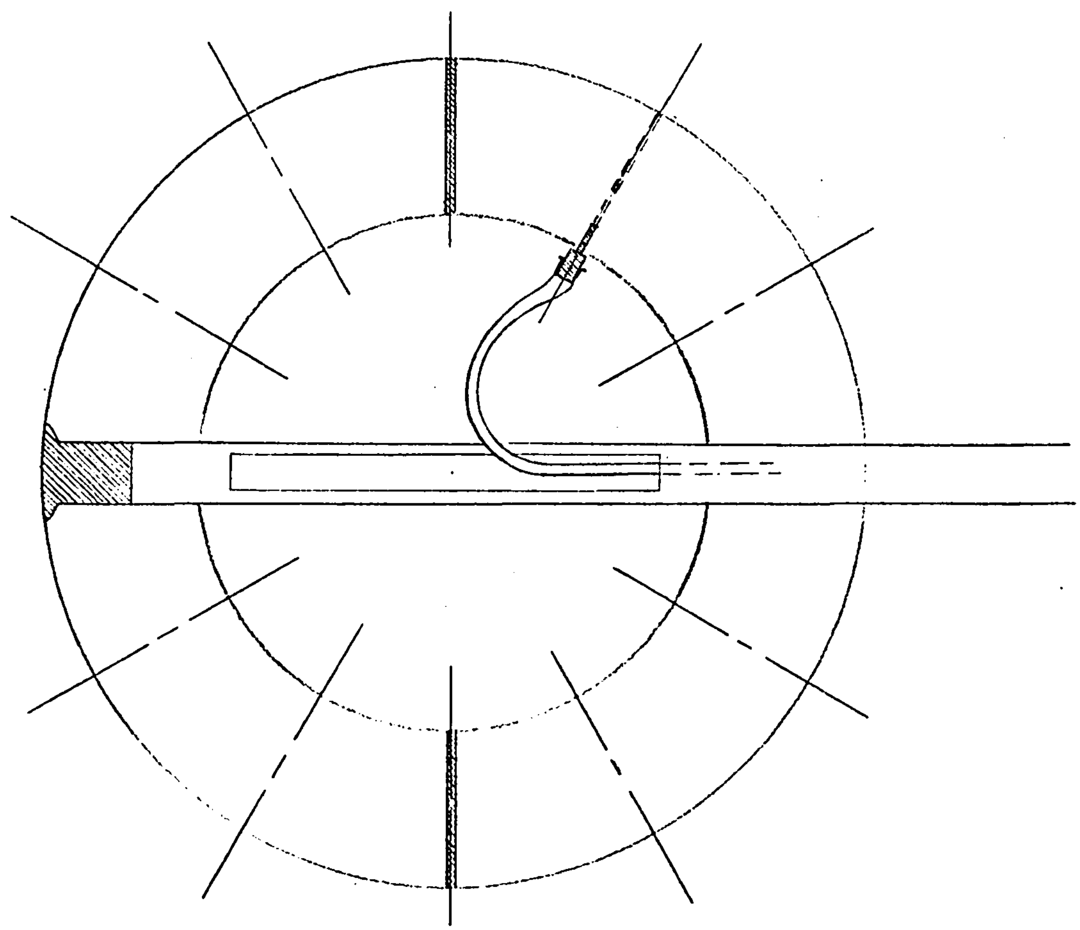

Plan View

INSTRUMENTATION

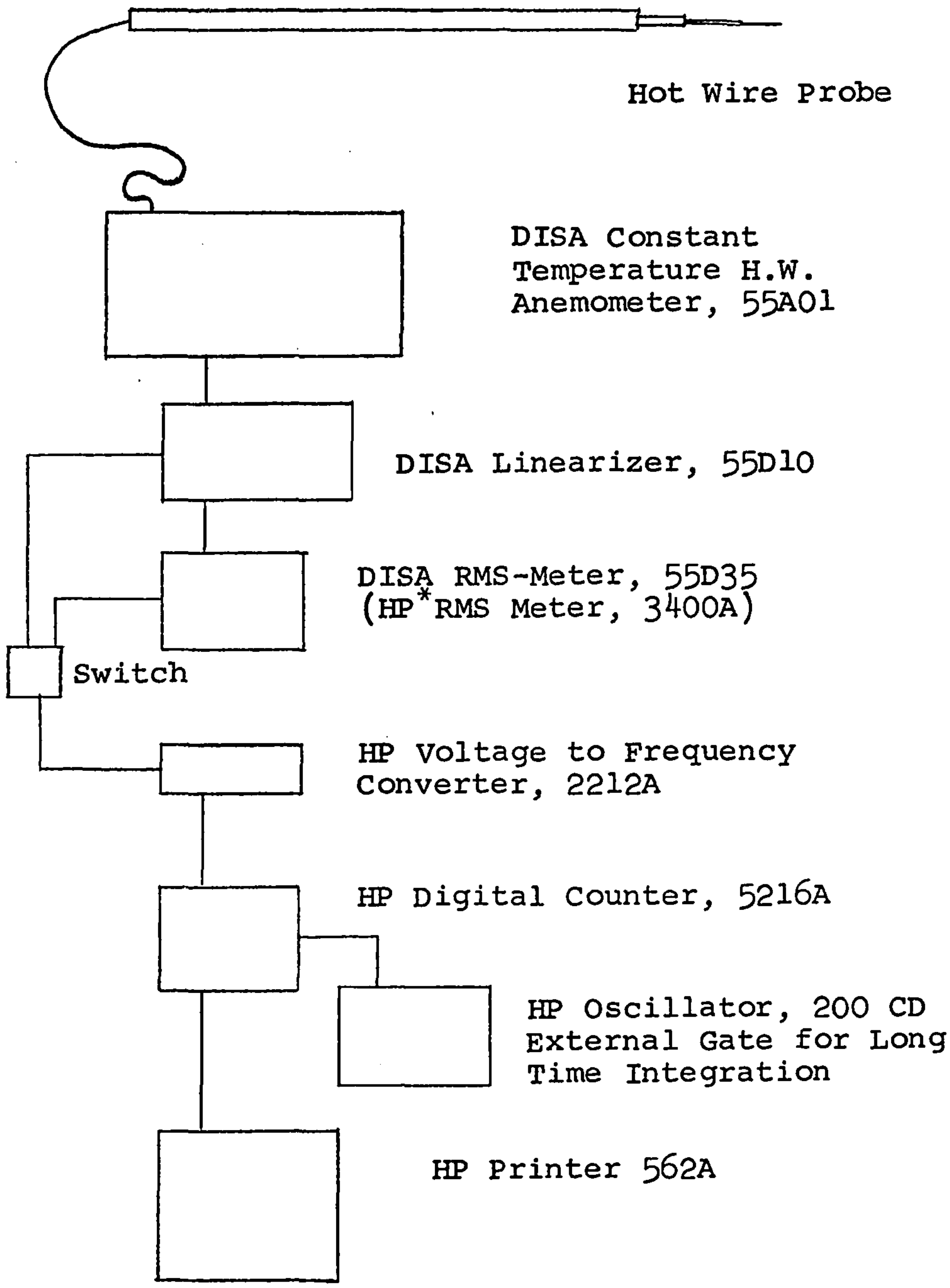

* HP - Hewlett-Packard

EXPERIMENTAL ARRANGEMENT

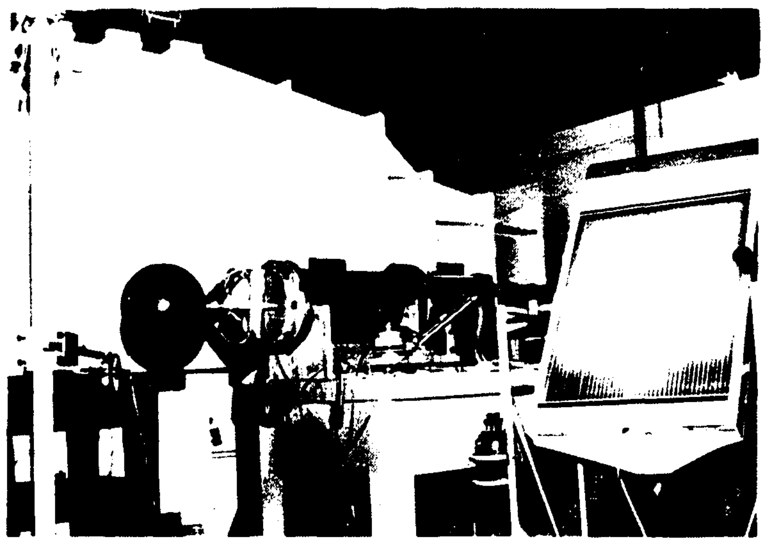

EXPERIMENTAL ARRANGEMENT

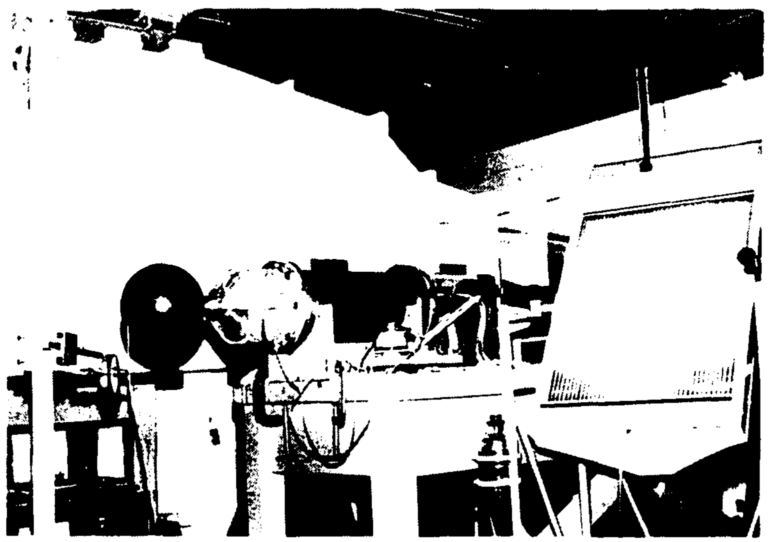

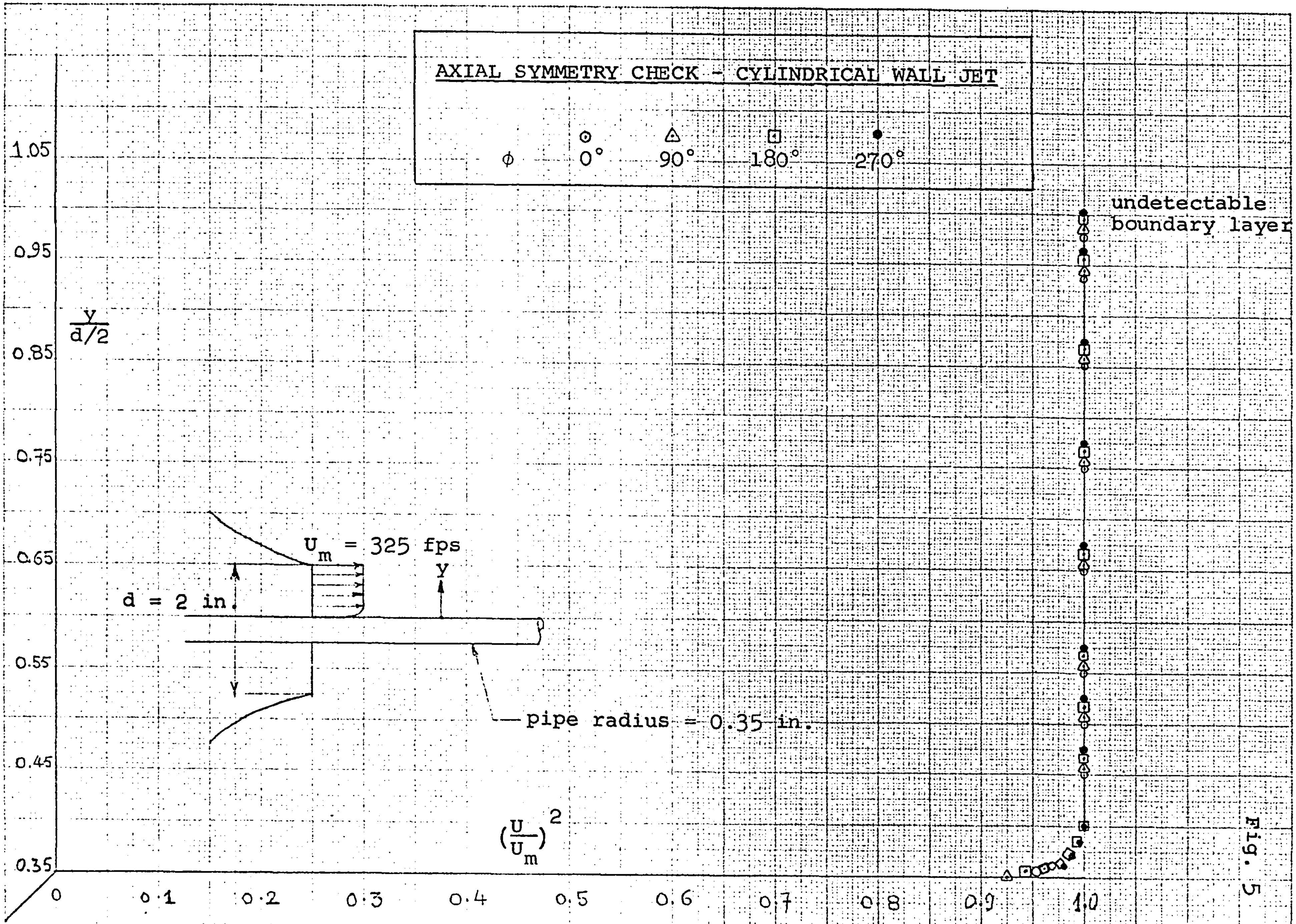

AXIAL SYMMETRY CHECK - CYLINDRICAL WALL JET
φ 0° 90° 180° 270°
undetectable boundary layer
y/(d/2)
1.05
0.95
0.85
0.75
0.65
0.55
0.45
0.35
U_m = 325 fps
y
d = 2 in.
pipe radius = 0.35 in.
(U/U_m)^2
0
0.1
0.2
0.3
0.4
0.5
0.6
0.7
0.8
0.9
1.0

Fig. 5

Fig. 6

CALIBRATION OF THE DOWNSTREAM PERFORATED PLATE

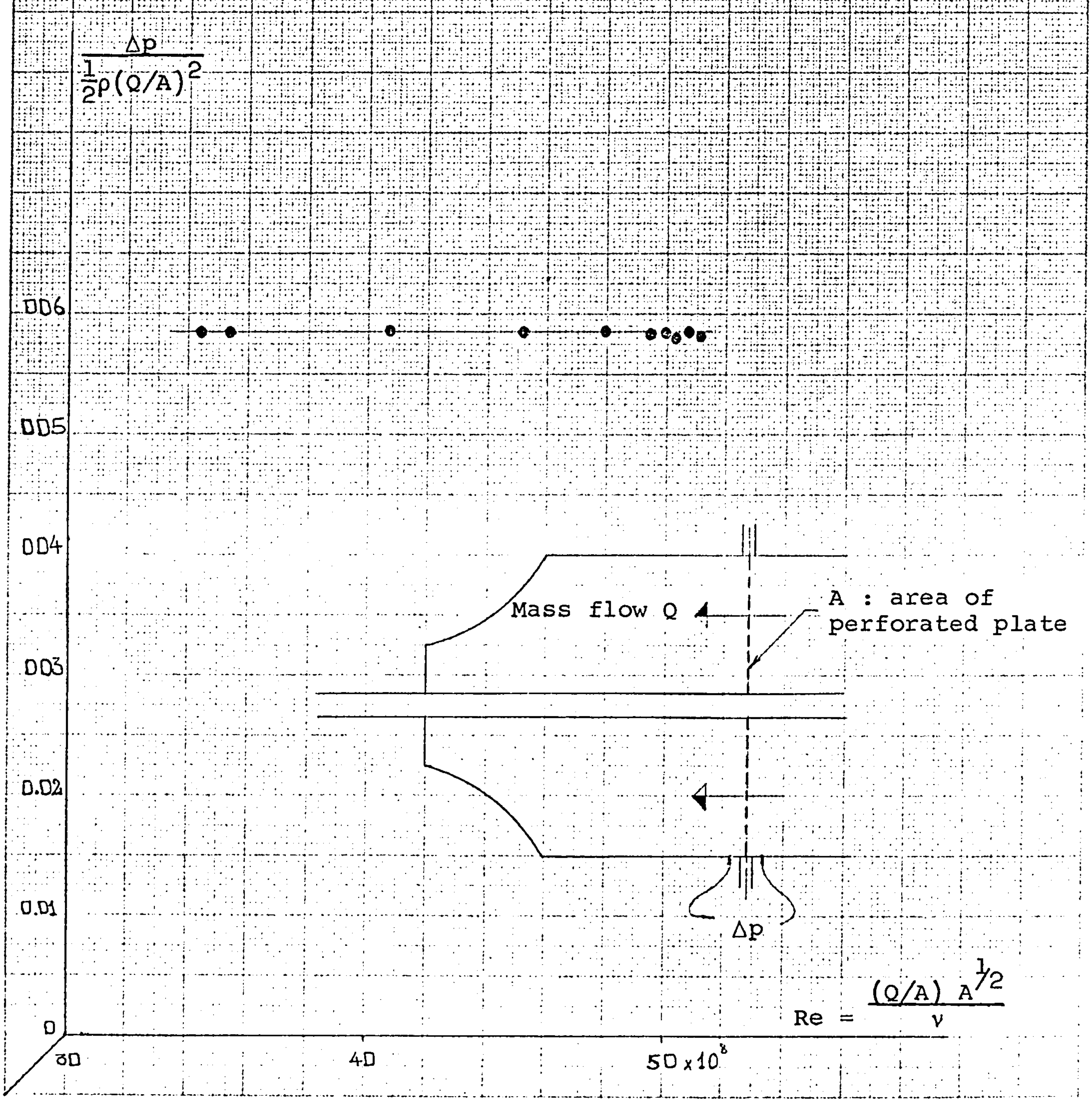

Fig. 7

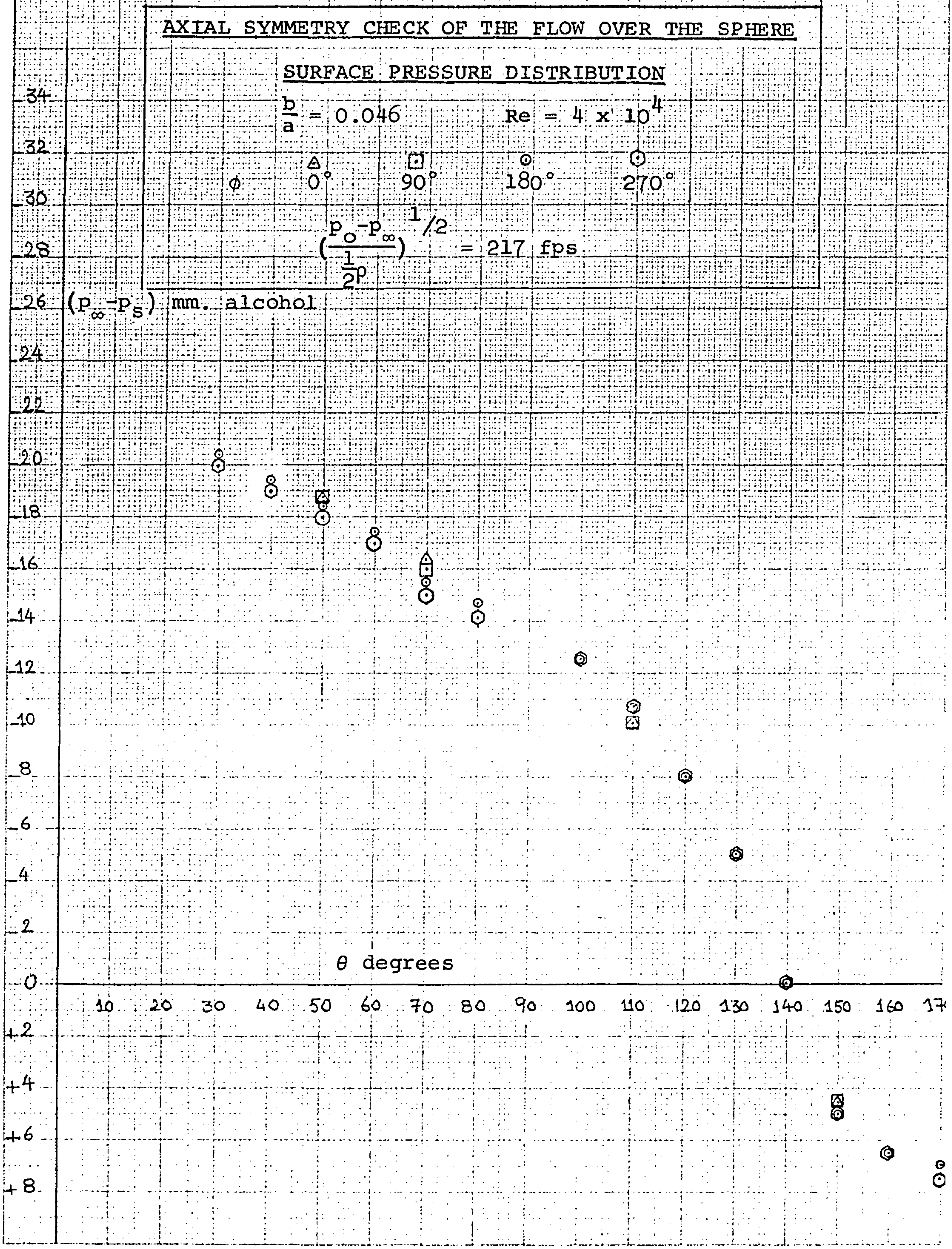

AXIAL SYMMETRY CHECK OF THE FLOW OVER THE SPHERE
SURFACE PRESSURE DISTRIBUTION
$\frac{b}{a} = 0.046$
$Re = 4 \times 10^4$
ϕ
0°
90°
180°
270°
$\left(\frac{p_o - p_\infty}{\frac{1}{2}\rho}\right)^{1/2} = 217$ fps
$(p_\infty - p_s)$ mm. alcohol
θ degrees
34
32
30
28
26
24
22
20
18
16
14
12
10
8
6
4
2
0
+2
+4
+6
+8
10
20
30
40
50
60
70
80
90
100
110
120
130
140
150
160
17

Fig. 8

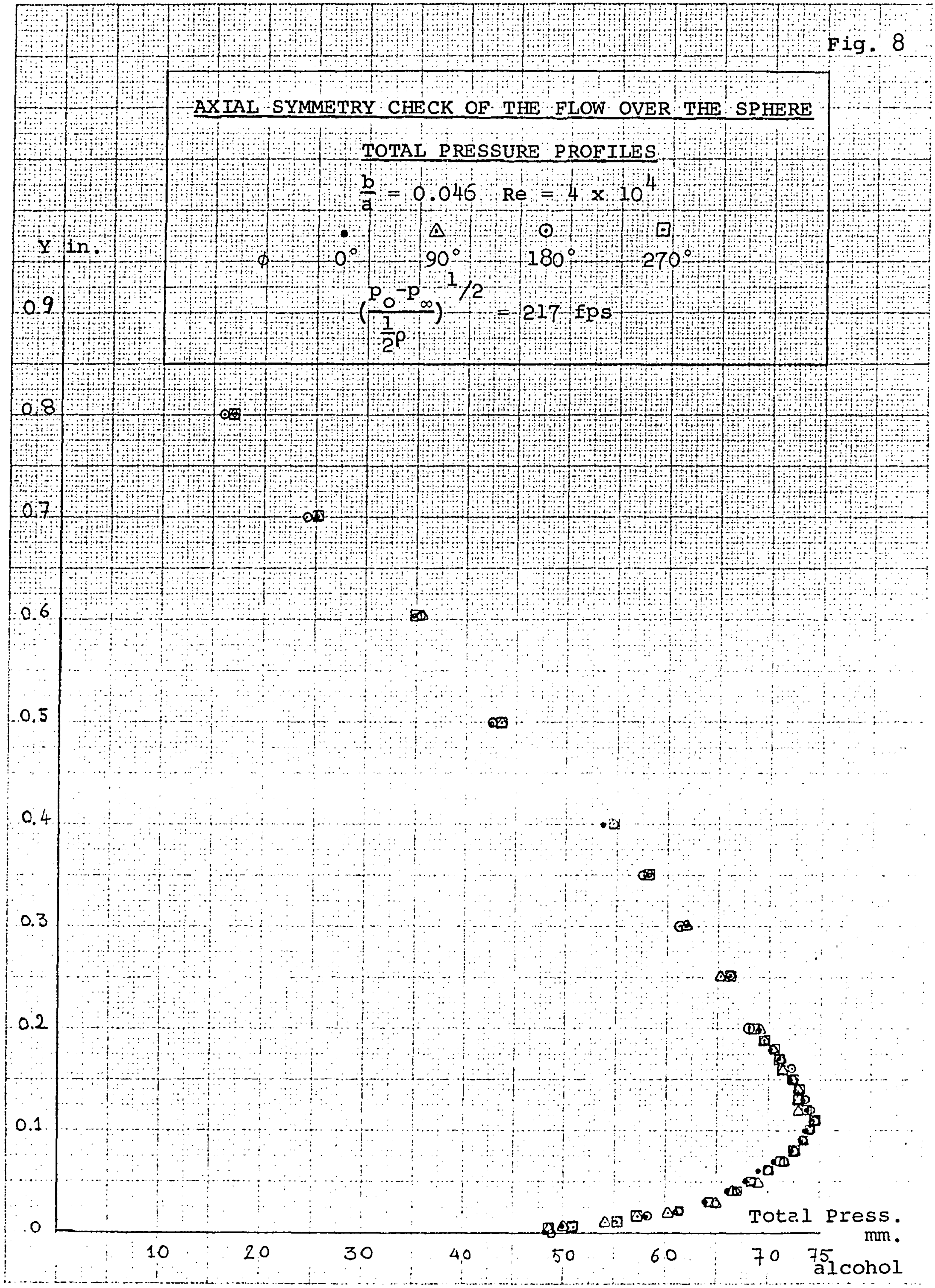
AXIAL SYMMETRY CHECK OF THE FLOW OVER THE SPHERE
TOTAL PRESSURE PROFILES
b/a = 0.046 Re = 4 x 10^4
φ 0° 90° 180° 270°
((p_o - p_∞)/(½ρ))^½ = 217 fps
Y in.
0.9
0.8
0.7
0.6
0.5
0.4
0.3
0.2
0.1
0
10
20
30
40
50
60
70
75
Total Press. mm. alcohol

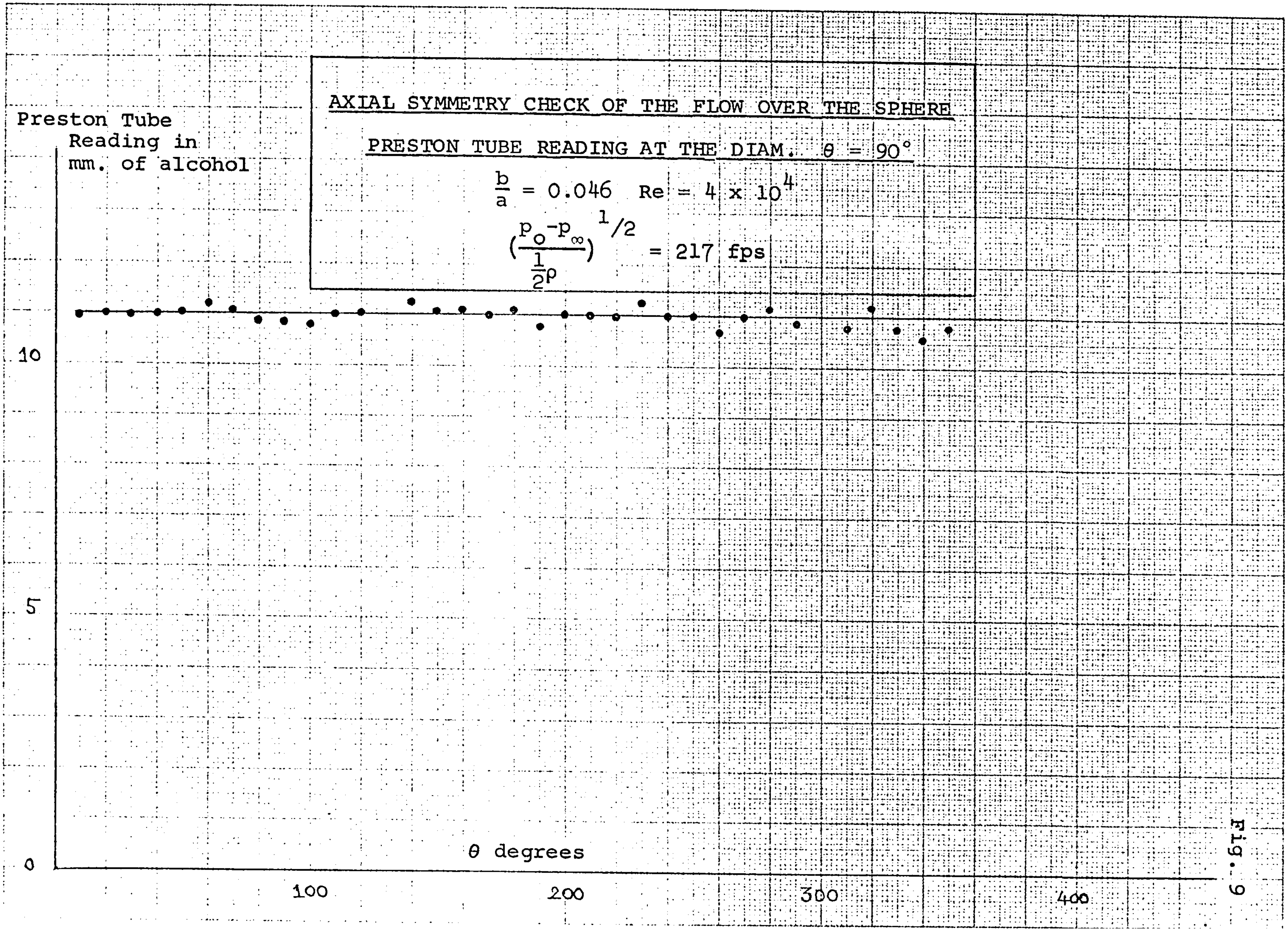
AXIAL SYMMETRY CHECK OF THE FLOW OVER THE SPHERE
PRESTON TUBE READING AT THE DIAM. $\theta = 90°$
$\frac{b}{a} = 0.046$ Re = 4×10^4
$\left(\frac{p_o - p_\infty}{\frac{1}{2}\rho}\right)^{1/2} = 217$ fps
Preston Tube Reading in mm. of alcohol
10
5
0
θ degrees
100
200
300
400

Fig. 9

Fig. 10-1

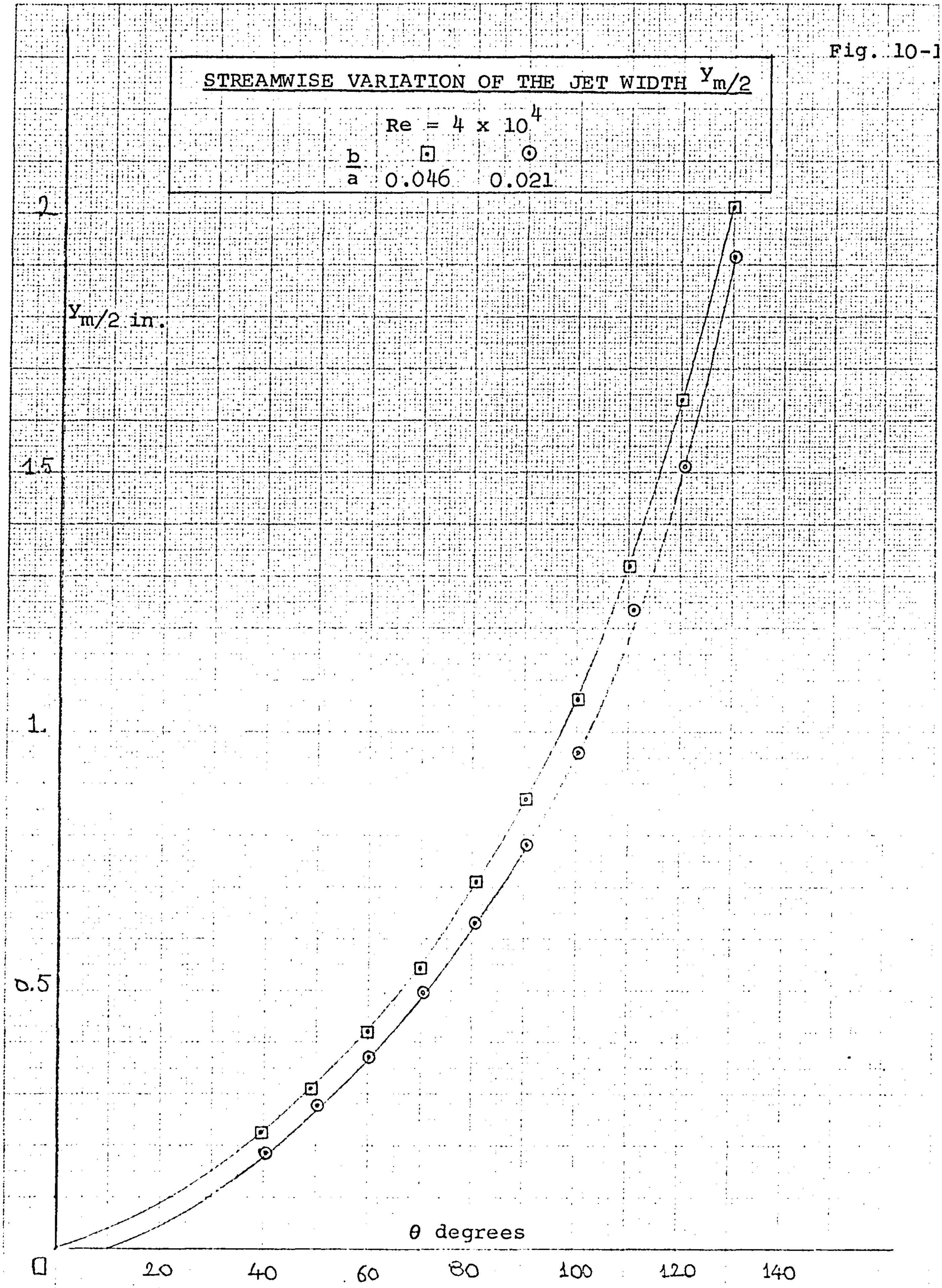

STREAMWISE VARIATION OF THE JET WIDTH $y_{m/2}$
Re = 4×10^4
$\frac{b}{a}$ ⊡ 0.046 ⊙ 0.021
$y_{m/2}$ in.
2
1.5
1.
0.5
0
20
40
60
80
100
120
140
θ degrees

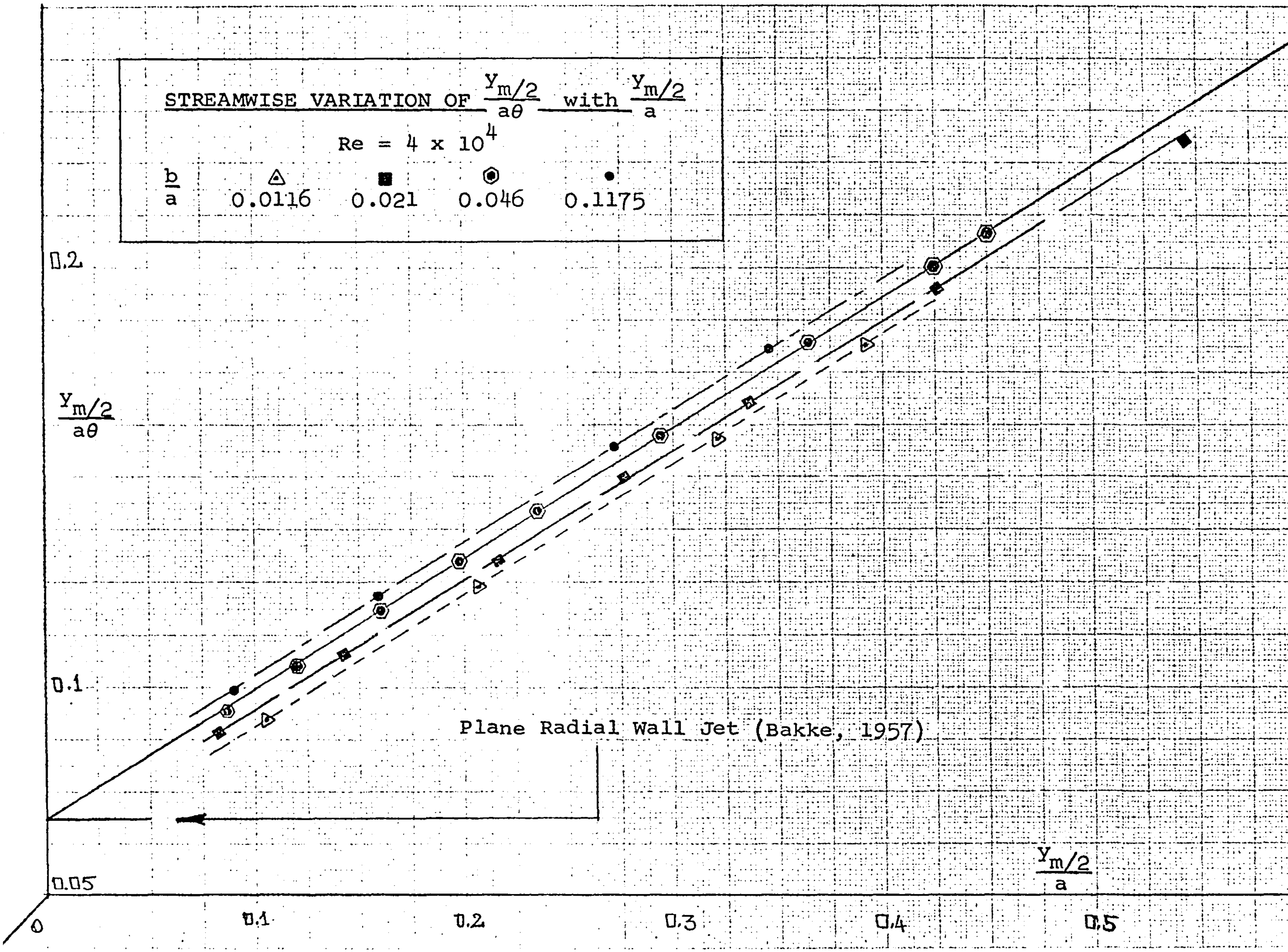
STREAMWISE VARIATION OF $\frac{y_{m/2}}{a\theta}$ with $\frac{y_{m/2}}{a}$
Re = 4×10^4
$\frac{b}{a}$ 0.0116 0.021 0.046 0.1175
$\frac{y_{m/2}}{a\theta}$
0.2
0.1
0.05
Plane Radial Wall Jet (Bakke, 1957)
$\frac{y_{m/2}}{a}$
0
0.1
0.2
0.3
0.4
0.5

Fig. 10-2

AXI-SYMMETRIC WALL JET ROUND A SPHERE

Scale: 1:4

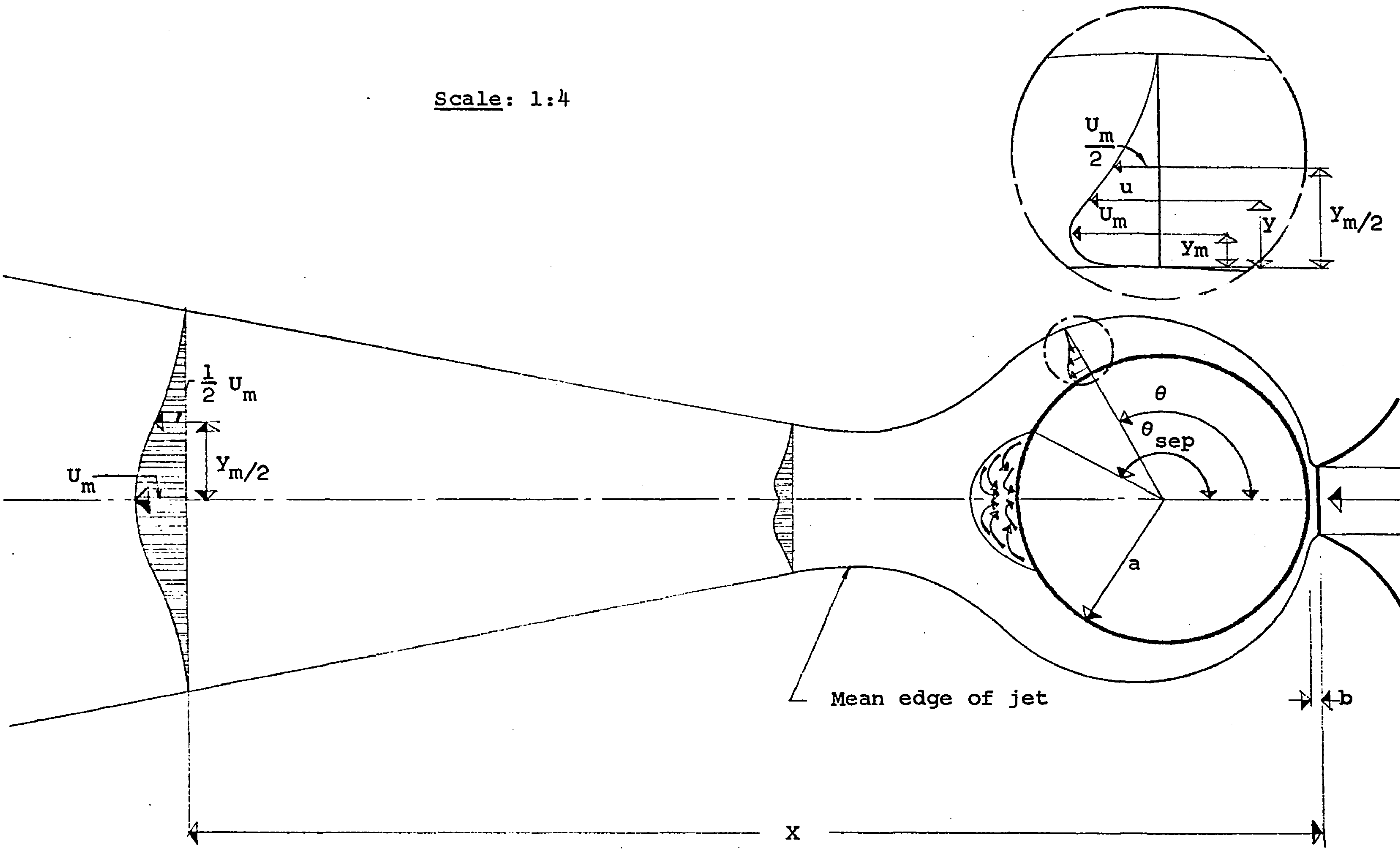

Fig. 11-2

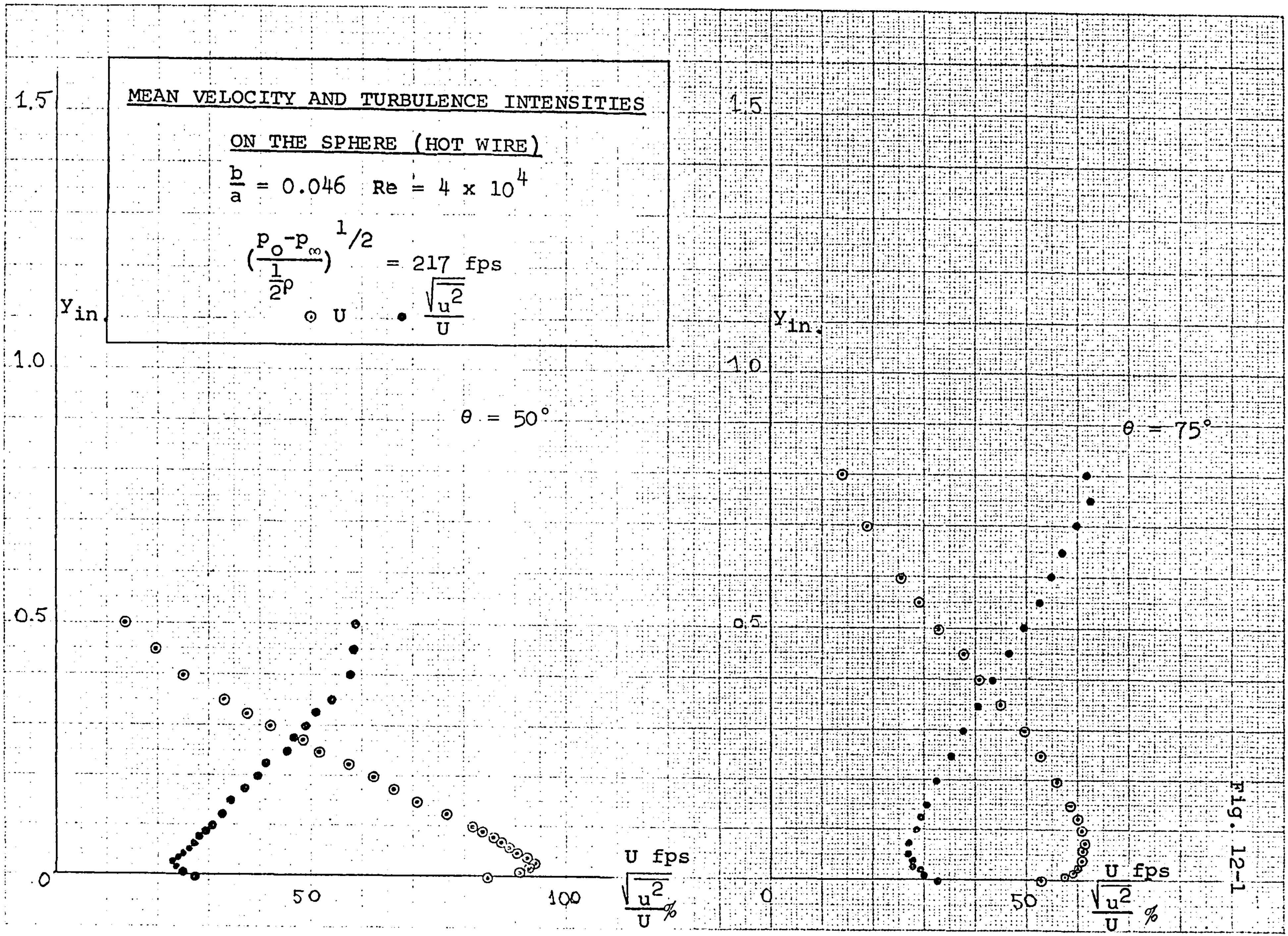
MEAN VELOCITY AND TURBULENCE INTENSITIES
ON THE SPHERE (HOT WIRE)
$\frac{b}{a} = 0.046$ Re $= 4 \times 10^4$
$\left(\frac{p_o - p_\infty}{\frac{1}{2}\rho}\right)^{1/2} = 217$ fps
⊙ U ● $\frac{\sqrt{\overline{u^2}}}{U}$
$y_{in.}$
1.5
1.0
0.5
0
50
100
$\theta = 50°$
$\theta = 75°$
U fps
$\frac{\sqrt{\overline{u^2}}}{U}$ %

Fig. 12-1

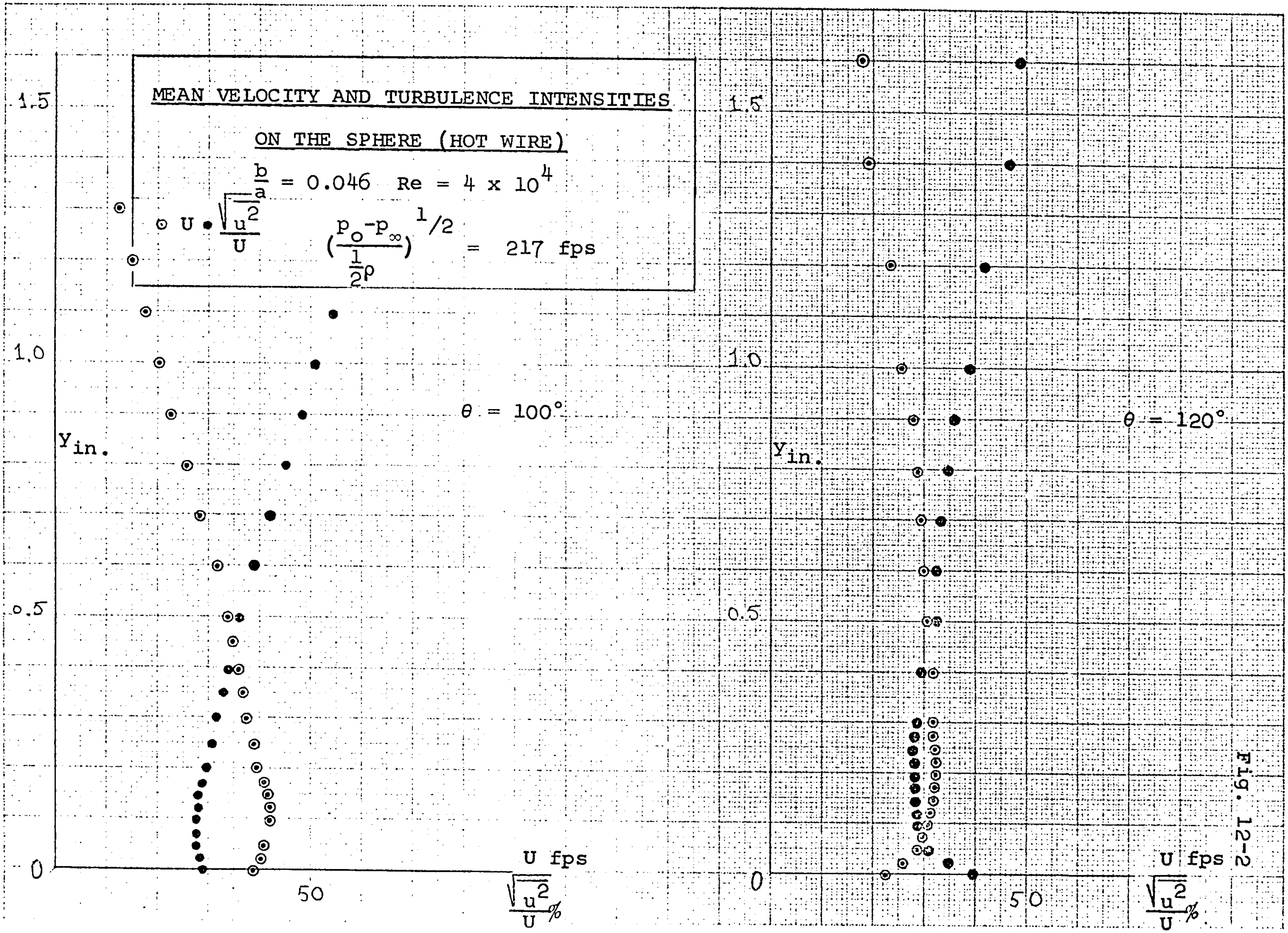

MEAN VELOCITY AND TURBULENCE INTENSITIES
ON THE SPHERE (HOT WIRE)
$\frac{b}{a} = 0.046$ Re = 4×10^4
⊙ U • $\frac{\sqrt{\overline{u^2}}}{U}$
$\left(\frac{p_o - p_\infty}{\frac{1}{2}\rho}\right)^{1/2} = 217$ fps
$\theta = 100°$
$\theta = 120°$
$y_{in.}$
1.5
1.0
0.5
0
50
U fps
$\frac{\sqrt{\overline{u^2}}}{U}\%$

Fig. 12-2

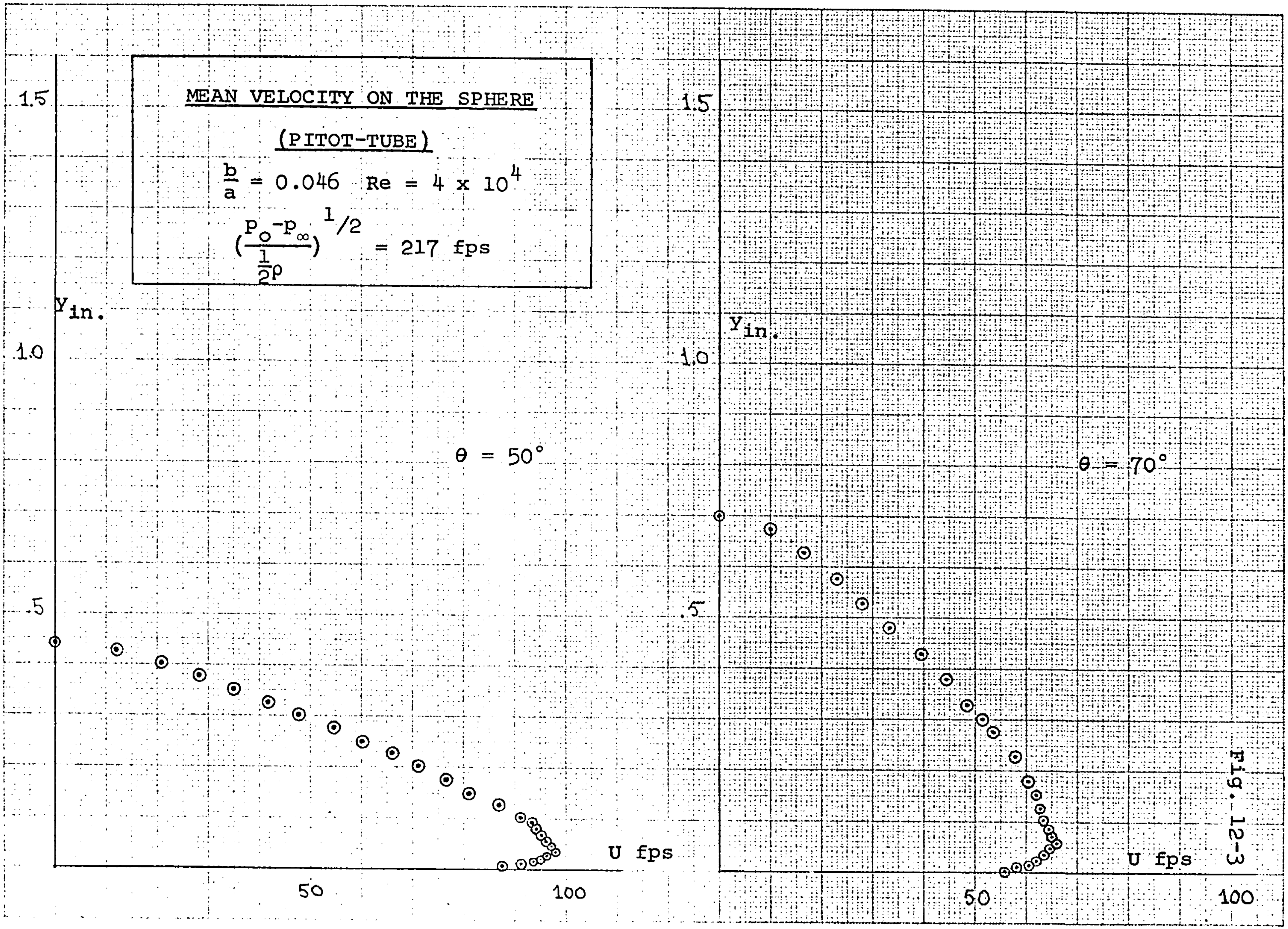

MEAN VELOCITY ON THE SPHERE
(PITOT-TUBE)
$\frac{b}{a} = 0.046 \quad Re = 4 \times 10^4$
$\left(\frac{p_o - p_\infty}{\frac{1}{2}\rho}\right)^{1/2} = 217$ fps
$y_{in.}$
1.5
1.0
.5
$\theta = 50°$
U fps
50
100
$y_{in.}$
1.5
1.0
.5
$\theta = 70°$
U fps
50
100

Fig. 12-3

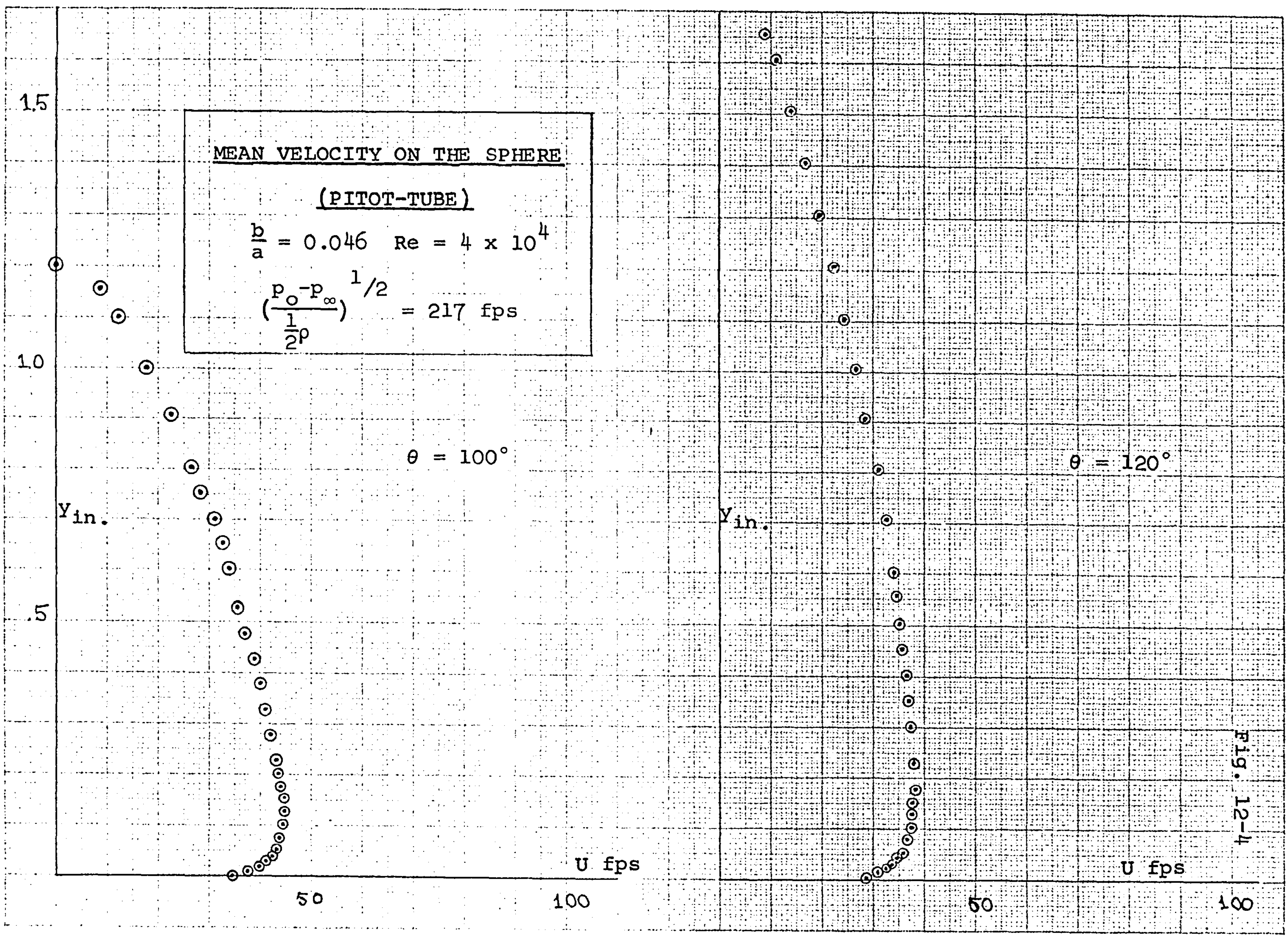
MEAN VELOCITY ON THE SPHERE
(PITOT-TUBE)
$\frac{b}{a} = 0.046 \quad Re = 4 \times 10^4$
$\left(\frac{p_o - p_\infty}{\frac{1}{2}\rho}\right)^{1/2} = 217$ fps
1.5
1.0
.5
$y_{in.}$
$\theta = 100°$
U fps
50
100
$y_{in.}$
$\theta = 120°$
U fps
50
100

Fig. 12-4

Fig. 12-5

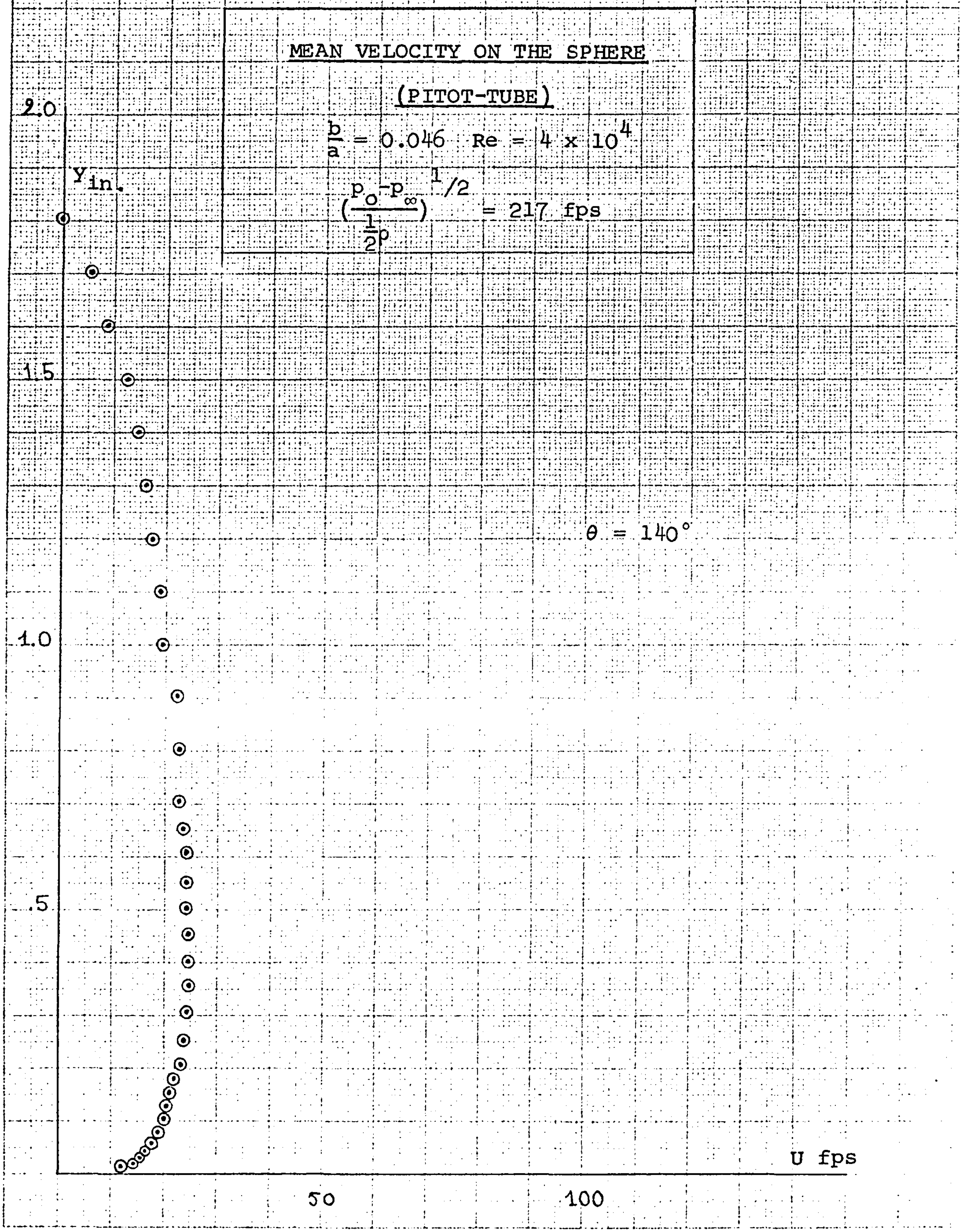

MEAN VELOCITY ON THE SPHERE
(PITOT-TUBE)
$\frac{b}{a} = 0.046$ Re = 4×10^4
$\left(\frac{p_o - p_\infty}{\frac{1}{2}\rho}\right)^{1/2} = 217$ fps
θ = 140°
$Y_{in.}$
2.0
1.5
1.0
.5
U fps
50
100

Fig. 13

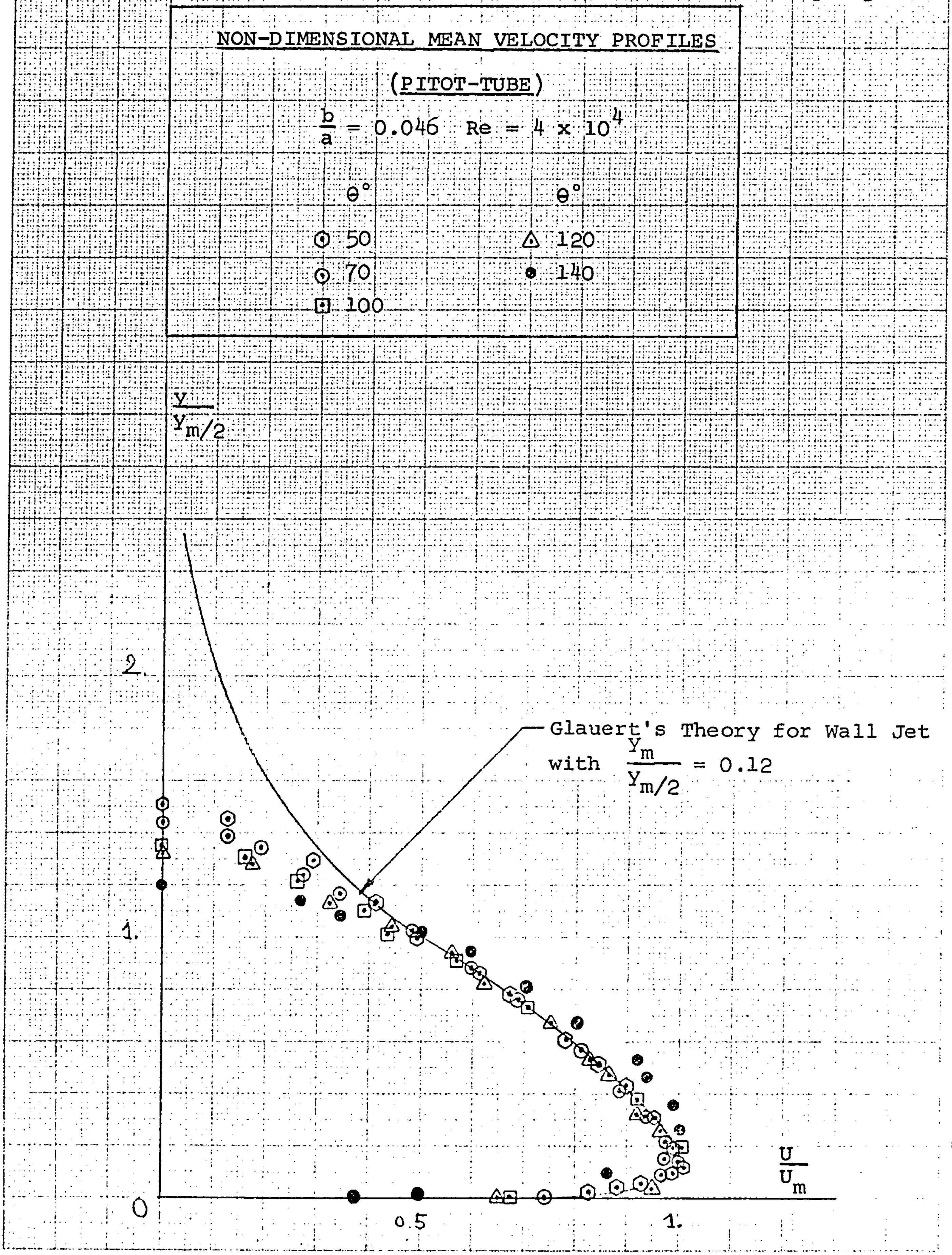
NON-DIMENSIONAL MEAN VELOCITY PROFILES
(PITOT-TUBE)
$\frac{b}{a} = 0.046$ Re = 4×10^4
θ°
50
70
100
θ°
120
140
$\frac{y}{y_{m/2}}$
2.
1.
0
0.5
1.
$\frac{U}{U_m}$
Glauert's Theory for Wall Jet with $\frac{y_m}{y_{m/2}} = 0.12$

Fig. 14-1

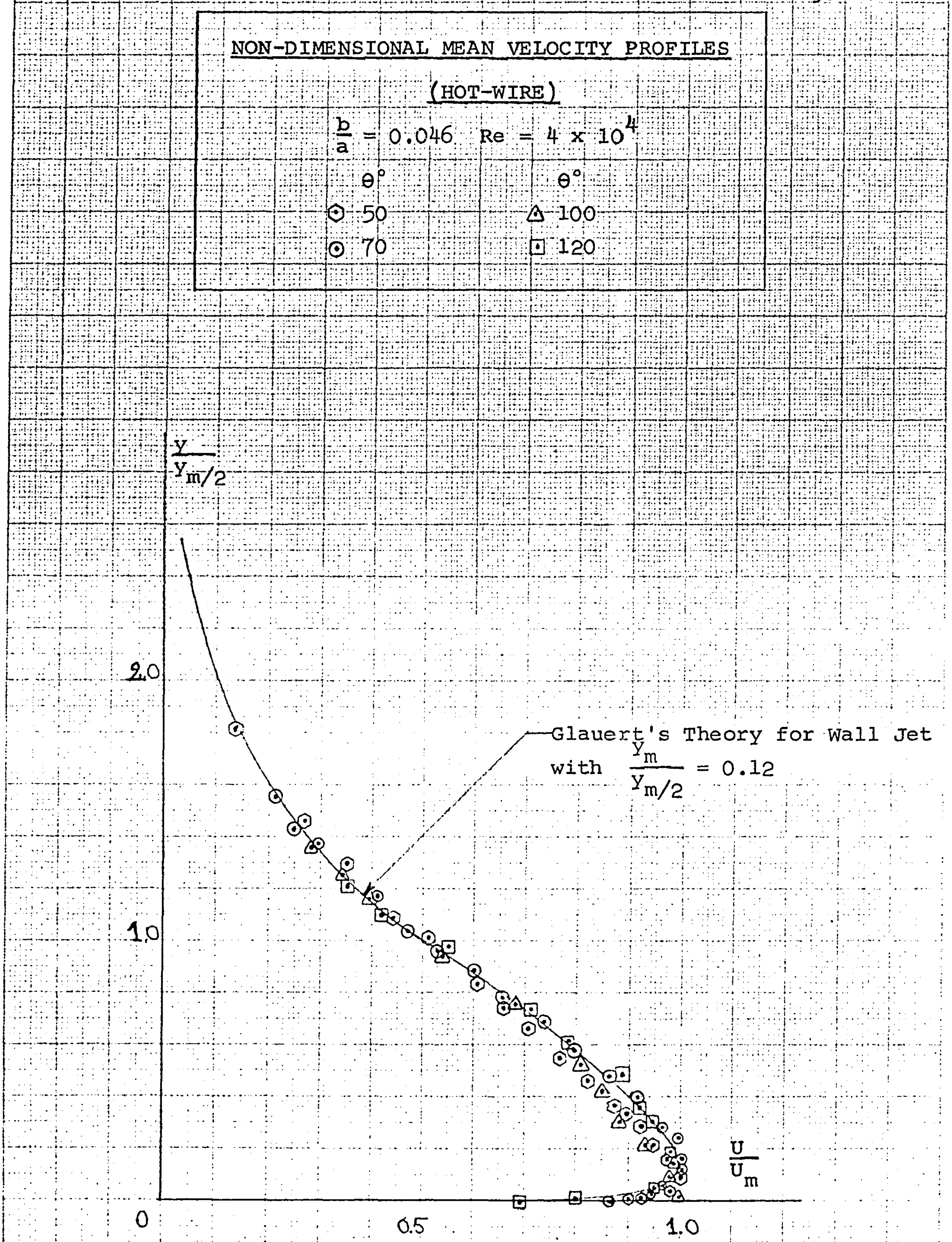

NON-DIMENSIONAL MEAN VELOCITY PROFILES
(HOT-WIRE)
$\frac{b}{a} = 0.046$ Re = 4×10^4
θ° 50
θ° 70
θ° 100
θ° 120
$\frac{y}{y_{m/2}}$
2.0
1.0
0
0.5
1.0
$\frac{U}{U_m}$
Glauert's Theory for Wall Jet with $\frac{y_m}{y_{m/2}} = 0.12$

Fig. 14-2

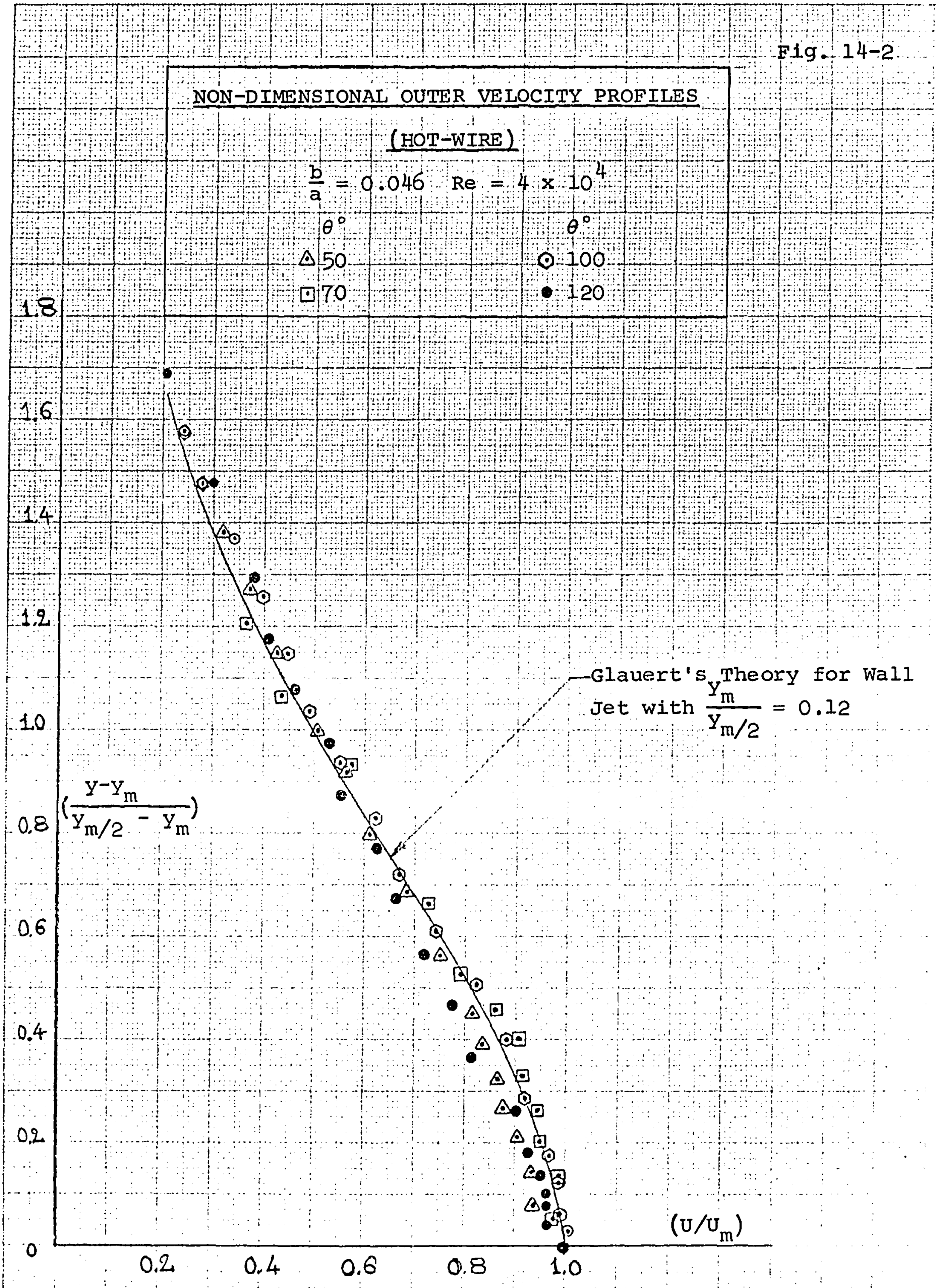
NON-DIMENSIONAL OUTER VELOCITY PROFILES
(HOT-WIRE)
$\frac{b}{a} = 0.046$ Re = 4×10^4
$\theta°$ 50, 70
$\theta°$ 100, 120
1.8
1.6
1.4
1.2
1.0
0.8
0.6
0.4
0.2
0
$(\frac{y - y_m}{y_{m/2} - y_m})$
Glauert's Theory for Wall Jet with $\frac{y_m}{y_{m/2}} = 0.12$
0.2
0.4
0.6
0.8
1.0
(U/U_m)

Fig. 15

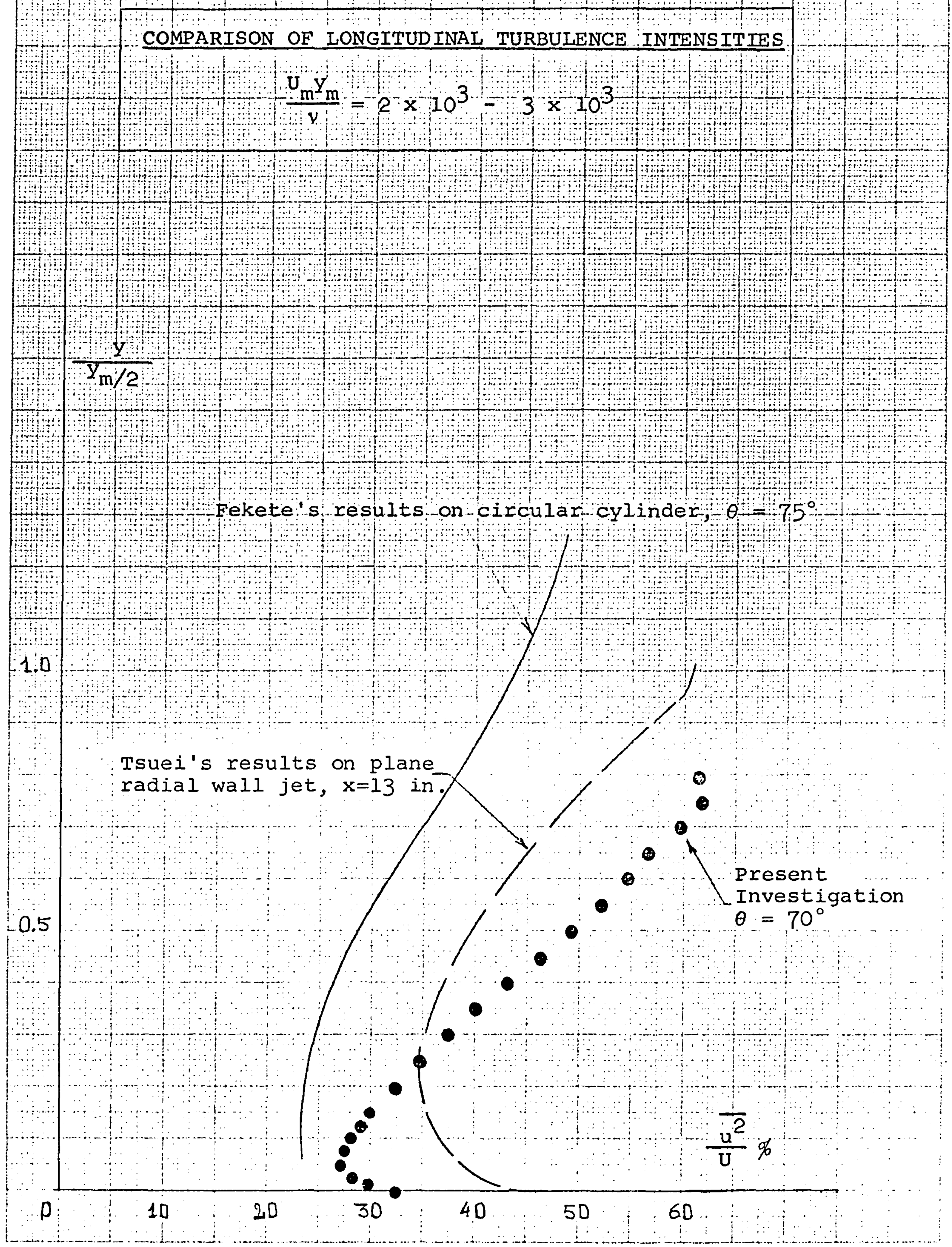
COMPARISON OF LONGITUDINAL TURBULENCE INTENSITIES
$\frac{U_m y_m}{\nu} = 2 \times 10^3 - 3 \times 10^3$
$\frac{y}{y_{m/2}}$
Fekete's results on circular cylinder, $\theta = 75°$
1.0
Tsuei's results on plane radial wall jet, x=13 in.
Present Investigation $\theta = 70°$
0.5
$\frac{\overline{u^2}}{U}$ %
0
10
20
30
40
50
60

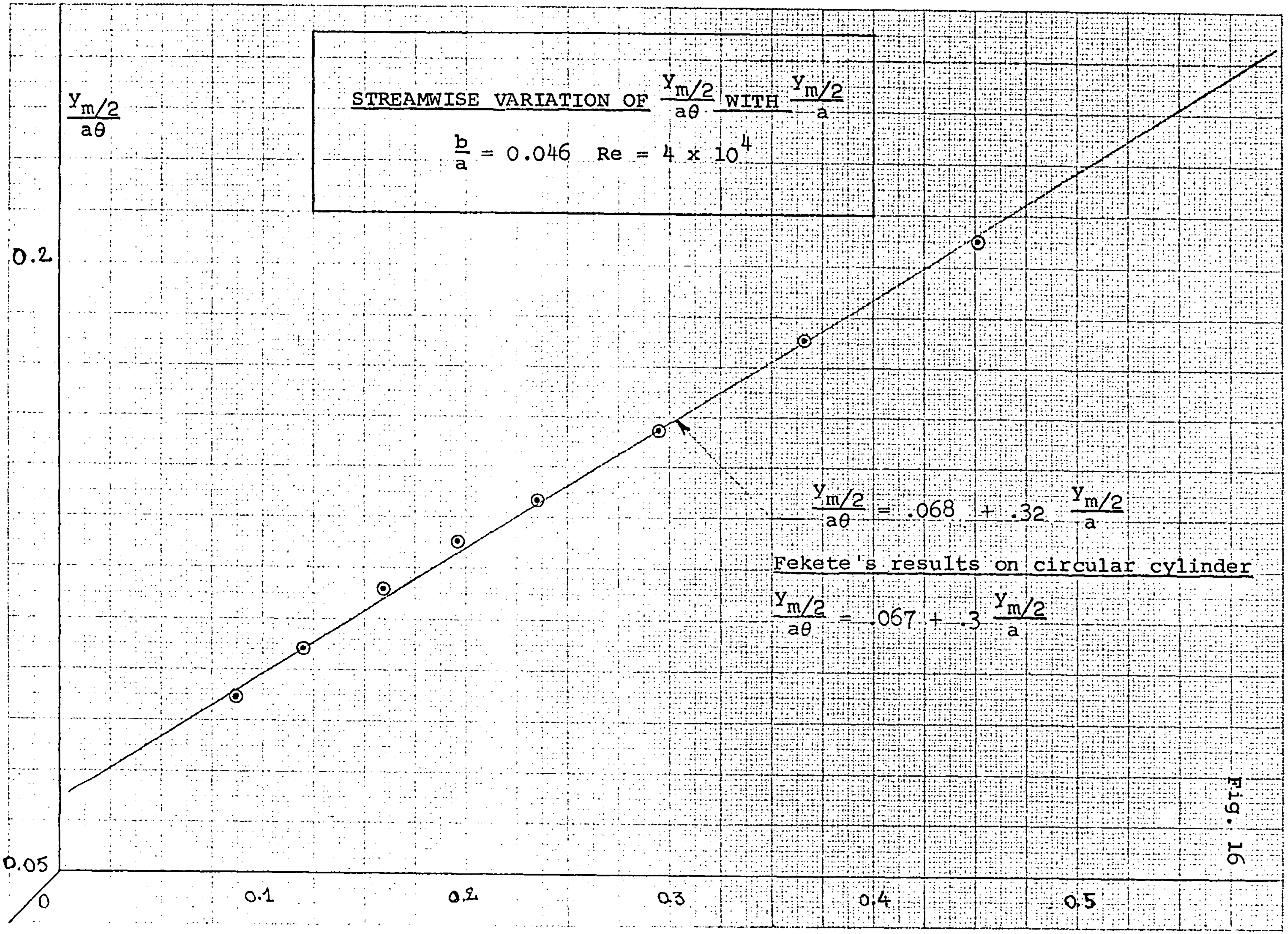
STREAMWISE VARIATION OF $\frac{y_{m/2}}{a\theta}$ WITH $\frac{y_{m/2}}{a}$
$\frac{b}{a} = 0.046 \quad Re = 4 \times 10^4$
$\frac{y_{m/2}}{a\theta}$
0.2
0.05
0
0.1
0.2
0.3
0.4
0.5
$\frac{y_{m/2}}{a\theta} = .068 + .32 \frac{y_{m/2}}{a}$
Fekete's results on circular cylinder
$\frac{y_{m/2}}{a\theta} = .067 + .3 \frac{y_{m/2}}{a}$

Fig. 16

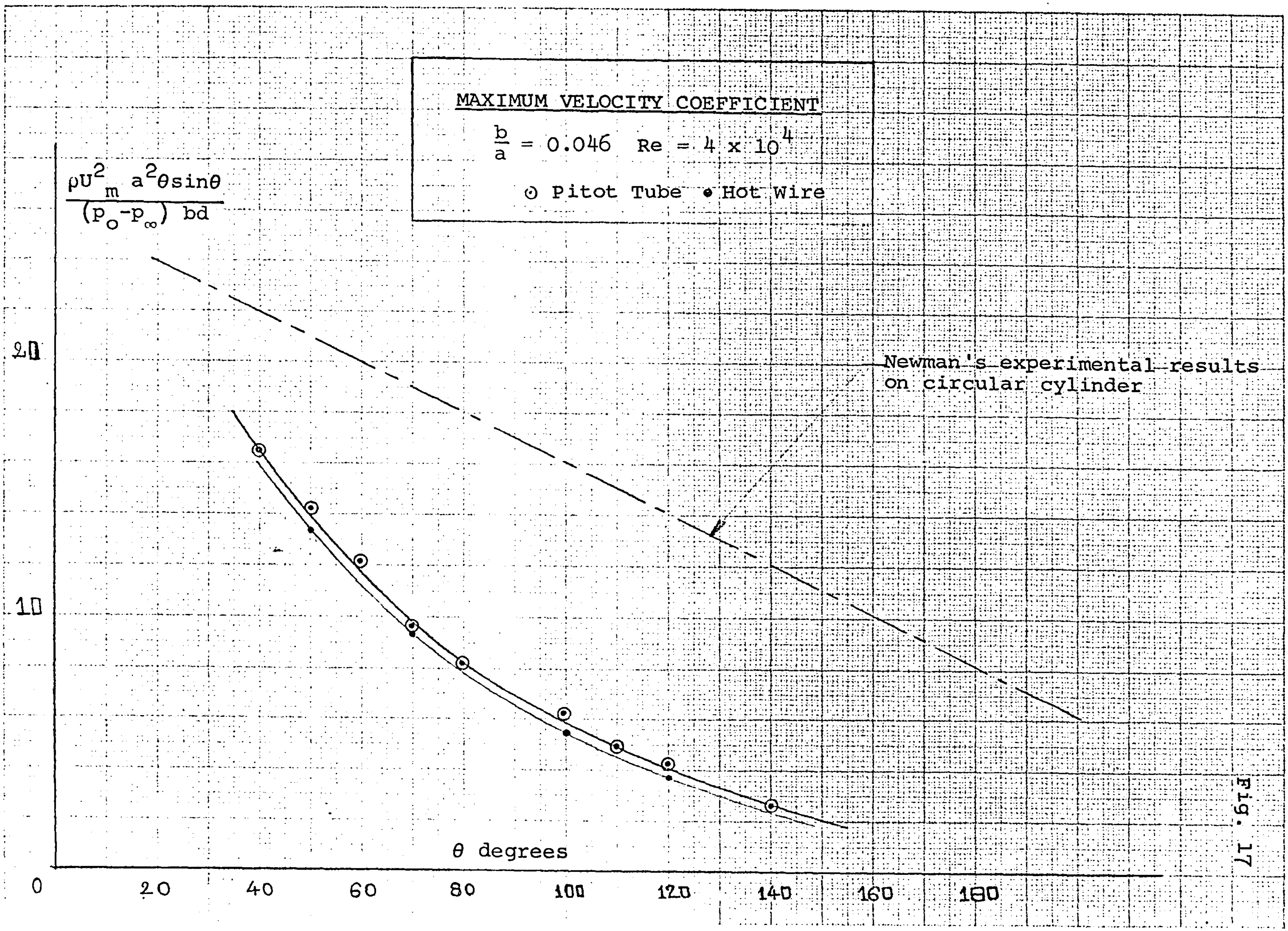
MAXIMUM VELOCITY COEFFICIENT
$\frac{b}{a} = 0.046$ Re $= 4 \times 10^4$
⊙ Pitot Tube • Hot Wire
$\frac{\rho U_m^2 \, a^2 \theta \sin\theta}{(p_o - p_\infty)\, bd}$
Newman's experimental results on circular cylinder
θ degrees
0
10
20
0
20
40
60
80
100
120
140
160
180

Fig. 17

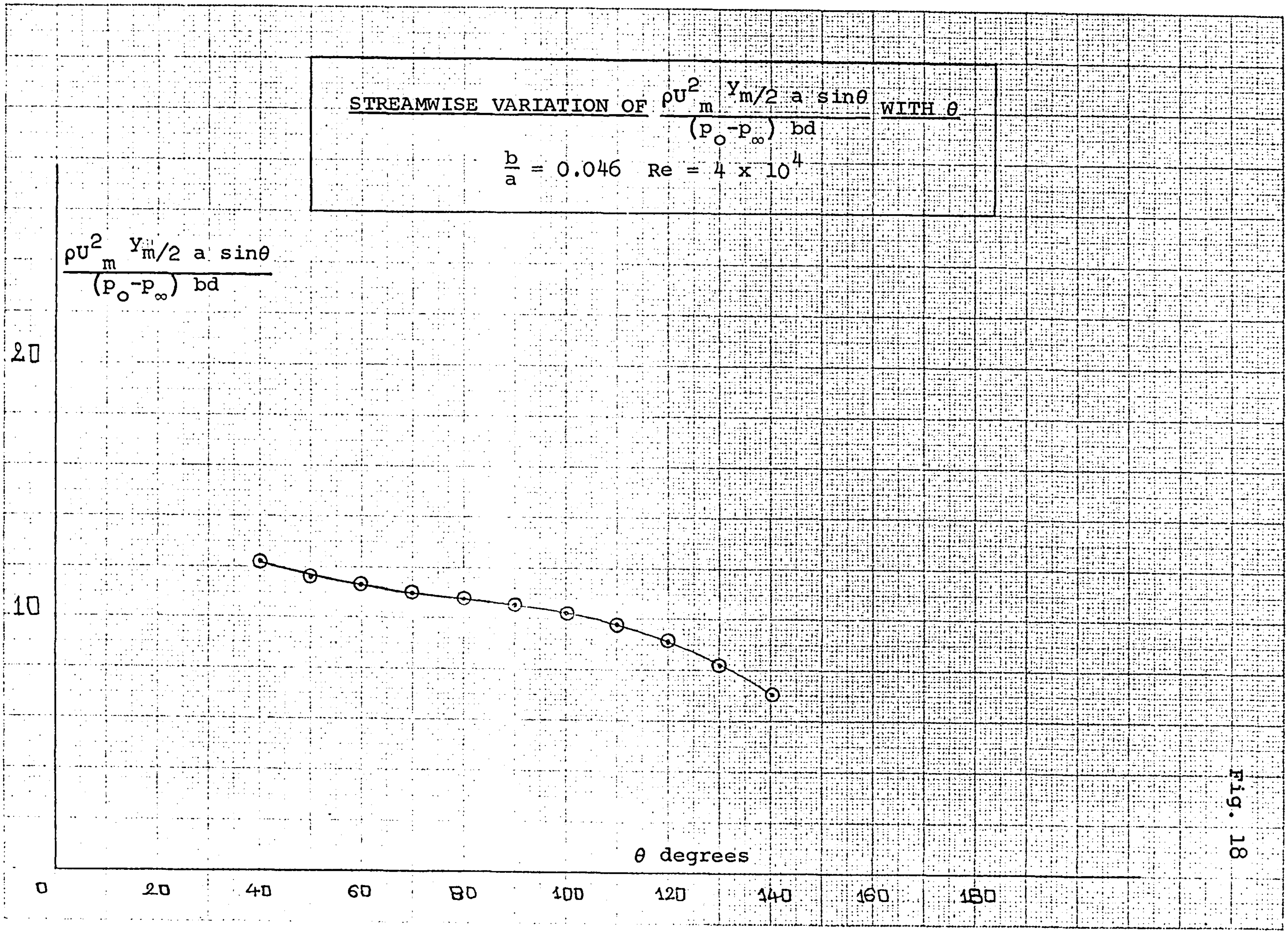
STREAMWISE VARIATION OF $\frac{\rho U_m^2 \, y_{m/2} \, a \sin\theta}{(p_o - p_\infty)\, bd}$ WITH θ
$\frac{b}{a} = 0.046 \quad Re = 4 \times 10^4$
$\frac{\rho U_m^2 \, y_{m/2} \, a \sin\theta}{(p_o - p_\infty)\, bd}$
20
10
θ degrees
0
20
40
60
80
100
120
140
160
180

Fig. 18

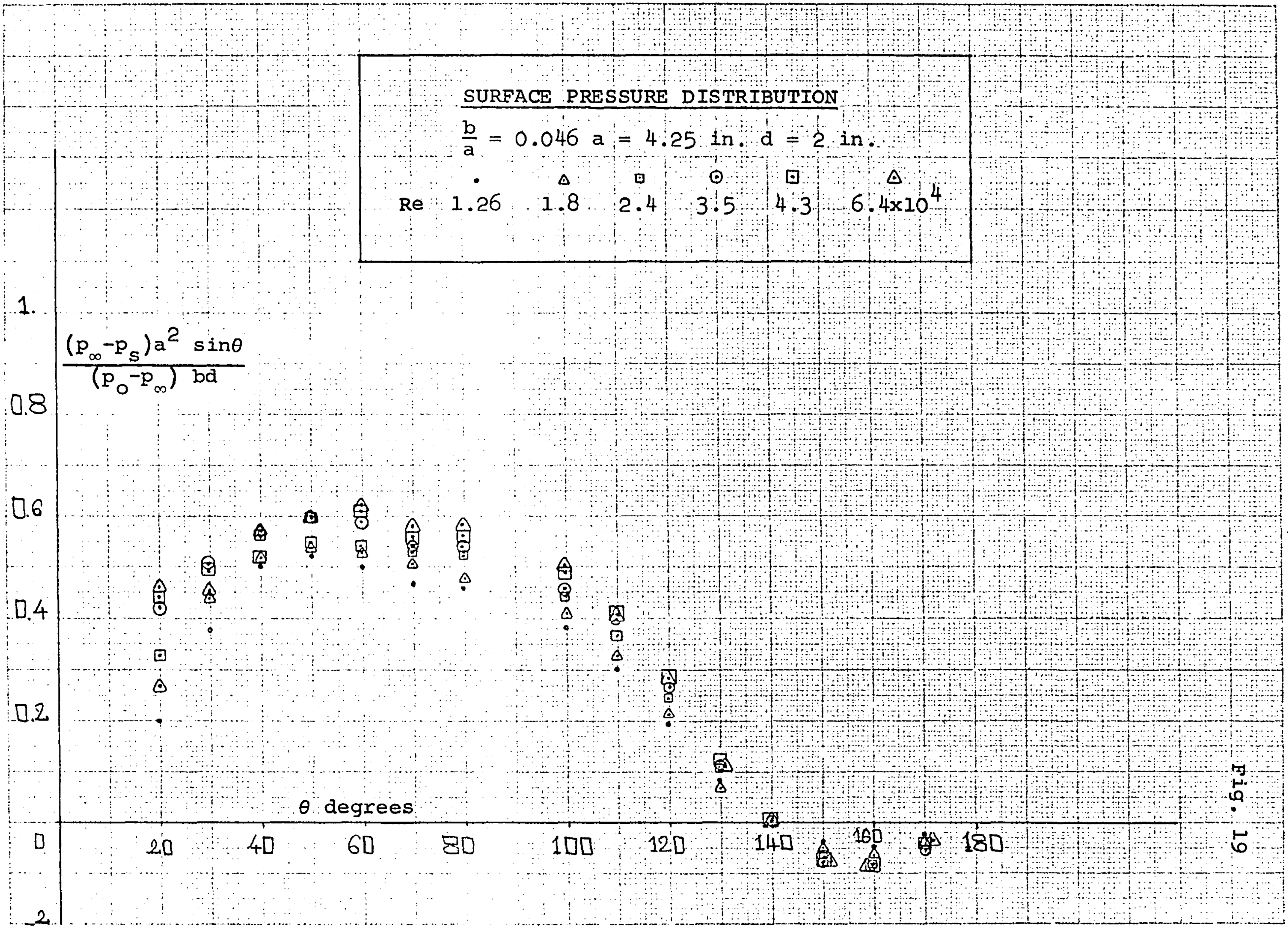

SURFACE PRESSURE DISTRIBUTION
$\frac{b}{a} = 0.046$ a = 4.25 in. d = 2 in.
Re 1.26 1.8 2.4 3.5 4.3 6.4×10^4
$\frac{(p_\infty - p_s) a^2 \sin\theta}{(p_o - p_\infty) bd}$
θ degrees
1.
0.8
0.6
0.4
0.2
0
-.2
20
40
60
80
100
120
140
160
180

Fig. 19

Fig. 20

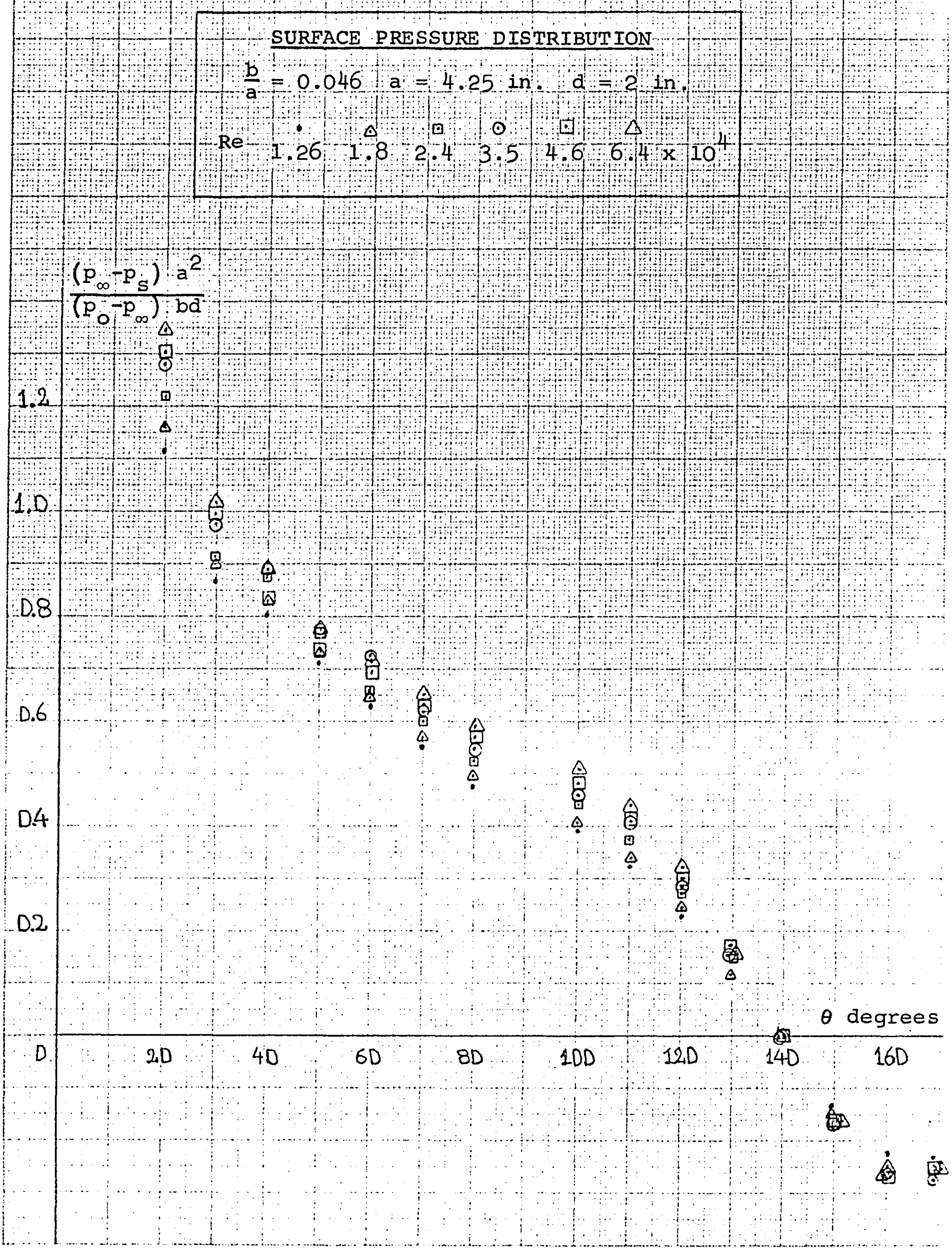
SURFACE PRESSURE DISTRIBUTION
b/a = 0.046 a = 4.25 in. d = 2 in.
Re 1.26 1.8 2.4 3.5 4.6 6.4 x 10^4
(p∞-ps) a^2 / (po-p∞) bd
1.2
1.0
0.8
0.6
0.4
0.2
0
20
40
60
80
100
120
140
160
θ degrees

Fig. 21

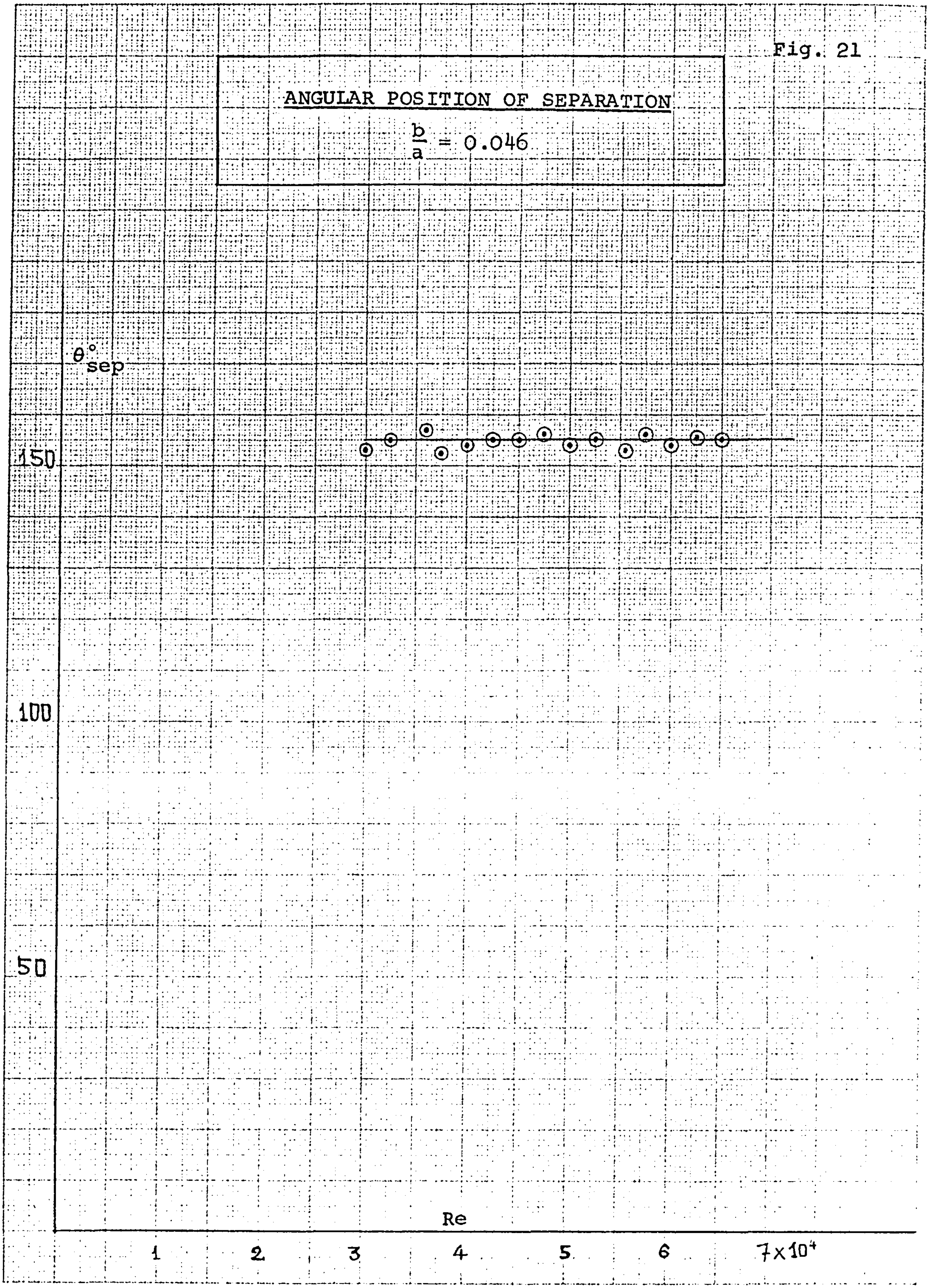

ANGULAR POSITION OF SEPARATION
$\frac{b}{a} = 0.046$
θ°_{sep}
150
100
50
Re
1
2
3
4
5
6
7×10^4

Fig. 22

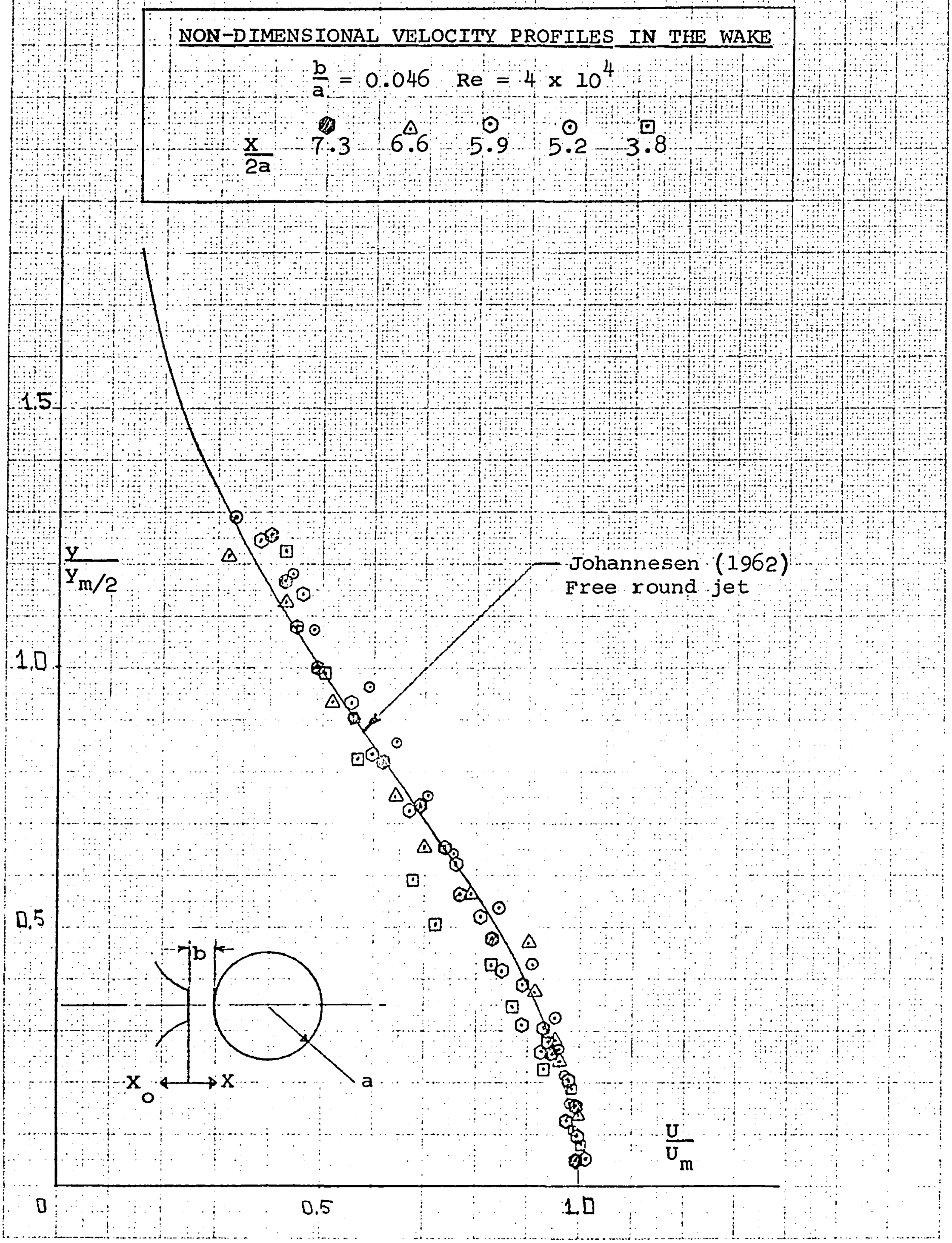

NON-DIMENSIONAL VELOCITY PROFILES IN THE WAKE
b/a = 0.046 Re = 4 x 10^4
X/2a 7.3 6.6 5.9 5.2 3.8
Johannesen (1962)
Free round jet
y/y_m/2
1.5
1.0
0.5
0
0.5
1.0
U/U_m
b
a
X_o
X

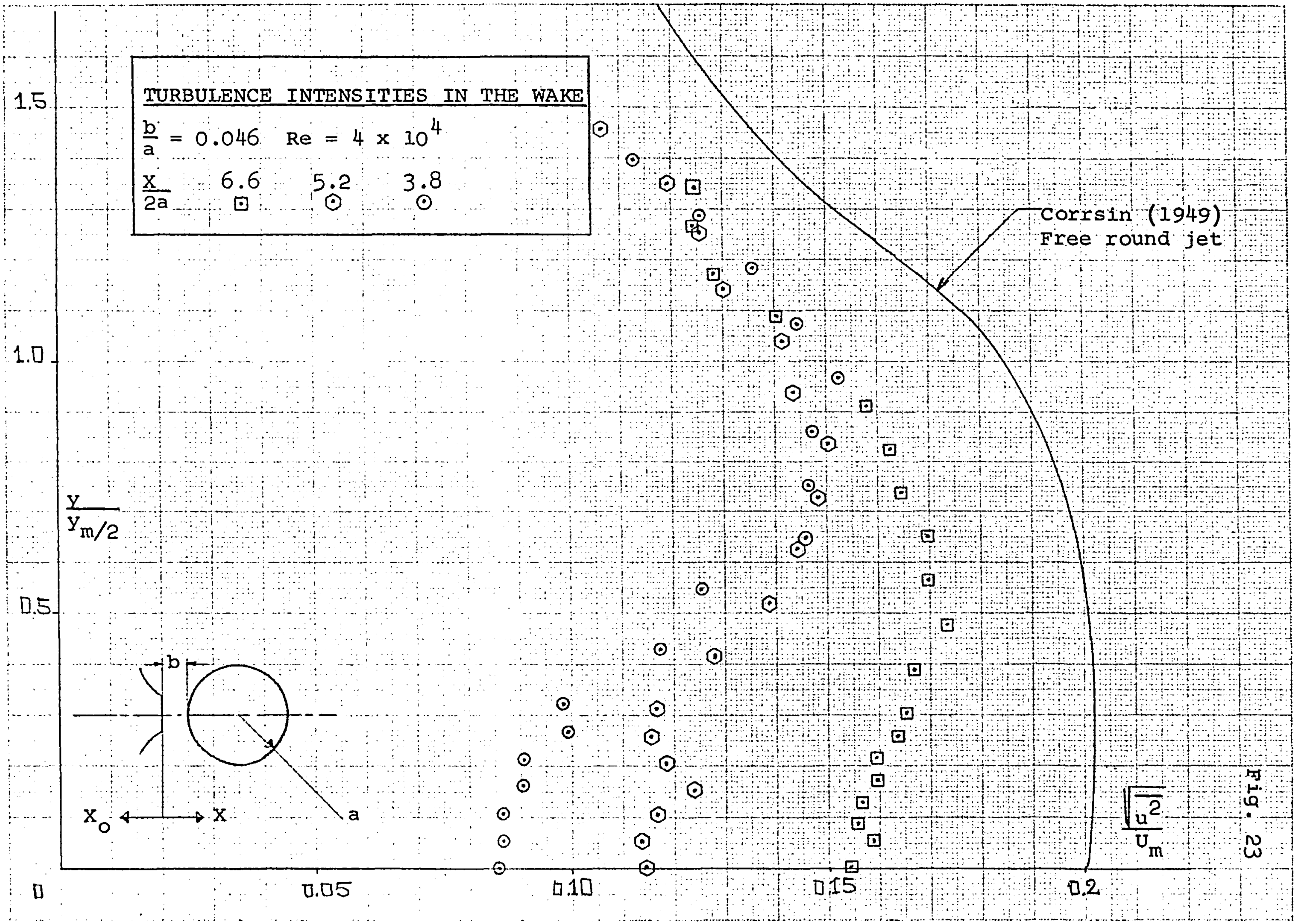

TURBULENCE INTENSITIES IN THE WAKE
b/a = 0.046 Re = 4 x 10^4
x/2a 6.6 5.2 3.8
Corrsin (1949)
Free round jet
1.5
1.0
0.5
0
0.05
0.10
0.15
0.2
y/y_m/2
√(u²)/U_m
b
a
x_o
x

Fig. 23

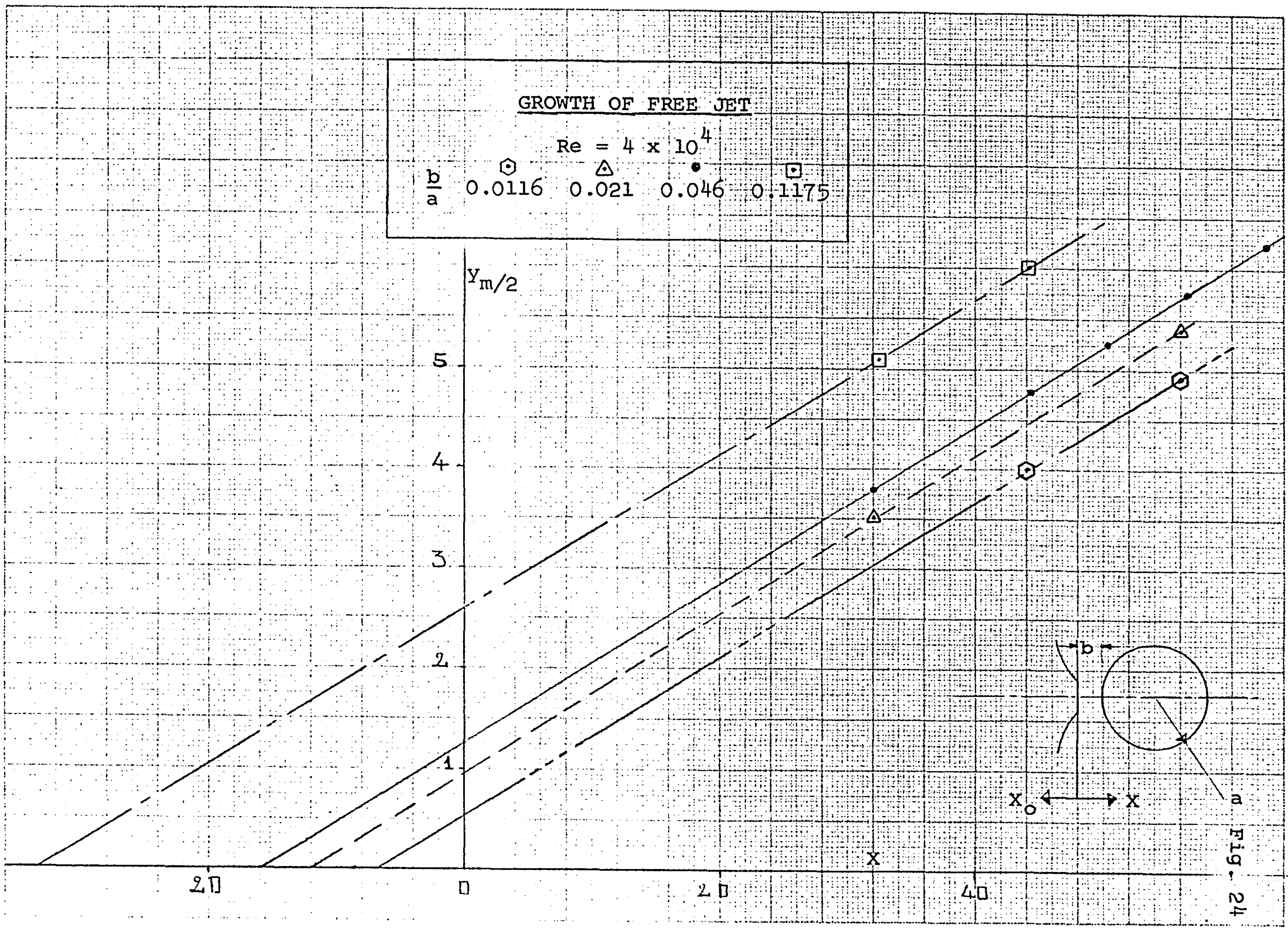
GROWTH OF FREE JET
Re = 4 x 10^4
b/a 0.0116 0.021 0.046 0.1175
y m/2
5
4
3
2
1
20
0
20
40
X
b
Xo
X
a

Fig. 24

Fig. 25

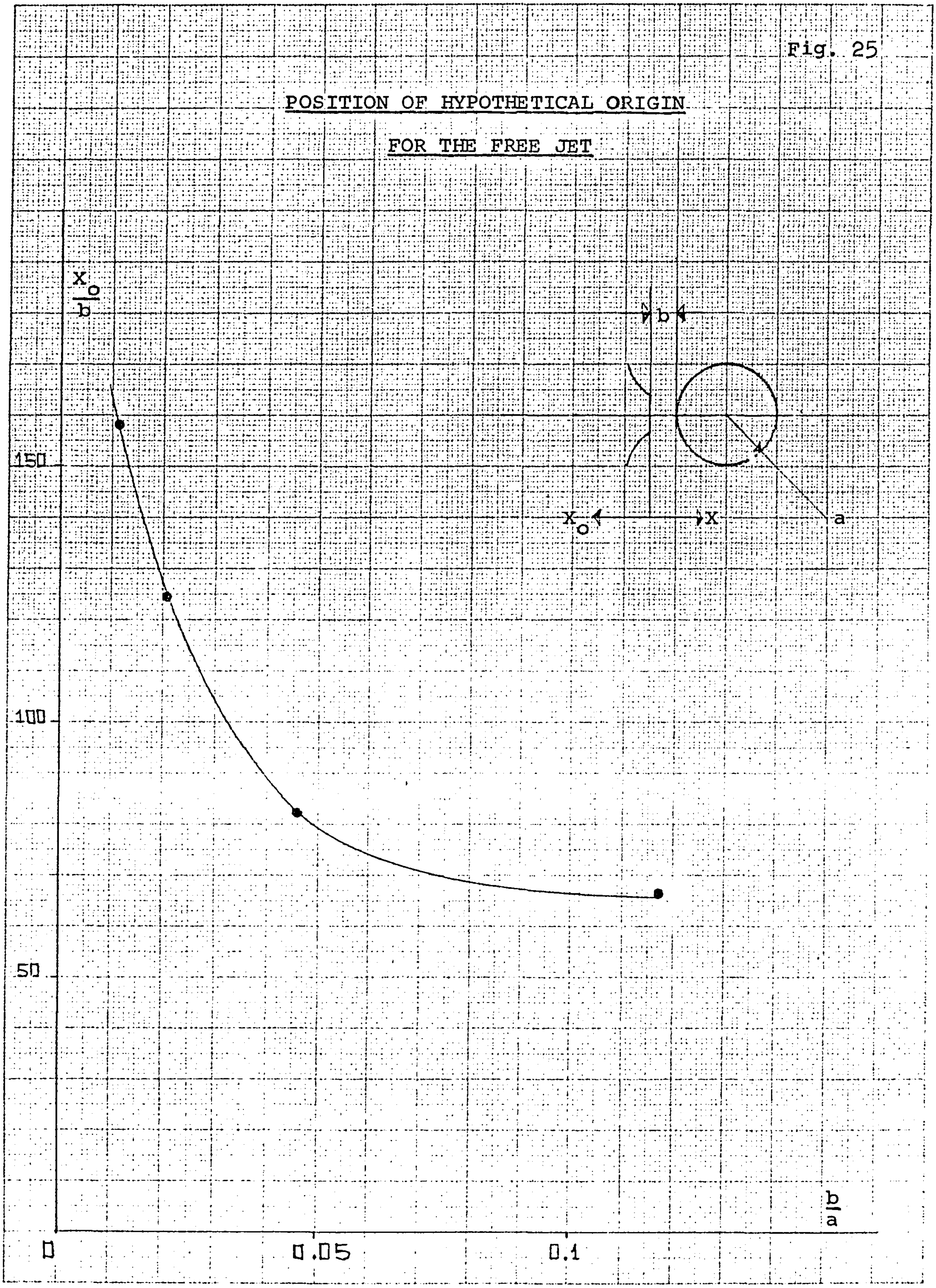
POSITION OF HYPOTHETICAL ORIGIN
FOR THE FREE JET
$\frac{X_o}{b}$
150
100
50
0
0.05
0.1
$\frac{b}{a}$
b
X_o
X
a

COMPARISON OF THEORIES FOR THE

MAXIMUM VELOCITY ON THE OUTSIDE OF A CIRCULAR CYLINDER

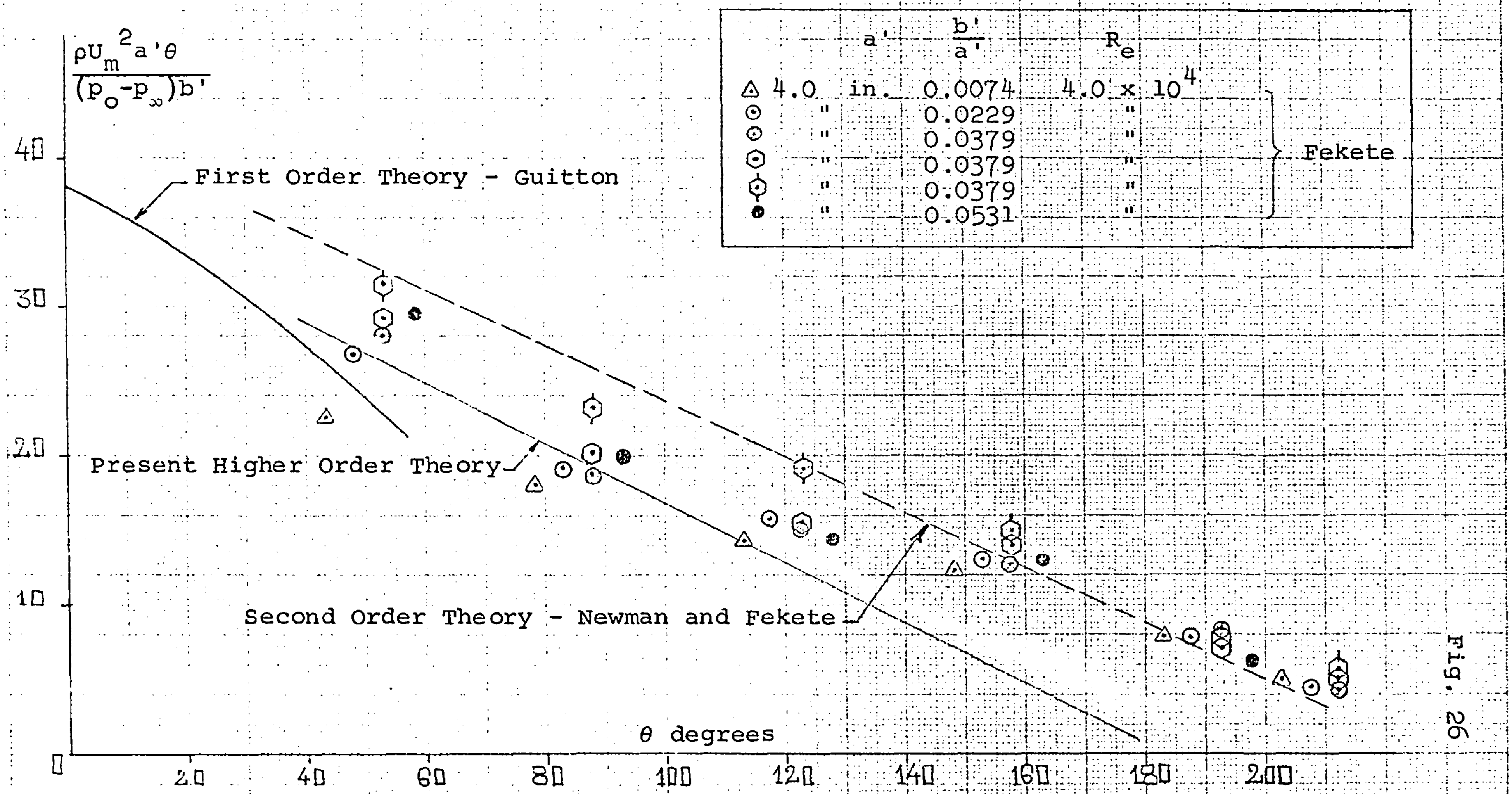

Fig. 26

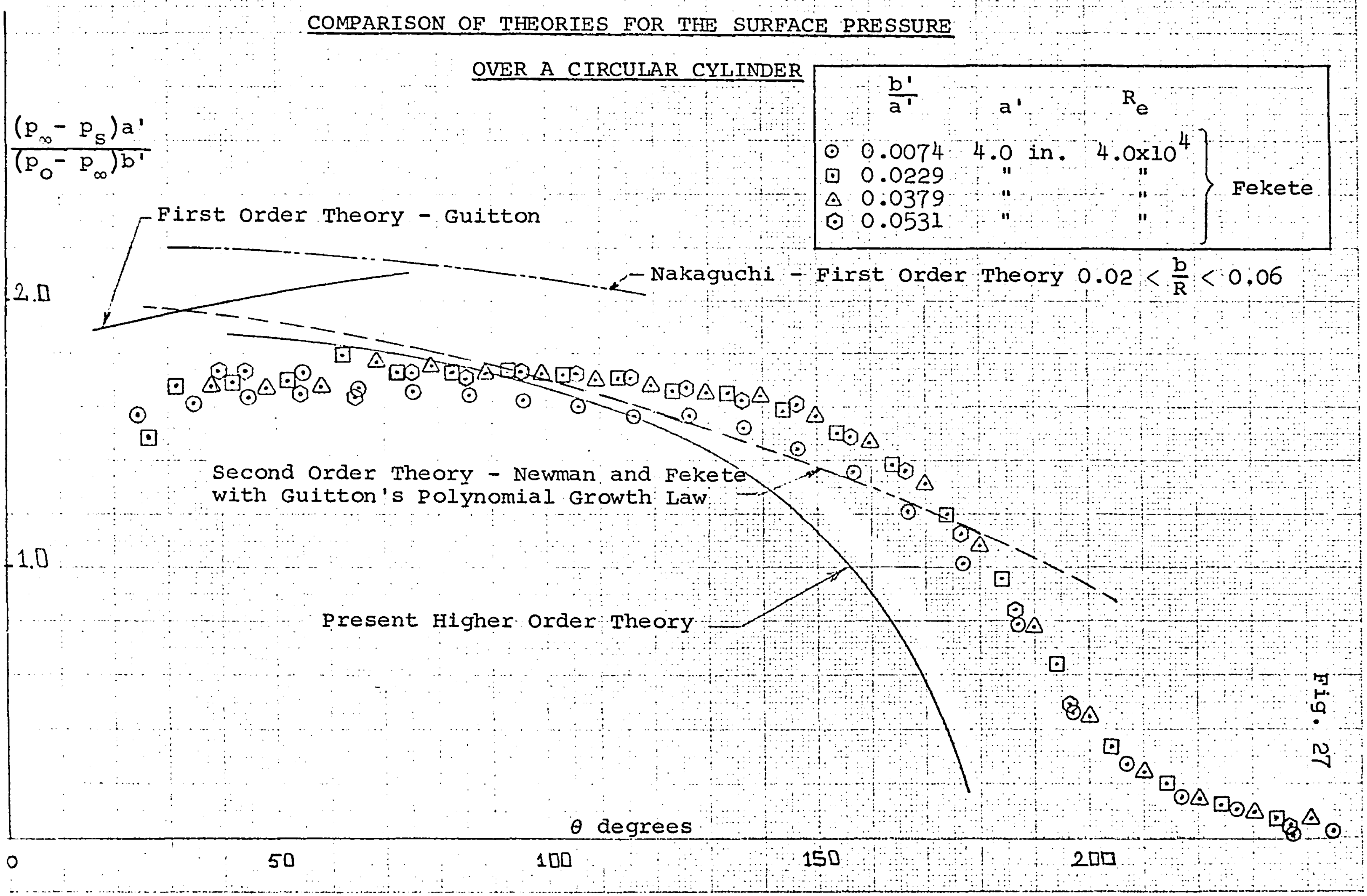
COMPARISON OF THEORIES FOR THE SURFACE PRESSURE
OVER A CIRCULAR CYLINDER
$\frac{(p_\infty - p_s)a'}{(p_o - p_\infty)b'}$
b'/a'
a'
R_e
0.0074 4.0 in. 4.0x10^4
0.0229 " "
0.0379 " "
0.0531 " "
Fekete
First Order Theory - Guitton
Nakaguchi - First Order Theory 0.02 < b/R < 0.06
Second Order Theory - Newman and Fekete with Guitton's Polynomial Growth Law
Present Higher Order Theory
2.0
1.0
θ degrees
0
50
100
150
200

Fig. 27

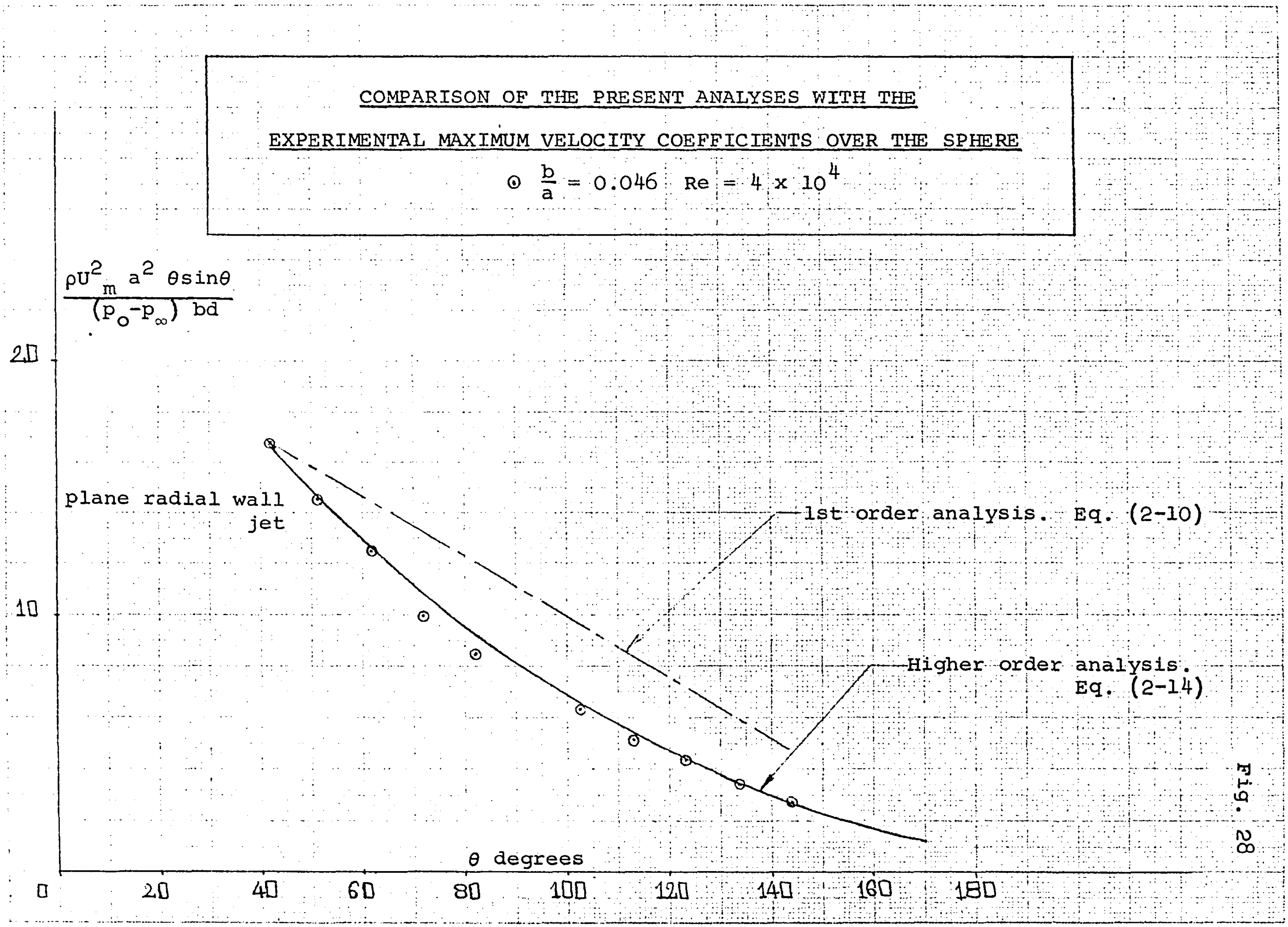
COMPARISON OF THE PRESENT ANALYSES WITH THE
EXPERIMENTAL MAXIMUM VELOCITY COEFFICIENTS OVER THE SPHERE
$\odot \; \frac{b}{a} = 0.046 \quad Re = 4 \times 10^4$
$\frac{\rho U_m^2 \, a^2 \, \theta \sin\theta}{(p_o - p_\infty) \, bd}$
2.0
1.0
0
20
40
60
80
100
120
140
160
180
θ degrees
plane radial wall jet
1st order analysis. Eq. (2-10)
Higher order analysis. Eq. (2-14)

Fig. 28

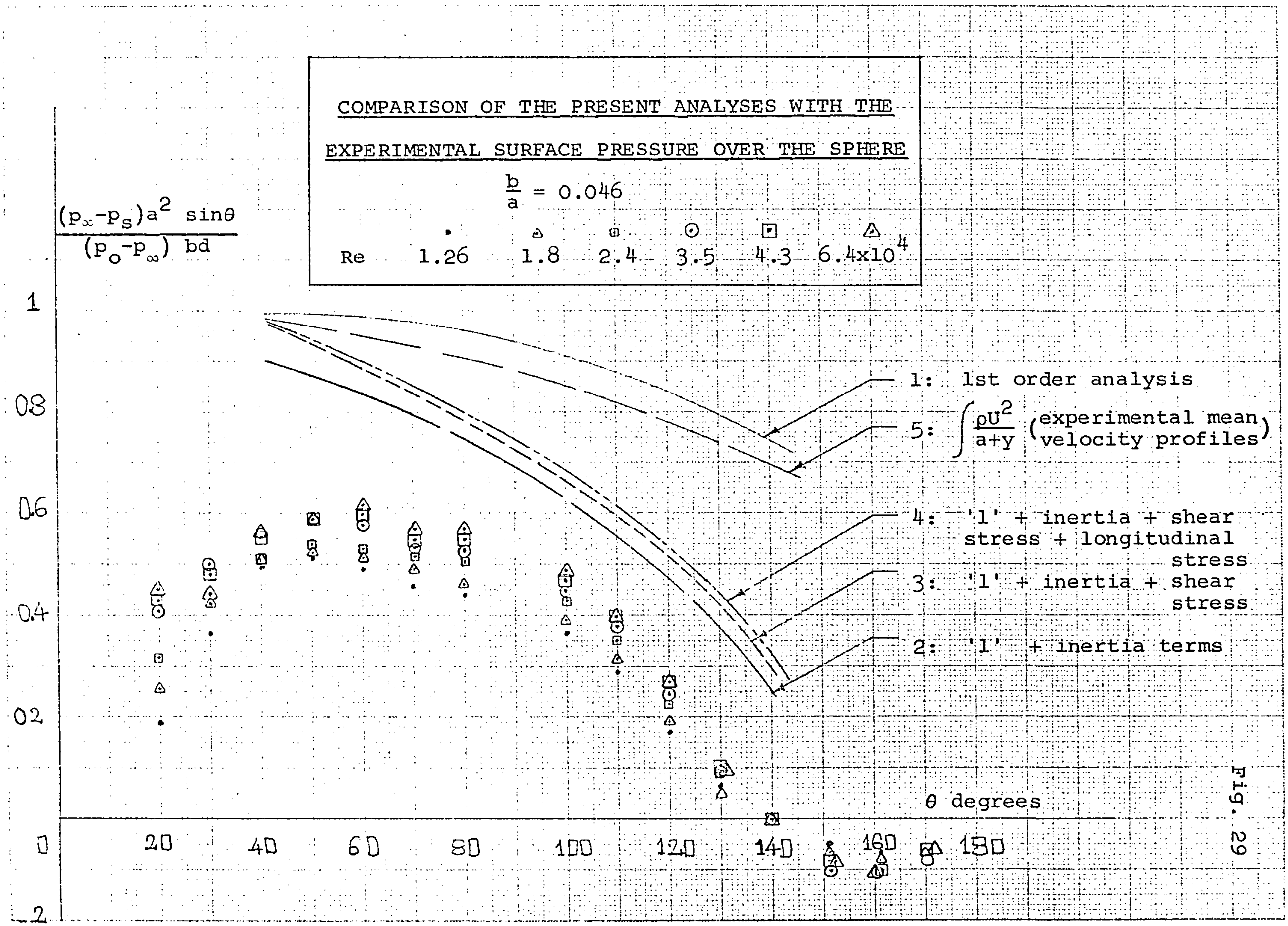

COMPARISON OF THE PRESENT ANALYSES WITH THE EXPERIMENTAL SURFACE PRESSURE OVER THE SPHERE
$\frac{b}{a} = 0.046$
Re 1.26 1.8 2.4 3.5 4.3 6.4x10^4
$\frac{(p_\infty - p_s)a^2 \sin\theta}{(p_o - p_\infty)\, bd}$
1
0.8
0.6
0.4
0.2
0
-.2
20 40 60 80 100 120 140 160 180
θ degrees
1: 1st order analysis
5: $\int \frac{\rho U^2}{a+y}$ (experimental mean velocity profiles)
4: '1' + inertia + shear stress + longitudinal stress
3: '1' + inertia + shear stress
2: '1' + inertia terms

Fig. 29